Alexandrina Machado Barbosa

Study of zirconia antibacterial surfaces for application on dental Implants

October, 2018

Universidade do Minho
Escola de Engenharia

Alexandrina Machado Barbosa

Study of zirconia antibacterial surfaces for application on dental Implants

Dissertação de Mestrado
Ciclo de Estudos Integrados Conducentes ao
Grau de Mestre em Engenharia de Materiais

Trabalho efectuado sob a orientação do
Professor Doutor Óscar Manuel Novais Carvalho
Professor Doutor Filipe Samuel Correia Pereira da Silva

October, 2018

ACKNOWLEDGMENTS

During the realization of this master thesis, there were some people that contributed for the realization of this work and I want to express my acknowledgements to them. Thus...

To Professor Óscar Carvalho, for the guidance and inspiration transmitted throughout the realization of this dissertation, always accompanied with good mood and enthusiasm.

To Professor Filipe Samuel for the opportunity to do this work, and for the valuable suggestions and words of wisdom shared.

To Sara Madeira for the patience, dedication and competence demonstrated during this work, even when it was not exactly her function.

To Professor Joaquim Jorge, from textile department, for the immediate availability shown when the need to perform mechanical tests in the neighbouring department arose.

To Caroline, Diana, Mafalda, Flávio e Helena and to all the collaborators of the CMEMS laboratory for all the support, good humor, mutual help, and encouragement demonstrated.

To professor Mihaela Buciumeanu for the support provided during the friction tests.

To the professors with whom I have crossed, during these academic years, who inspired me with their knowledge, but above all, with the modesty, devotion and enthusiasm that gave me motivation to continue this journey.

To my friends of university for the lunch hours in good company and the fellowship demonstrated over the academic years.

To my long-time friends Flávia and Pedro Faria (the cousins), Mafalda Pimenta, Sara Mota, Tânia and Daniela Rodrigues (sisters) and Andreia Lima (the godmother of *praxis*) for being present at good and bad times. For the patience, and specially for the moments of laughter which contributed to finish this step with better mood.

To my companion César Salgado for the support and words of encouragement given over the academic journey. As well as for the patience and concern shown over the years.

To my brothers and sisters, who had a very different childhood from me, for taking care of me all these years. Also, for the unprecedented support and care shown during my growth.

And above all, to my parents for the immeasurable support at all levels demonstrated during this period. For the trust deposited and words of strength in the good and bad moments.

ABSTRACT

Dental implants are currently the most reliable solution for dental replacement. Although Titanium alloy (TiAl4V) is considered the gold standard dental implant material, some disadvantages have been pointed such as metallic ions release and its greyish colour that can be visible through fine mucosa. Zirconia (ZrO_2) is a bioceramic that has been studied as a promising metal-free alternative to titanium due to its good biocompatibility, good mechanical properties compared to other ceramics, good aesthetic, due to its tooth-like colour and low affinity to bacterial microorganisms.

Despite the high rate of successful dental implants, problems related to the entry and proliferation of bacteria to the peri-implant zone have been emerging. Peri-implantitis is the most frequent biological cause that leads to implant failure and immediate implant removal. Thus, is extremely important to develop a zirconia surface with antibacterial properties to apply in dental implants. In this context, the present dissertation addresses the study of a barrier approach to inhibit the penetration of microorganisms into the peri-implant zone through the production of successive microgrooves and a biocide approach to eliminate the bacteria that interact with the implant by silver and gold surface chemical functionalization.

The microgrooves were produced by an Nd:YAG laser, morphologically characterized by SEM and tested for their retention capacity to artificial soft tissue by mechanical tensile test. Its roughness was also evaluated. The micro-functionalization with silver (Ag) was performed in a two-step process of cold pressing and laser sintering via Nd:YAG laser. And the gold (Au) nano-functionalization was tested by three different methods from which one was selected. Thus, the Au nano-functionalization was carried out by deposition by spray and sintering via CO_2 laser. The chemical functionalized samples were subjected to reciprocating friction tests against bone to simulate implant insertion and then analysed through SEM/EDS.

The results achieved showed that the introduction of microgrooves on zirconia surface increased the mechanical retention to artificial soft tissue. Roughness evaluation revealed the need for an improvement on laser finishing. The chemical functionalized surfaces presented good resistance to the friction test against bone. Additionally, the obtained COF values can predict good primary stability of the implant. The modified surfaces revealed promising results in the context of the application.

KEYWORDS: Zirconia, Dental implants, Antibacterial, Mechanical barrier, Microgrooves, Biocide effect, Gold nanoparticles (AuNP's), Silver microparticles (Ag)

RESUMO

Os implantes dentários são atualmente a solução mais confiável para a substituição dentária. Embora a liga de Titânio (TiAl4V) seja considerada o material de excelência em implantes dentários, algumas desvantagens têm sido apontadas, como a libertação de iões metálicos e a sua cor acinzentada que pode ser visível através da gengiva fina. A Zircónia (ZrO_2) é uma biocerâmica que tem vindo a ser estudada como uma promissora alternativa ao Titânio, devido à sua boa biocompatibilidade, boas propriedades mecânicas comparativamente a outras cerâmicas, boa estética devido à sua cor clara e à baixa afinidade para com as bactérias.

Apesar da elevada taxa de sucesso dos implantes dentários, têm surgido problemas relacionados com a entrada e proliferação de bactérias na zona peri-implantar. A peri-implantite é a causa biológica mais frequente da falha do implante. Sendo assim, torna-se importante desenvolver uma superfície em Zircónia com propriedades antibacterianas. Neste contexto, a presente dissertação contempla o estudo de uma abordagem de barreira para inibir a penetração de microrganismos na zona peri-implantar através da produção de micro rasgos sucessivos á superfície e uma abordagem biocida para eliminar as bactérias que interagem com o implante por funcionalização química da superfície com prata e ouro.

Os rasgos foram produzidos através de um laser Nd: YAG e foram avaliados quanto à sua retenção em gengiva artificial com testes de tração uniaxial. A sua rugosidade também foi avaliada. A micro-funcionalização foi realizada com prata (Ag) por um processo de prensagem a frio seguida de sinterização a laser Nd: YAG e a nano-funcionalização foi realizada com ouro (Au) e foi testada por três métodos dos quais um foi selecionado. Assim sendo, a nano-funcionalização com Au foi realizada por deposição por spray e sinterização via laser de CO_2. As amostras resultantes foram submetidas a ensaios de atrito e analisadas através de microscopia eletrónica de varrimento e espectroscopia dispersiva de raios-X.

Os resultados demostraram que a introdução de rasgos na superfície em Zircónia aumentou a retenção mecânica da gengiva artificiais. A avaliação da rugosidade revelou a necessidade de uma melhoria deste parâmetro. As superfícies obtidas através da funcionalização química apresentaram boa resistência ao teste de atrito. Além disso, os valores de COF obtidos preveem uma boa estabilidade primária do implante.

As superfícies modificadas revelam resultados promissores no contexto da aplicação.

PALAVRAS - CHAVE: Zircónia, Implantes dentários, Antibacteriano, Barreira mecânica, Microrasgos, Efeito biocida, Nanopartículas de ouro (Au), Micropartículas de prata (Ag)

TABLE OF CONTENTS

LIST OF FIGURES

LIST OF TABLES

LIST OF ABBREVIATIONS AND SYMBOLS

AAS - Atomic absorption spectrometry

AuNP's - Gold nanoparticles

CMEMS - Micro fabrication and systems integration laboratory

COF – Coefficient of friction

DDW - Double distilled water

DLVO - Derjaguin, Landau, Verwey, Overbeek

EDS – Energy dispersive X-ray spectroscopy

LA - Laser ablation

LAL - Liquid medium laser ablation

LPS - Lipopolysaccharide

LSPR - Localized surface plasmon resonance

Nd:YAG – Neodymium-doped yttrium aluminum garnet

NP - Nanoparticles

OM – Optical microscopy

PBS – Phosphate-buffered saline solution

PM - Powder metallurgy

PVD - Physical vapor deposition

QACs - Quaternary ammonium compounds

Ra – Arithmetic mean surface roughness

ROS - Reactive oxygen species

Rz – Average maximum peak to valley

SD – Standard deviation

SDS - Sodium dodecyl sulfate

SEM – Scanning electron microscopy

SFE – Surface free energy

SLC – Sisma Laser Controller

SLS - Selective laser sintering

STEM - Scanning transmission electron microscopy

TEM - Transmission electron microscopy

Y-PSZ - Yttrium-oxide partially stabilized zirconia

CHAPTER 1

INTRODUCTION

Chapter 1 introduces the work developed in the present study. It comprises a brief **motivation** that led to the choice of the subject, the **objectives** of the applied methodologies and, at last, an **outline** describing the structure of this written work.

MOTIVATION

Oral health care is very important in many sectors of human life, since it affects mastication, digestion, phonation, appearance, and psychological well-being. Tooth loss is one of the reasons why people seek for oral care, it can occur at any age and for a variety of reasons related either with disease or trauma. Dental implant has been proved to be the most reliable solution to replace missing teeth because it preserves the gingival mucosa and bone with no damage to the adjacent teeth [1,2].

Although the successful dental implant rate is high, the outcomes from implant failure are devastating to the patient as its extraction involves more distressing surgical procedures and cost, also, it compromises the clinician's efforts to accomplish implant functionality and esthetics [3,4].

Peri-implantitis is the major biological cause for implant failure. Hyun-Jin et al [5] conducted a study on 2796 implants, for a period of 19 years. In this study 150 implants failed of which 64 in advanced treatment phase (late failure). Overloading, fracture and peri-implantitis were reported to be the main causes of late implant failure with 53 and 17 and 13 % respectively.

To reduce dental implant failure regarding peri-implantitis, it is crucial to develop a surface that prevents adhesion and proliferation of bacteria and, at the same time, allows good mechanical engagement with soft tissue to avoid bacteria contact. Therefore, the study of the chemical, physical and mechanical properties of the zirconia (ZrO_2) surface material in order to achieve an antibacterial surface will be the focus of this work.

Zirconia is a ceramic material with, already proved, good osteointegration [6,7], excellent biocompatibility [7–9] and good mechanical strength [10,11]. In addition, it has some advantages over the conventional titanium implants like the reduced formation of plaque on material's surface [12,13], and its tooth like colour that provides good aesthetics, especially in cases of thin gingiva or soft tissue recessions [14].

Thus, the challenge in dental implantology relies on the development of new approaches combining different methods, technologies and the latest scientific findings to create, simultaneously, functional and biocompatible surfaces capable of preventing peri-implant disease.

OBJECTIVES

The main objective of this work is to develop an yttrium-oxide partially stabilized zirconia (Y-PSZ) surface for dental implant application with the ability to inhibit oral biofilm formation and prevent peri-implant disease. It is expected that the surface developed interact with bacteria in two ways: a) as a barrier, the implant works as a physical barrier to hinder bacteria from entering through the soft tissue, and b) as a biocide, so that the implant surface holds a killing effect against oral bacteria. Certain specific objectives must be attained to accomplish with the aforementioned:

1. To investigate the fundamentals on the problematic of peri-implant disease and search for current solutions on the subject;
2. To produce Y-PSZ samples by powder metallurgy (PM);
3. Physical barrier:
   3.1. To develop a textured Y-PSZ surface with successive microgrooves by laser ablation:
   - i. To study the influence of the laser parameters on the microgroove profile, groove depth, groove width and groove interspacing;
   - ii. To characterize the morphology of the produced microgrooves by Scanning Electron Microscopy (SEM);
   - iii. To test the mechanical interlock of the grooves against artificial gum;
   - iv. To characterize the roughness from the laser finishing.
4. Biocide effect:
   4.1. To chemically functionalize the Y-PSZ surface with silver (Ag) microparticles:
   - i. To produce a micro texture on the sample surface to favour silver adhesion;
   - ii. To optimize the laser/processing parameters for the silver sintering step;
   - iii. To examine, morphologically and chemically, the Ag-Y-PSZ functionalized surface by SEM/EDS;
   - iv. To test silver adhesion by means of a mechanical friction test;
   4.2. To chemically functionalize the Y-PSZ surface with gold nanoparticles (AuNP's):
   - i. To produce a solution of gold nanoparticles by laser ablation;
   - ii. To test methodological options for the deposition of the gold nanoparticles, as well as for sintering;

iii. To optimize the laser parameters for the nanoparticles sintering step;

iv. To examine, morphologically and chemically, the AuNP's Y-PSZ functionalized surface by SEM/EDS;

v. To test the nanoparticles adhesion by means of a mechanical friction test;

OUTLINE

Chapter 1 comprises the motivation that inspired for the selection of the current subject as well as the objectives for this work and lastly the organization of the written work.

Chapter 2 presents a background research on the subject of the thesis. It comprehends an understanding on the selection of zirconia as a dental implant material (2.1) and on the problematic of the peri-implant disease (2.2). A study on the mechanisms behind bacterial adhesion and a research for the three possible material design approaches to prevent bacterial adhesion (2.3) and respective review (2.4). It also presents pertinent information on nanoparticles (2.5), followed by a review (2.6), and ends with a relevant study on laser technologies (2.7).

Chapter 3 describes, in detail, all the materials and methodologies adopted on the practical section of this work. The procedure adopted to produce the samples (3.2), as well as the applied treatments on Y-PSZ surface (3.3) and, finally, the material characterization techniques that were required (3.4).

Chapter 4 comprises all the results obtained throughout the present dissertation and it is accompanied by a detailed analysis and discussion. This chapter is divided in a total of four subchapters. These comprise the characterization results of the microgrooves produced by laser ablation (4.1), of the silver micro-functionalized surface by laser sintering (4.2) and of the NP's solution that was produced by laser ablation (4.3) in context of the gold surface nano-funtionalization (4.4).

Chapter 5 draws the main conclusions from this work and adds some suggestions for future works.

CHAPTER 2

STATE OF THE ART

The study of the requirements to achieve an anti-bacterial surface demands a background research on the subject. Therefore, understanding the mechanisms behind bacterial adhesion, researching the actual solutions on antibacterial materials for dentistry, studying the optimal chemical and physical parameters, as well as, current material manufacturing techniques are going to be the main topics of the current chapter.

2.1 Zirconia as a dental implant material

With Branemark discovery of osteointegration process, several investigations and clinical studies, as well as required surface modifications have been made to ensure titanium was a good biomaterial for oral rehabilitation [15–18]. However, allergic reactions [19,20], cellular sensitization [21,22] and galvanic current formation [22,23] have been observed as side effects on the use of this material [5–9], leading the way to zirconia which arises as a good alternative material to overcome these problems. Zirconia (ZrO_2) is an advanced ceramic material that shows biocompatibility [7–9], chemical inertness [24,25], and reduced formation of dental plaque [12,13], that are major factors on promoting good osteointegration of an implant. Zirconia also possesses good mechanical properties, such as high flexural strength [10,11], good corrosion and wear resistance [26,27], and superior fracture toughness when compared to other ceramics [15,16]. In addition, in opposite to titanium, zirconia provides good aesthetics that derives from its teeth-like colour, useful, for instance, on thin gingiva recession [14,30,31].

Since 1970s considerable research has been made about zirconia, due to its transformation toughening ability, holding a unique place amongst oxide ceramics with respect to mechanical properties. Transformation toughening mechanism is associated to a martensitic-like transformation of tetragonal metastable grains into a monoclinic state that happens at the crack tip. However, only after the 1990s zirconia implants become available in the market [32,33].

Zirconia can present itself in three atomic structural forms: monoclinic, tetragonal and cubic. In pure state, zirconia has a monoclinic structure, at room temperature, which remains stable up to 1170 °C (Figure 1a). From the later temperature up to 2370 °C the tetragonal structure is formed (Figure 1b). The cubic structure develops from 2370 °C up to the melting point of the material, which is 2680 °C (Figure 1c). When cooled, the crystalline transformations are spontaneously reverted to the most stable phase, however the tetragonal and cubic structures can be metastatically retained at room temperature with the addition of other cubic oxides named stabilizers. In this work the selected material is Zirconia Partially Stabilized with 3 mol% of yttrium oxide (Y-PSZ) [32].
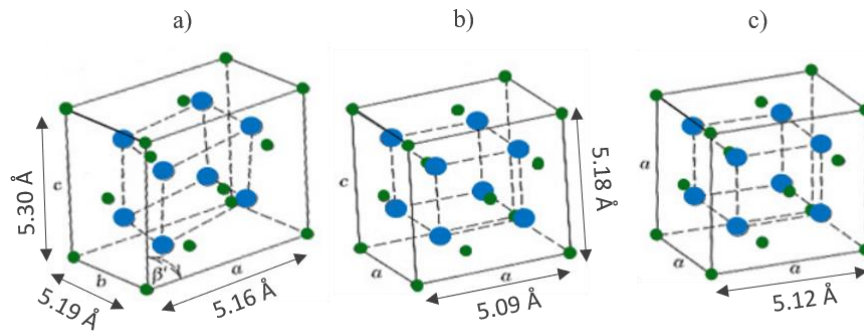
Figure 1 Schematic representation of the atomic crystalline structures of zirconia (ZrO₂): a) monoclinic, b) tetragonal, c) cubic. In blue are represented the oxygen atoms and green the zirconium atoms. Adapted from [34]*.*

Table 1 shows density, flexural strength, young modulus and fracture toughness values of Y-PSZ (3 mol% of yttrium oxide).

Table 1. Property values of zirconia (Y-TZP) from literature.

Property	Value (unity)	Ref
Density	≈ 6 g/cm^3	[35–37]
Flexural strength	900-1200 (MPa)	[35,37]
Young's modulus	≈ 200 (GPa)	[35,37]
Fracture Toughness (K_{IC})	6-10 (MN/m$^{3/2}$)	[35,37]

2.2 The problematic of peri-implant disease

Even though the successful dental implant rate is high [5,38,39], the outcomes from implant failure are devastating to the patient. Its extraction involves distressing surgical procedures and additional costs [4,40]. Implant failure can be related to biological or nonbiological complications. In one hand, nonbiological complications may be caused by lack of stability, overloading, or mechanical fracture, which for instance, may be dependent on implant factors as shape [6,41], material properties [6,42], and quantity of bone surrounding the implant [6].On the other hand, when it comes to biological complications, the situations recorded are inflammation, host response, and peri-implantitis, which, in this case, are tightly related with the interaction of the implant surface with the surrounding medium, thus, surface mechanical, topographic, and physicochemical properties are of great influence in biological processes [44][30].

With respect to implant failing occurrence, it can happen in an early or in a late stage of treatment. Early failure is associated with poor bone quality/quantity [4,40], lack of primary stability [4,40], premature loading [4,5], and late failure is related with overloading [5,45], mechanical fracture [5,45], and peri-implantitis [5,40,45,46].

Periimplantitis is an oral disease derived from a bacterial infection located at peri-implant site, it presents as implant pocket formation which is the loss of the supporting bone around implant [47–49]. When bacteria from oral microbiota migrates to peri-implant site they tend to attach to a subtract/surface and colonize producing a biofilm. This biofilm development is responsible for the activation of the host immune and inflammatory responses around the implant, which is crucial in the pathogenesis of periimplantitis and consequent loss of supporting bone [50–52]. The most common bacteria associated with peri-implant disease are: *Porphyromonas gingivales*, *Porphyromonas intermedia*, *Actinobacillus actinomycetemcomitans* [53,54], *Streptococcus aureus* [55,56], *Streptococcus mutans* [57,58], *Streptococcus sanguinis* [59,60].

Hyun-Jin et al. [5] conducted a study on 2796 implants focused on implant failure, for a period of 19 years. In this study, from the total tested implants 150 implants failed in which 64 at an advanced treatment phase (late failure). Furthermore, they reported that the main causes of late failing implant is related to overloading and fracture of the implant, with 53% and 17% rate, respectively, followed by peri-implantitis (13%). Another study [61] based on the prevalence rate of periodontitis determined that 10 out of 89 patients (11.2%) suffer from this peri-implant disease.

2.3 Physicochemical mechanisms of bacterial adhesion

Bacteria are divided in two main categories, gram-positive and gram-negative[1]. The gram-positive bacteria are surrounded by a plasma membrane and a cell wall containing peptidoglycan linked to lipoteichoic acids. In turn, the gram-negative bacteria present a plasma membrane and a thinner cell wall (peptidoglycan in a similar way to gram-positive)

---

[1] The terminology given to each type of bacteria is related with the colour effect visualized on a Gram stain test which is related with the differences on cell wall composition [62].

followed by an external layer of phospholipid and lipopolysaccharide (LPS) complex and impenetrable, making them resistant to the most used antibiotics [62].

The biological phenomenon of bacterial adhesion to a dental implant can be described by four phases: transport, adhesion, attachment and colonization [44].

In phase 1 occurs the transport of bacteria to the material surface. This can happen through Brownian motion[2], by sedimentation of bacteria in solution, via liquid flow or by bacteria movement itself [44].

Initial adhesion starts in phase 2, resulting in weak and reversible adhesion of the bacterium through long and short-range forces of about 50 nm from surface. Bacterium are attracted or repelled to the surface according to the resultant of the non-specific interaction forces. This phase has a duration of 2 or 3 hours [44,63]. In this stage, two physicochemical approaches are considered to describe bacterial adhesive interactions, the *thermodynamic approach* and the *classical DLVO* approach [44]. The first one is related with the surface free energy (SFE) of two interacting surfaces, and states that, before a bacterium can contact directly with the implant surface, the water film between the interacting surfaces must be removed [44]. As so, the necessary energy for this process to occur, named as interfacial Gibbs Free Energy (ΔG_{adh}), can be calculated from the following equation: $\Delta G_{adh} = \gamma_{sb} - \gamma_{sl} - \gamma_{bl}$, where γ_{sb} is the free energy between the surface and the bacterium, γ_{sl} is surface-liquid interfacial free energy, and γ_{bl} is bacterium-liquid interfacial free energy. Once nature tends to minimise free energy, if ΔG_{adh} is negative adhesion is thermodynamically favoured and will spontaneously occur [44].

The *classical Derjaguin, Landau, Verwey, Overbeek* (*DLVO)* approach identifies the existence of two forces: G_A-The Lifshitz-van der Waals attractive force that is the first force becoming active at distances greater than 50 nm: and G_E-The electrostatic repulsive force which is available at closer distances. The G_E occur because of a positive charged outer layer formed on the water particles that neutralizes the bacterium's and material's surface negative charge (the electrical double layer or Stern layer). When the bacterium/water layer overlays the surface/water layer a repulsive electrostatic interaction take place since bacterium and

---

[2] Brownian motion: Random movement of microscopic entities in fluid caused by thermal continuous agitation, it is of fundamental significance in the world of microorganism motion [181].

surface have the same charge. The distance under which this interaction arise is dependent on the thickness of each layer that in turn depends of ionic charge of the surface and ionic concentration of the medium [44]. DLVO states that at a distance above 1 nm, the sum of G_A and G_F describe the total long-term interaction between the bacteria and the surface ($G_{TOT} = G_A + G_F$). The graphic representing this relation is present on Figure 2.
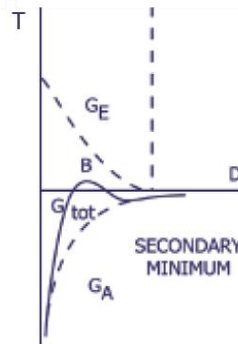
Figure 2 Graphic representation of the Lifshitz-van der Waals attractive force (G_A), the electrostatic repulsive force (G_E) and the resulting total force along the distance between bacteria and the surface [44]*.*

For bacteria in the mouth, the G_{TOT} secondary minimum (Figure 2), representing reversible chemical interactions, does not frequently reach very negative values, resulting on a 'weak' reversible adhesion. Thus, bacterium continues to exhibit Brownian motion and can readily be removed from the surface by mild shear or by the bacterium's own mobility. [44].

Although the *thermodynamic approach* and the *classical DLVO* approach have demonstrated to be adequate microbial adhesion theories for certain groups of strains, these fail on describing all aspects of microbial adhesion that is valid for every strain, as a variety of environmental and cell-specific physiological conditions way of action is still unknown [44,64].

Then, Van Oss et al. presented the *extended DLVO theory*, that comprises four fundamental, interactions: Lifshitz–van der Waals, electrostatic, Lewis acid–base and Brownian motion forces. Lewis acid–base relies on electron-donating and electron- accepting interactions between polar moieties in aqueous solutions. The influence of the acid–base interactions is much superior than electrostatic and Lifshitz–van der Waals interactions. On the other side, they are short ranged, and a close approach between the interacting surfaces (less than 5 nm) is required before these forces can become operative. This new theory has improved prediction of bacterial adhesion in several in vitro experiments [65].

After adhesion of the bacterium to the surface of the implant, comes phase 3, the attachment. In this phase, a strong anchorage between bacteria and surface occurs through covalent, ionic, or hydrogen bonding. Additionally, in this stage microorganisms secrete a

dense substance, the glycocalyx, and cover themselves in it leading to protection against humoral and cellular body immune components. The attachment takes several hours to be completed [44,63].

Finally, in phase 4 (colonization), the strongly attached bacterium starts to grow along with new cells formation, resulting in the biofilm development. The growth rate of the microorganisms depends on the material of the implant [44]. Figure 3 presents the above-mentioned four phases of bacterial adhesion as well as the approximated time of each phase.
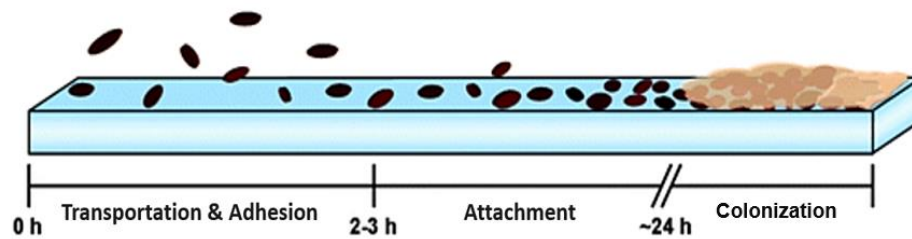
Figure 3 Schematic representation of the bacterial adhesion phases on material surface, and respective time. Adapted from [63]

Afterwards, biofilm maturation leads to the activation of host immune and inflammatory responses around the implant, which is crucial in the pathogenesis of peri-implantitis and consequent loss of supporting bone [50,66]. An explaining illustration of the plaque (biofilm) on the implant surface, inflammation (peri-implant mucositis) fallowed by peri-implantitis is observable on Figure 4. While Figure 5 represents a clinical and a radiographic image of a clinical situation of peri-implantitis, where bone loss is visible in the shape of a crater.
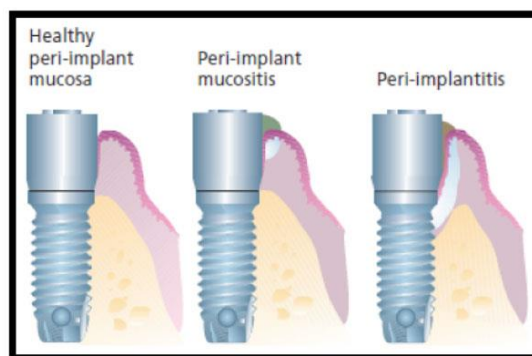
Figure 4 Illustration of pathological conditions around dental implants (peri-implant infections) [66]*.*
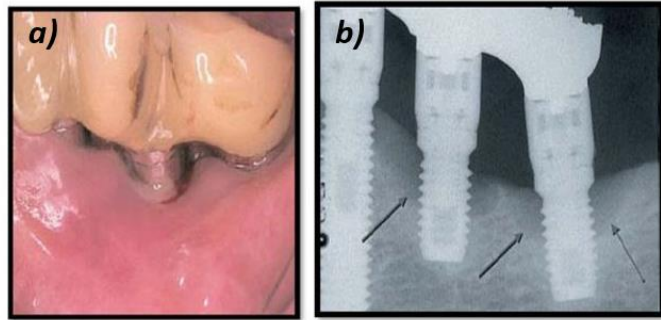
Figure 5 Clinical (a) and radiographic (b) observations of two implant sites with peri-implantitis [66]*.*

2.3.1   Material design approaches for antibacterial effect

Depending on the desired material feature to obtain, several physicochemical parameters must be studied. An implant surface can accomplish three main functions:

- Barrier;
- Antifouling;
- Promotion of bacteria elimination.

The following chapter will describe some theoretical foundations behind these three functions. A last topic summarizes the bibliographic review on the methodologic developments related with surface modification for antibacterial purposes.

2.3.2   Bacterial barrier

One of the three approaches in the problematic of bacterial infection is creating a bacterial barrier which main function is to inhibit bacteria entering through the mucosal implant zone. The oral epithelium is the primary barrier between the external environment and deeper tissues. The idea is to create a mechanical design that restricts movement between the implant surface and oral soft tissue in contact. This interface, named *biological width*, occupies 3 to 4 mm downwards length [67–69] and is schematized in Figure 6.
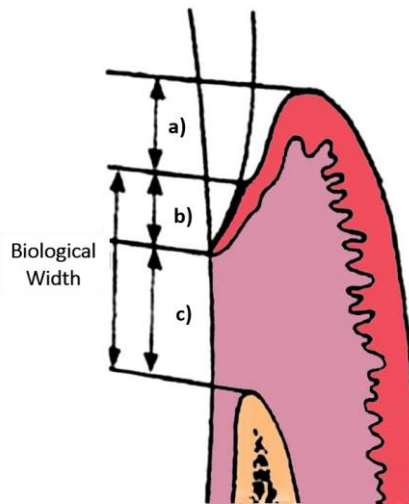
Figure 6 Illustration of the anatomy of the interface between the tooth and the soft tissue: a) histological sulcus, b) epithelial attachment, c) connective tissue attachment, and b) + c) biological width.

For the mechanical barrier to succeed is of major importance that the oral fibroblasts and epithelial cells adhere to the implant surface. Literature studies were made and a *contact-guidance* behaviour of cells on microgrooved surfaces was observed, revealing that cell positions are random on a flat surface. However, on a grooved surface cells align themselves along to the groove direction. This occurrence may be explained by the mechanical stresses created by the microgrooves which influences cell spreading and leads to cell alignment [67,70].

Aligned or elongated cells had demonstrated better adhesion compared to spherically shaped ones. In this way, surface microtextures such as grooves may influence the cell spread and growth. Investigations about the reaction of soft tissue to implant surface of oral implants reveal that surface treatment of the implant materials significantly influences the attachment of oral fibroblasts and epithelial cells [71–73].

The development of the interface between the epithelial cell and a substrate comprises two time-dependent stages, it initiates with 1) nascent adhesions, which later matures into 2) focal adhesions[3]. Cell dimension at nascent adhesion state is inferior to 0.2 µm, reaching 1–5 µm size after they mature into focal adhesions [74]. Considering this, it is more difficult for the cells to create stable focal adhesions within grooves with a groove width smaller than 5 µm.

---

[3] Focal adhesions: Macromolecular subcellular structures that mediate the regulatory effects (ie, signaling events) of a cell in response to the extracellular matrix [182].

Research on the influence of groove profile characteristics, as groove depth, width and interspacing, in cell attachment and spreading is under development in the scientific community. Studies suggest that groove width equal or superior to 10 μm is preferential on soft tissue attachment [75–77]. On the other hand, groove depth less or equal to 5 μm, in groove depth studies between 1 and 10 μm [75,78], although, research about oral soft tissue cell response to groove dimensions in orders of magnitude greater is necessary, since deeper grooves would increase the contact area between the implant and the soft tissue improving the mechanical retention of the interface.

2.3.3 Bacterial antifouling

The focus on biofilm prevention should be on inhibiting the progress from stage 1) bacterial adhesion to stage 2) bacterial attachment, and the associated development of irreversible chemical bonds between bacteria and the implant surface. Considering this, studies attention must be on an earlier interaction, stage 1) initial bacterial adhesion. A surface capable of prevent bacterial early stage adhesion is named an *antifouling* surface [79]. The study about the best surface characteristics for this purpose must include a chemical and a physical research line, as follows.

Chemical component

As realized in the previous chapter, *Physicochemical mechanisms of bacterial adhesion (2.3)*, the electrochemical interaction between bacteria and the material surface is very important in initial adhesion stage. As so, it becomes important to study the electronegativity of bacterial external layer in order to conclude about the appropriate charge to avoid initial adhesion. Literature studies [80–84] state that most of bacteria is negatively charged, fact that is crucial on initial adhesion. In gram-positive bacteria, this is due to the negatively charged teichoic acids on bacterium external wall and in case of gram-negative bacteria due to the presence of negatively charged carboxylic acid on O-antigen entities.

Physical component

As mentioned in the beginning of the current chapter, irreversible chemical bonds between bacteria and implant surface are undesired, therefore, transition from reversible to irreversible connections must be interrupted. A factor that prevents this evolution is the shear force applied on the material surface (which occurs, for example, during cleaning, mechanical

action, or by fluid flow), although, a rough surface offers a shelter for bacteria, protecting it from environmental forces. For that reason, the material surface roughness must be small, preferentially smaller than an ultramicrobacteria dimension, less than 0,2 μm [85–87].

2.3.4 Bacteria elimination

Chemical component

This chemical study relies basically on choosing a chemical composition with already reported bactericidal properties to apply directly on the implant surface, for instance, Quaternary ammonium compounds (QACs) [88,89], metallic nanoparticles (NP) as silver (Ag) [90] or oxide nanomaterials as, for example, zinc oxide (ZnO) [91].

Physical component

The bacteria elimination approach relies, not only on selecting a bactericidal chemical composition, but also on the scale of action chosen to work with. The material added to the substrate may present itself at micrometric or nanometric state. Different working scales will provide distinct properties to the same chemical composition [92,93]. Bactericidal compounds as single walled carbon nanotubes [94] and several metallic NP's [95,96] are good alternatives for this application, since they combine the biocide chemical composition with the nanometric size of the material.

Frequently, studies on the behaviour of nature give rise to concepts with potential to be applied on engineer science, for instance , Elena el al. [97] studied the nature phenomenon cicada wing contact-kill effect against bacteria, which hypothesizes the potential that mimicking cicada wing nanopillar pattern on material surfaces hold.

2.4 Review on current solutions for antibacterial surfaces

Several studies have been conducted on materials regarding antibacterial purposes. These studies comprise the development of a variety of material coatings, and material surface functionalization methods. Some researchers have done efforts on the development of coatings of hydroxyapatite [98,99], silver [90,100] and copper [101]. And, apart from the study of surface chemical functionalization promoted by the addition of a functional group [102,103] or a specific material with biocide properties [90,101], other researchers [44,85,87] have studied physical functionalization focused on a desired roughness.

Surface chemical functionalization may be carried out, either by introducing long chain hydrophobic positively charged components (e.g. alkylated polyethylene amines) [102,103], or by adding a functional group on the surface, which can be attained via polymerisation [104] and plasma treatment [105]. This functionalization may also occur via deposition of nanomaterials with bactericidal properties (e.g. single walled carbon nanotubes [94], metallic NP's [95,96], and nanostructured materials containing QACs) [88,89].

At nanoscale, antibacterial positive results had been reported by different oxide nanomaterials (such as zinc oxide (ZnO) [91], titanium dioxide (TiO_2) [106], copper oxide (CuO) [107] and magnesium oxide (MgO) [108]) related with both production of reactive oxygen species (ROS) (OH^-, H_2O_2 and O_2^{2-}) and direct cell membrane damage. Also metallic NP's (silver (Ag) [109], copper (Cu) [110] and gold (Au) [111]) had demonstrated antibacterial properties through ion and ROS release. The incorporation of different types of nanoparticles on dental materials improves its chemical and physical properties[89,93], and consequently, their anti-bacterial properties which is key on the preventive dentistry field. Hanan. H. Beherei et al added a ZnO NP's containing composite into an alginate polymer matrix by impregnation [112] and Juan et al. added silver NP's on titanium surface by silanization method [113].

Physical functionalization can be achieved by controlling surface topography, for instance, the surface roughness values can be potential or detrimental to bacteria colonization. Aiming to decrease bacteria adhesion, the smooth surfaces (roughness < 0.2 μm) are appointed/required [44,85,87].

2.5 Antibacterial nanoparticles

Nanotechnology has opened up a new world of possibilities with regard to oral health, from diagnostic [114,115] to preventive dentistry [112,113]. A nanoparticle is a highly reactive entity and exhibits a high specific surface area (SSA), due to its small dimension (1 to 100 nm), [89,116] which results on a larger portion of active surface sites than on a regular bulk material offering a new scale of material properties [93]. The incorporation of various kind of nanoparticles into dental materials improves its chemical and physical properties, reflecting on characteristics as osteointegration and anti-bacterial. This specific area of application is referred to as *nanodentistry* and is defined as the "*Science and technology of diagnosing,*

treating and preventing oral and dental diseases, relieving pain, preserving and improving dental health using nanostructured materials" [89].

It is known that smaller nanoparticles have a stronger bactericidal effect since morphological and physicochemical characteristics of the NP's are size dependent. Metal nanoparticle's positive surface charge eases their binding to the negatively charged surface of the bacteria, which may result in an increase in the bactericidal effect. Also the shape of nanoparticles influences their antimicrobial properties [117].

The raw materials on nanoparticles production may be, a) polymeric: polyethylene glycol, solid lipids, nanogels, dendrimers, chitosan; b) metallic: silver, gold, copper; or c) non-organic: zirconia, silica, titanium dioxide, hydroxyapatite, quantum dots, nanocarbons [89].

2.5.1 Metal NP in bacterial cell damage

Although there is not an agreement on the chemical activity that leads to the observed anti-bacterial action of metal nanoparticles, some theories are under investigation [117,118]:

a) the DNA replication (bacteria's life cycle process) stops due to uptake of free metal ions through the bacteria cell wall, leading to its damage and/or death;

b) metal nanoparticles and metal ion generates reactive oxygen species (ROS);

c) the metal nanoparticle directly damage the cell membrane [117,118].

ROS are believed to affect three distinct cell entities: the cell DNA, the cell membrane and the cell membrane proteins. And the metal ion release will affect the bacteria DNA and the membrane proteins [118]. In Figure 7 some hypothetic interactions between nanoparticles and bacteria cell are schematized. The event identified in the image as 1) and 2) illustrates the nanoparticle ions release and generation of ROS, as well as, their interactions with membrane proteins affecting cellular correct function. Area 3) schematizes the NP accumulation in the cell membrane affecting membrane permeability, and on area 4) is represented the entrance of nanoparticles into the cell and generation of ROS, ions release, affecting DNA [118].
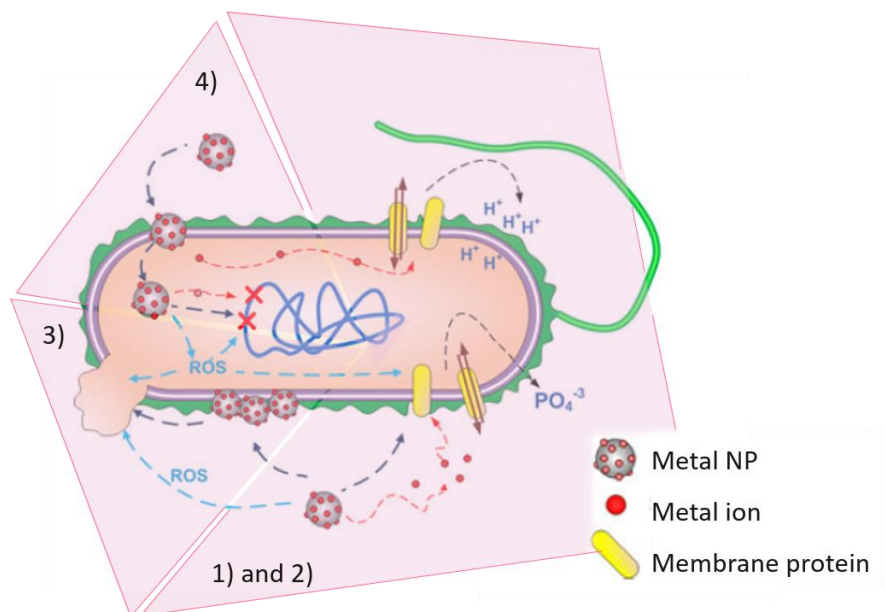
Figure 7 Illustration of hypothetic interactions between metal nanoparticles and bacteria cell. Adapted from [118]*.*

Metallic nanoparticles generate very intense electromagnetic field that results in unique catalytic characteristics, and optical properties also benefit from this new electromagnetic potential. Gold (Au) is a stable material which has gained great interest at nanometric scale due to the change in electromagnetic properties [93,119]. Nobel metal NP's, as Au, have a peculiar dependence of colour on a size, shape and dispersion which is useful, for instance, on diagnosis in medical field. Bulk gold is golden/yellow while gold nanoparticles can exhibit different shades varying from greyish blue to ruby red, and black [120,121]. This colour dependence on size and shape is explained by the quantum physics theory of *localized surface plasmon resonance* (LSPR) absorption.

In LSPR, all the light scattering happens only at the surface (the region where all the interactions occur), since mean free path in gold is 50 nm LSPR is only characteristic from nanoparticles smaller than 50 nm. When the wavelength of the incident light is larger than the nanoparticle size, it polarizes the electrons at the NP surface, causing an oscillation in resonance with the frequency of the absorbed light [119–121], standing resonance conditions as represented is Figure 8. Since this is a surface interaction, shape or size of the nanoparticle affects the surface geometry causing a shift in the electric field on the surface, shifting the oscillation frequency of the electrons, and consequently generating different cross-sections for the optical properties including absorption and scattering (diamond prism-like effect). The reported Gold NP's maximum light absorption wavelength in 15 nm particles is 525 nm increasing to 575 nm in 45 nm sized particles [93].
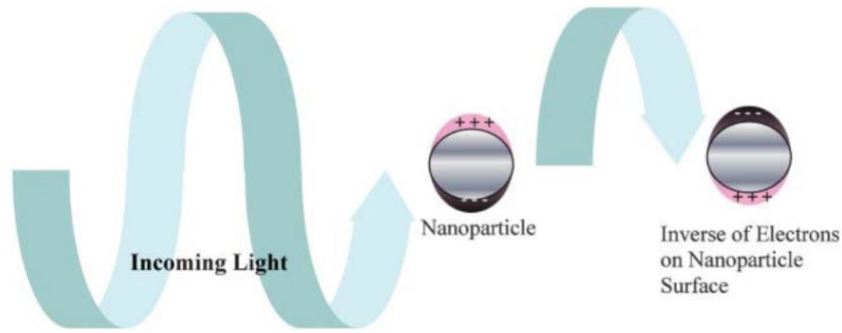
Figure 8 Origin of surface plasmon resonance due to coherent interaction of the electrons in the conduction band with light. Extracted from [119]*.*

The gold bulk melting temperature is around 1336 K (1063°C) [92]. However the melting point of nanoparticles is dependent on particle size [92,93]. Melting point decreases intensively with particle size reduction, as can be seen in Figure 9. Regarding AuNP's produced in this work with 5 nm average size, the melting point is around 1100 K (827 °C).

Not only the melting temperature decrease in nanometric particles but also sintering process begins and proceeds at a lower temperature than for conventional micrometric particles.
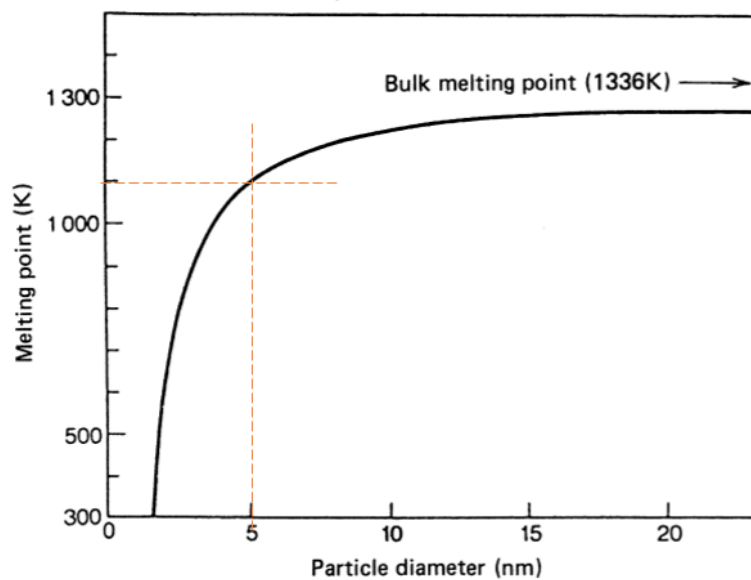
Figure 9 Calculated value for the evolution of the melting point along particle diameter for superfine particles of gold [92]. The intersecting dashed strokes indicate the melting temperature that is significant for the subject.

2.5.2   Gold Nanoparticles in bacterial cell damage

Y. Cui et al. [122] studied Gold NP's bactericidal action mode and concluded that it can happen mainly by two ways: altering membrane potential and inhibiting ATP[4] synthase activities, indicating a general decline in metabolism; and hindering the subunit of ribosome for tRNA binding, which in turn culminates on collapse of the biological process. Gold NPs also increase the chemotaxis[5] in an early phase reaction. Even though the ROS generation is the cause of cellular death for most bactericidal compounds (i.e. ZnO, TiO_2 NP's) against microorganisms, in the case of Au NP's this doesn't apply, which could explain the reported low toxicity of gold NP's to mammalian cells.

Lima et al. [123] studied the bactericidal effect of Au NP's with distinct SSA and fractal geometry concluding that size, roughness and dispersion of the Au NP's on the medium are physical properties with high influence in bactericidal properties.

2.6 Review on silver and gold as antibacterial materials

Silver has been known for its antibacterial properties and studies are being developed on its addition either as a micro or nano – scale entity in a variety of material implants. For instance, silver coating was deposited by galvanic deposition on titanium-vanadium implant with a thickness ranging from 10 to 15 μm and showed positive antibacterial results [100,124]. X. Zhang et al. [125], studied the addition of Ag (2.05 wt.%) to titanium to form a antibacterial coating by a duplex-treatment combining magnetron sputtering and micro-arc oxidation, which eliminated *E.colli* in 24h and noticed that the elimination rate increased gradually with time. Y. Dong et al. [126] experimented a duplex plasma surface alloying technique which combine high temperature double glow plasma silvering trialled on SS surfaces. In this study, Gram-negative *E. coli* and Gram-positive *S. epidermidis* were reduced by over 97% and 90% within 6 h.

---

[4]ATP (Adenosine Triphosphate): Intracellular energy source by all living organisms which plays a central role in the respiration and metabolism, this molecule is extremely valuable to all cells [183].
[5]Chemotaxis: Mechanism by which bacteria efficiently and rapidly respond to changes in the chemical composition of their environment [122].

Silver nanoparticles exhibit strong bactericidal activity against both gram positive and gram negative bacteria including multi resistant strains [109,127]. They are widely used in wound dressings [128,129], in catheters [129,130], orthopedic implants and fixations [131,132] and several commercial products [133,134]. Ag NP's applications includes its incorporation in different materials families (e.g. polymeric [135]/textile [136]) , also as nanocoatings [137] or as additive on Zirconia surface [138].

Several studies have been done on the antibacterial properties of silver nanoparticles, Yadollahi et al. [135], prepared antibacterial nanocomposite hydrogels through in situ formation of Ag NPs (size inferior to 50 nm) within the polyme. Although the results showed antibacterial results against E. coli (gram-negative) and S. aureus (gram-positive) bacteria, the nanohybrid stability was only guaranteed for 1 month. G.M. Raghavendra et al. [136], impregnated Ag NP's (size of 4 ± 2 nm), obtained by green synthesis of $AgNO_3$, into cellulose fibers and obtained positive results against *E.coli*. This study resulted on a better antibacterial effect than the work carried out by Ravindra et al. [139] which obtained higher NP's size (20 nm), also by a green synthesis process. S.B. Sant et al. deposited an Ag film (grain size 15 nm) by physical vapor deposition (PVD) from which they concluded that the physical nature of the silver crystallites, in the form of nanocrystals, as well as their association with Ag–O superoxides and line defects like twins are crucial for bactericidal efficacy [137]. K. Xu et al. [138], added Ag NP's (10-50 nm) on Zirconia (Y-PSZ) surface by a chemical-reduction-based coating technique and succeeded to inhibit early bacterial adherence against *E. coli, S. mitis and C. alibicans*. In this study, they concluded that NP's can provide a large reservoir of silver ions (Ag^+) which can be released gradually and result in long-term antimicrobial activity, on contrary to implant materials filled with silver-ion which display fast Ag^+ release.

Although some studies had reported higher efficiency of silver nanoparticles compared with gold nanoparticles [57,140], there are other studies that reported toxicity related with the use of silver nanoparticles [141,142], however, this aspect is not fully studied. In this context gold nanoparticles becomes a promising alternative.

Au NP's biocide potential have already been tested against bacteria and demonstrated positive results [57,143,144]. In addition, some studies related with gold nanoparticles applied to cancer diagnosis and treatment [145] has given strong evidences of the low toxicity of these particles [122,144]. Regarding biomedical applications, T. Russo et al. [111] studied the mechanical and antibacterial activity of PMMA-based bone cement loaded with gold

nanoparticles (10-20 nm) and the addition of only 1 %wt of gold caused a reduction on live bacterial cells of 50 %. However, to the authors' knowledge, no significant studies exist focused on the application of these nanoparticles on implant materials, especially when using zirconia as substrate.

2.7 Laser technology

Laser technology has emerged in recent years with potential for application in material engineering in operations such as machining (eg. cutting, drilling), forming (rapid prototyping), joining (eg. welding, brazing), surface modification (eg. hardening, texturing) and material deposition (sintering) [146]. It has been used in the processing and treatment of metals [147,148], polymers [149] and ceramics [146,150,151].

The generation of a laser beam is based on the principle of light amplification by stimulated emission of radiation, hereafter the acronym "LASER". Currently, there are different types of lasers used in surface treatment or processing of materials, including solid state lasers which is solid crystals (e.g. Nd: YAG lasers, Ti – sapphire, fiber lasers) or gas lasers (CO_2, excimer lasers) [152]. In addition, a laser can operate by emitting a continuous wave, as is the case of CO_2 laser or pulsed mode such as Nd: YAG (Neodymium-doped Yttrium Aluminum Garnet laser). In continuous mode lasers, a light is emitted continuously (energy is constant), while in a pulsed mode laser there is a period in which this one turns off between successive pulses of energy, resulting in an intermittent cooling period. Pulsed lasers can operate with nanosecond (10-9 seconds), picosecond (10-12 seconds) or femtosecond (10-15 seconds) energy pulses [153].

Laser complexity during processing is associated with its dependence on laser parameters, on material chemical and physical properties as well as on the interaction between the laser beam and the surface. Figure 10 shows some of these process variables [152].
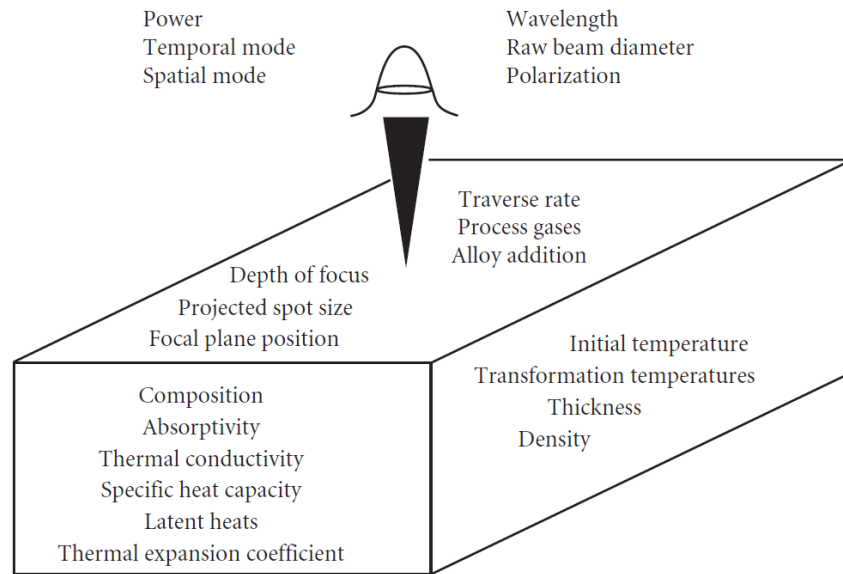
Figure 10 Laser beam and material lateral view point showing the principal process variables of laser material processing. Extracted from [152].

With respect to laser material interaction, during laser processing, three different mechanism can take place according to the laser density: heating, melting, and evaporation, as shown in Figure 11. The vital parameters governing this interaction are dependent on the properties of the material, such as reflectivity, thermal conductivity, specific heat, latent heat of fusion and evaporation [152,153].
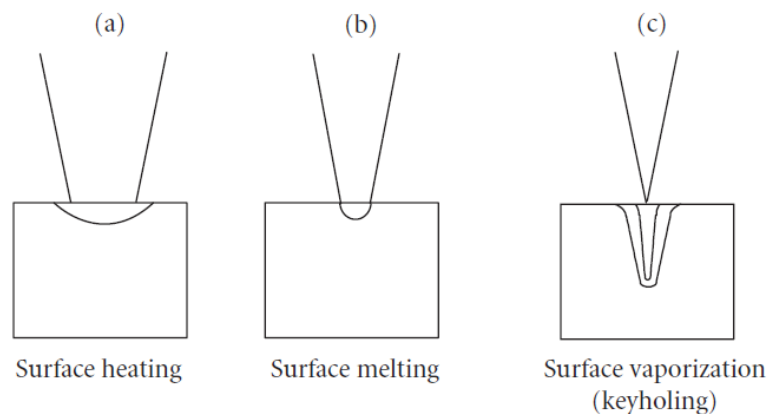
Figure 11 Illustration of the three distinct effects of increasing power density on the interaction between a laser beam and a material under steady state conditions. Extracted from [152]

Each laser has a characteristic wavelength which means that the type of laser to be used should be selected according to the absorption characteristics of the material to be processed. In this work, solid crystal Nd: YAG laser, was used on three different experiments: the multipurposed texturing of Y PSZ samples, being the most suitable laser for processing of ceramic powders [152,154,155], on sintering of the Ag powder on Y-PSZ surface since it is referred as an appropriate type of laser for melting of this metal [156–158] and finally on the

gold NP's manufacturing [159–161]. On the other hand, Au NP's were deposited on Y-PSZ surface using the gas state CO_2 laser technology referred in literature on the processing of metals [162–165]. A description of the process of laser ablation and of laser sintering is given on the two following topics.

2.7.1 Laser ablation (LA)

For better understanding the effect of the adjusted parameters on the further experiments follows an explanation of the way of action of Nd:YAG laser. Also, a brief explanation on the mechanisms behind NP manufacturing by laser ablation.

Ablation occurs when a material is exposed to an energy level greater than the binding energy of the ions in a lattice or in a molecule. Therefore, the amount of energy that is needed to remove a certain level of material depends highly on the ion and electron-configuration of the target material. This energy is the most important parameter for laser processing, since it is directly correlated to the ablation rate and thus to the formation of micro-structures. Energy input is commonly described, in association with time of exposure or a reference area, by intensity (W/cm²), fluence (J/cm²) and power (W) [166].

As previously mentioned, laser Nd:YAG works on pulsed mode, Figure 12 illustrates the scanning laser performance as well as the pulse overlap in the x and z direction. This overlap is necessary when texturizing with a scanning Gaussian beam as it compensate for the decreasing energy towards the tails of the distribution, leading to an homogenous energy exposure of the target surface [166,167].
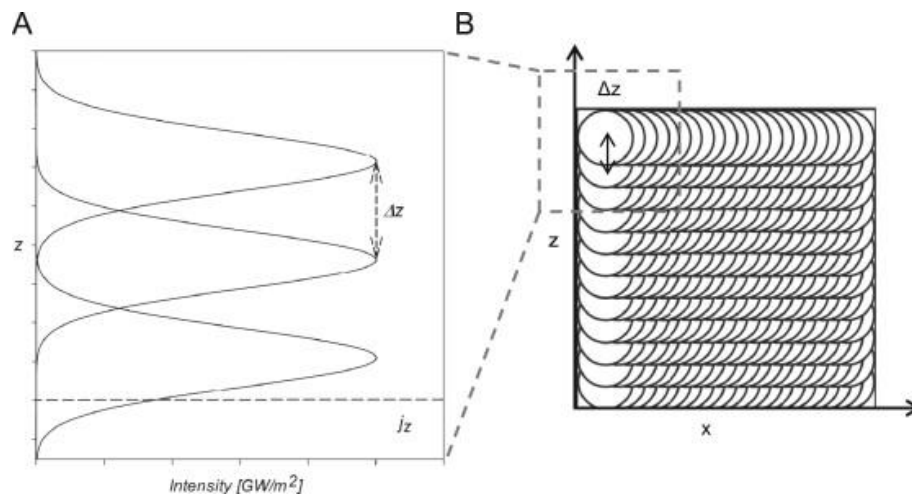
Figure 12 Schematic of overlapping during x and z direction in laser scanning to form a pattern (B), and the energy intensity distribution of the z direction scanning (A). Extracted from ref [166].

Additionally, laser ablation corresponds to a nanoparticle production method for a wide range of material classes and can take place in two distinct environments: in a vacuum or gaseous environment or in a liquid medium. The liquid medium laser ablation (LAL) was first applied less than 20 years ago to fabricate a colloidal solution of metallic nanoparticles and it is currently used [160,161,168]. The LAL is different from gaseous medium laser ablation because the liquid allows to control certain parameters and also have further effect on the morphology and microstructure of the resultant particles, like particle shape and size [169,170].

In this process, a laser beam penetrates the solid surface of the material, named *the target* (Figure 13). The depth of the penetration depends on the laser wavelength and on the refraction index of the target. When the radiation interacts with the target, an electrical field forms with enough energy to remove electrons from the bulk material. These electrons travel within the electromagnetic field and collide with the atoms of the target transferring some energy to the lattice. Once the matter becomes sufficiently hot to melt, forms a plasma containing atoms, molecules, electrons, ions, clusters, particulates and molten globules, with elevated temperature, high pressure and high density. The pressure difference between the produced plasma and the involving ambient results on an instant expansion of the plasma followed by a cool down. Finally, after the ideal condensation temperature and pressure, the plasma species nucleate and grow to form nanostructured entities [170,171].
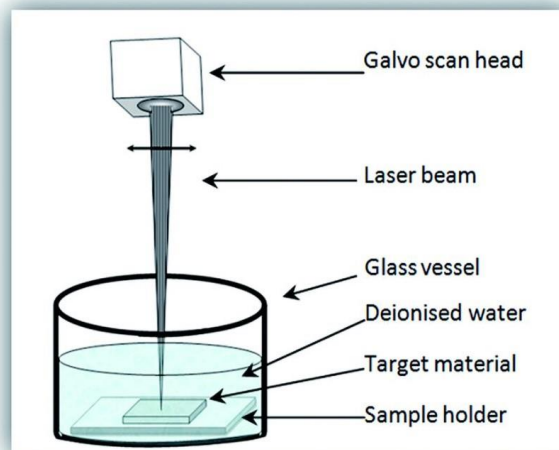
Figure 13. Schematic representation of laser ablation technique in liquid media [172]*.*

2.7.2   Selective laser sintering (SLS)

Laser sintering is an additive manufacturing process and is one of the leading commercial processes for rapid fabrication. In this process a high energy beam is emitted by the laser to sinter the material in the previously drawn (in CAD-computer assisted design software) areas and, sequentially, to sinter the material layer by layer. The sintering occurs through the heat generated by the laser beam when it is oriented, using a beam deflection system, to the place where the powder substrate is [173,174]. During this interaction, the temperature increases causing the brown state particles to be sintered and a solid layer is formed (Figure 14).
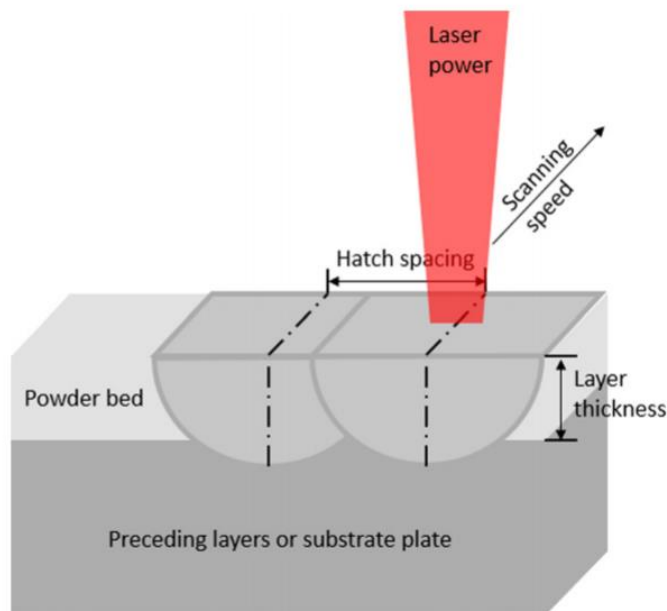
Figure 14 Illustration of the laser sintering additive manufacturing process [175]*.*

CHAPTER 3

EXPERIMENTAL METHODOLOGIES

The materials and methods used in the experimental part of this work will be explained in detail in this chapter. For better understanding the organization, the schematic outline presented on Figure 15 serves as a practical work guide.

Experimental Methodologies
Chapter 3

▼

Materials *(3.1)*

↓

Samples preparation *(3.2)*

↓

Surface treatment *(3.3)*

Physical barrier

Biocide effect
Green YPSZ   *Sintered YPSZ*

Green YPSZ

Laser microtexturing
(3.3.1)
via laser ablation (Nd:YAG)

**Micro
functionalization**

**Nano
functionalization**

Sintered YPSZ

Groove profile study
(3.3.1.1)

**Laser microtexturing
(to enhance Ag adhesion)**
(3.3.1.2)
via laser ablation (Nd:YAG)

Au NP's production
(3.3.3)
via laser ablation (Nd:YAG)

Sintered YPSZ

Sintered YPSZ

Ag micro-functionalization
(3.3.2)
· Deposition by powder pressing;
· Sintering via Nd:YAG laser.

Au nano-functionalization
(3.3.4)
· Deposition by spray and by irrigation;
· Sintering via CO_2 laser and in the oven

Surface Characterization
*(Physical, Structural, **Chemical, Mechanical**)*

- SEM - Surface roughness - Mechanical interlock test (artificial soft tissue)	- Ultrasonic Test - SEM - Friction Test - EDS	Ultrasonic Test - SEM - Friction Test - EDS

Figure 15 Flowchart of this work experimental methodologies.

3.1 Materials

This subchapter approaches the materials used in the experimental part of this work. The material used as substrate is described in section 3.1.1 and the added materials in section 3.1.2 and 3.1.3. Some characteristics of each material will be described in detail, such as chemical composition and relevant properties.

3.1.1 Zirconia (Y-PSZ)

The biomaterial used as subtract was Zirconia Partially Stabilized with Yttria (Y-PSZ) (Yttrium Oxide [3 mol%]) as powder (TZ-3YB-E Tosoh, Tokyo, Japan). The qualitative and quantitative chemical composition, as well as, some of this material physical properties are presented on Table 2 and Table 3, respectively, according to the supplier datasheet. The SEM images of the Y-PSZ powder are presented in Figure 16. It shows that the powder is composed of spherical agglomerates of nanosized particles.

Table 2 Chemical composition of the Y-PSZ powder (TZ-3YSB-E, Tosoh, Tokyo, Japan) according to supplier datasheet.

Chemical composition (wt.%)	
$ZrO_2 + HfO_2 + Y_2O_3$	> 99.80
Y_2O_3	5.15 ± 0.20
A_2O_3	≤ 0.10
SiO_2	≤ 0.02
Fe_2O_3	≤ 0.01
Na_2O	≤ 0.04

Table 3 Physical properties of the Y-PSZ powder (TZ-3YSB-E, Tosoh, Tokyo, Japan) according to supplier datasheet.

Physical properties	
Specific surface area (m^2/g)	7 ± 2
Particle size – D_{50} (μm)	0.60
Density after sintering (g/cm^3)	6.05
Coefficient of thermal expansion ($10^{-6}/K$)	10.50
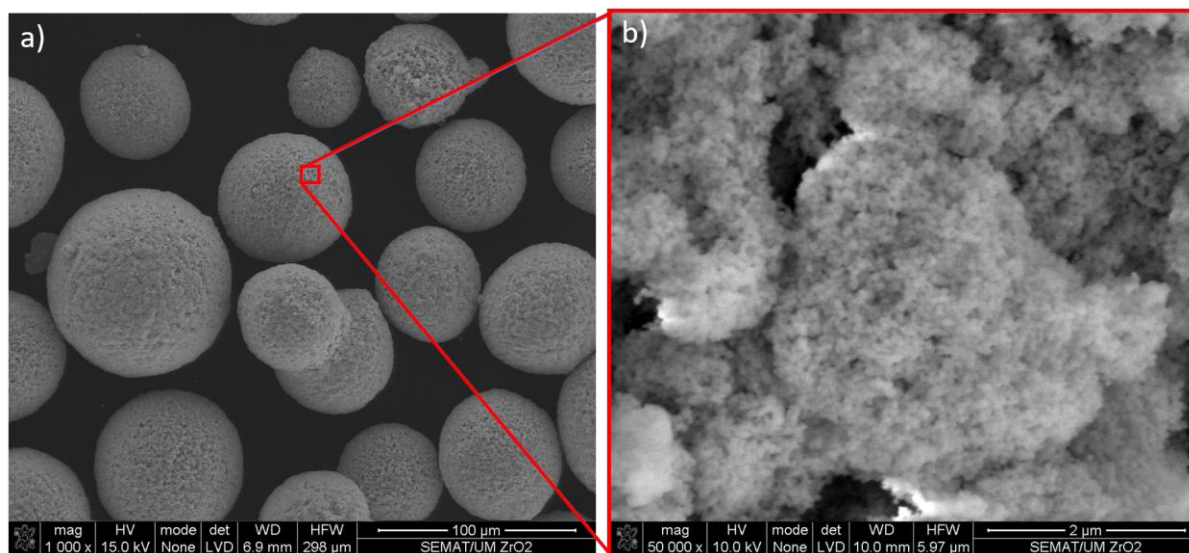
Figure 16 SEM images of the zirconia powders at a) 1000 X and b) 50000 magnification.

3.1.2   Silver (Ag)

Regarding the chemical surface functionalization, a silver (Ag) powder from Metalor, USA with an average grain size of 1.194 µm was used. The powder chemical composition and some of the powder physical properties, provided by the supplier, are presented in Table 4 and Table 5. This powder is characterized by an irregular morphology, as shown in SEM images presented in Figure 17.

Table 4 Chemical composition of silver powder (Metalor, USA), according to the supplier.

Chemical composition (wt.%)	
Cl	–
Cd	–
Cu	0.0375
Fe	0.0032
K	–
Na	–
Ni	–
Pb	–
Zn	–

Table 5 Physical properties of silver powder (Metalor, USA), according to the supplier.

Physical properties	
Specific surface area (m^2/g)	5.369
Particle size – D_{50} (μm)	1.194
Tap density (g/cm^3)	3.1
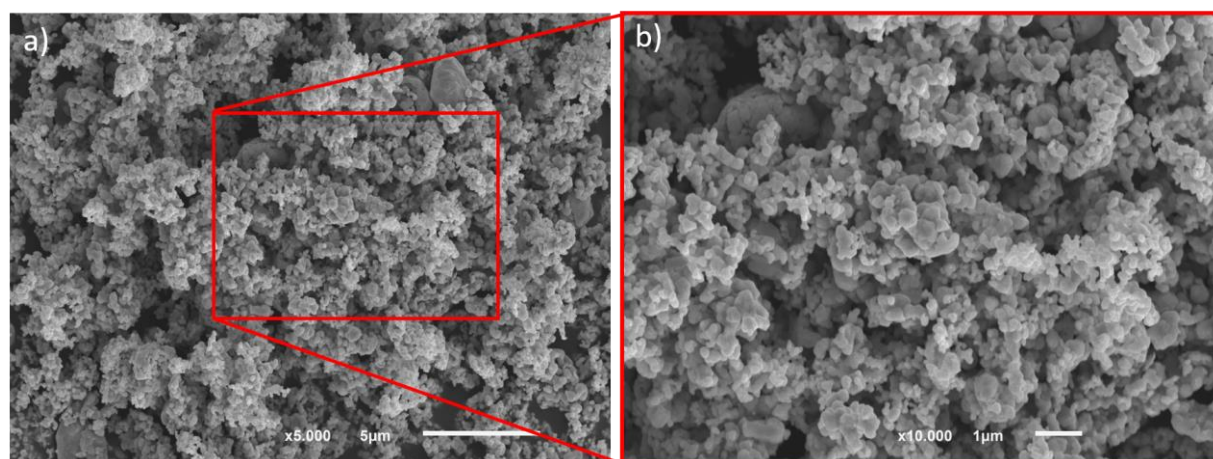
Figure 17 SEM images of the silver powders at a a) 5000 X and b) 10000 magnification.

3.1.3   Gold (Au)

Gold was added on zirconia surface as a nanoscale entity. The nanoparticles were obtained by the ablation of an Au plate in liquid medium. Considering this, for the NP's

production an Au rectangular plate (1 mm of thickness with 99.99 % purity) was used. The Au plate used in this experiment is presented on Figure 18.
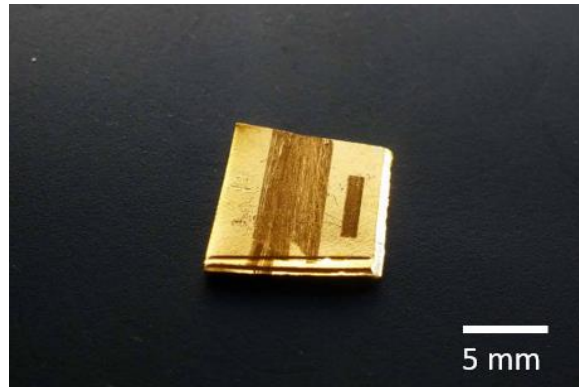
Figure 18 Au plate used in laser ablation experiment.

3.2 Samples preparation

The raw material used in this experiment was Zirconia Partially Stabilized with Yttria (Y-PSZ). The zirconia samples were produced by powder metallurgy (PM), in a two-steps process: a) powder/cold pressing and b) powder sintering. Two Y-PSZ discs with different dimensions were used as samples in this work, S1 and S2. The procedure of samples production is summarized in Figure 19.
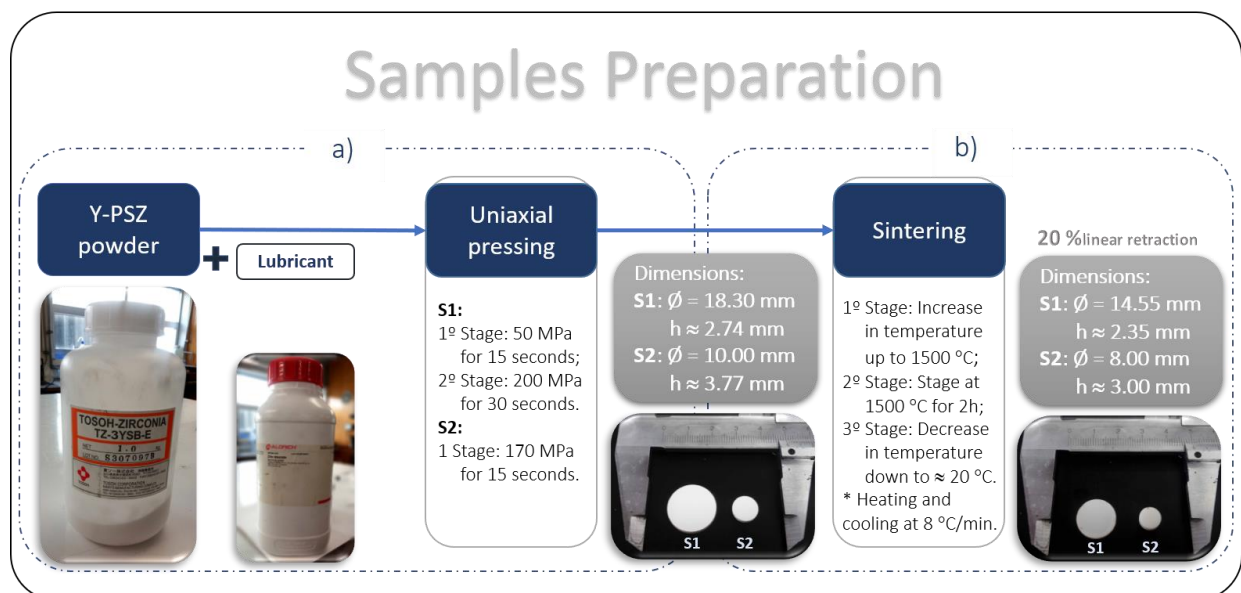
Figure 19 Scheme of the methodology adopted in the production of the zirconia samples S1 and S2.

a) Powder pressing

In powder pressing, the zirconia powder is compacted to increase the proximity between particles and prepare them to be sintered. For the production of sample 1, 2 g of zirconia was used and for the production of sample 2, 0.9 g.

The zirconia powder was weighed and introduced on a stainless-steel mould, previously lubricated with zinc stearate (powder/solid lubricant). The powder was, then, cold die pressed with a stainless-steel punch by unidirectional pressing (single action). In the case of sample 1 with a pre-pressure of 50 MPa for 15 seconds followed by a final pressure of 200 MPa for a period of 30 seconds. For sample 2, a one stage pressure of 170 MPa for 15 seconds. The equipment used in this experimental procedure is presented on Figure 20.

Figure 20 Hydraulic press equipment MEGA, Spain (micro fabrication and systems integration laboratory (CMEMS) of the Mechanical Engineering Department of University of Minho).~

b) Powder sintering

Sintering is a thermal process in which the main objective is to produce a strong bond between the powder particles and consequently to achieve the optimal density.

This step occurs after the compression of the ceramic powder. Therefore, the green compact is afterwards sintered in an oven, Zirkonofen 700 ultra-vacuum, Italy, (Figure 21a)

for 2 h at 1500 °C, in air, with a heating rate of 8.3 °C/min. The sintering cycle adopted in the Y-TZP samples processing is represented in Figure 21b.
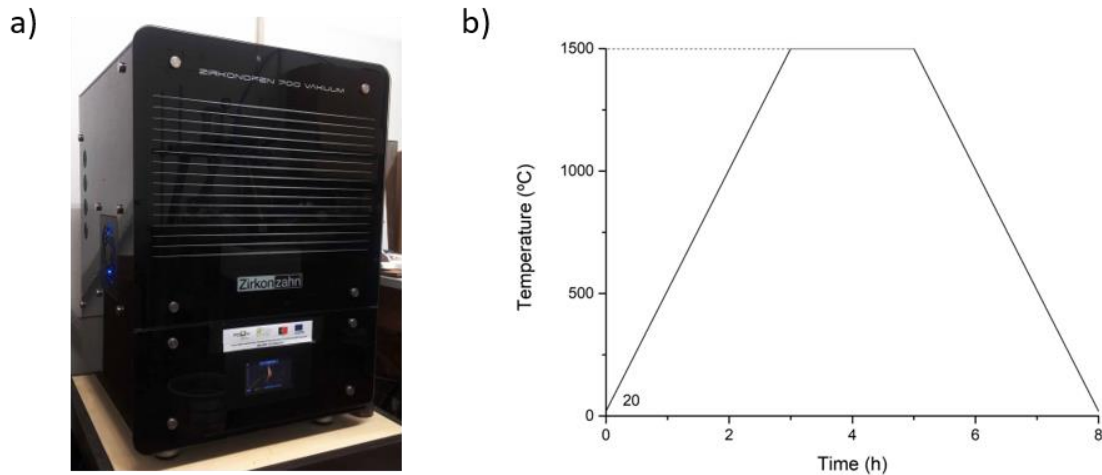
Figure 21 Information on the sintering process of zirconia samples: a) oven used in the sintering of zirconia samples (CMEMS Laboratory of the Mechanical Engineering Department of University of Minho), b) sintering thermal cycle used in the processing of the samples.

After sintering, the processed samples were finally cleaned on the ultrasonic equipment, for 8 seconds, and left to dry on air. The samples calculated volume retraction was approximately 45 % while its linear retraction was of $\approx$ 20 %.

3.3 Surface treatment

This subchapter comprises a detailed description of the surface treatments applied to accomplish with the objectives of the present work. Hence, the first topic describes the methods used in the development of micro-textures through laser technology. The following topic is related to all the procedure used for the silver surface micro-functionalization. And the two last topics are dedicated to the gold nano-functionalization procedure in which the first step comprises the production of the NP's and the second the respective deposition.

3.3.1   Surface micro-texturing via laser Nd:YAG laser

This section presents all the experimental information related with Y-PSZ surface texturing that was relevant on the study of the groove depth, groove width and groove interspacing, as well as, information on texturing to achieve Ag adhesion on Y-PSZ surface.

The micro-texturing was performed on the Y-PSZ surface under green state.

A Nd:YAG (OEM 60 Plus, Sisma, Italy) pulsed laser was used to produce micro-textures on Y-PSZ surface. It belongs to the category of solid-state lasers, emitting a radiation at a wavelength of 1064 nm. The laser is equipped with a computer holding version 0.91 of the software Inkscape that allows to draw in two dimensions (2D) the textures to be produced. The software Sisma Laser Controller (SLC) allows to control and execute the laser process, as well as to define the laser parameters to produce the textures. Additionally, a forced air-cooling system is also accoupled to spread resultant powder released from textures production, and to avoid powder accumulation in the zirconia surface which can interfere with results. Figure 22 reveals the laser setup used in this work and Table 6 its technical characteristics.
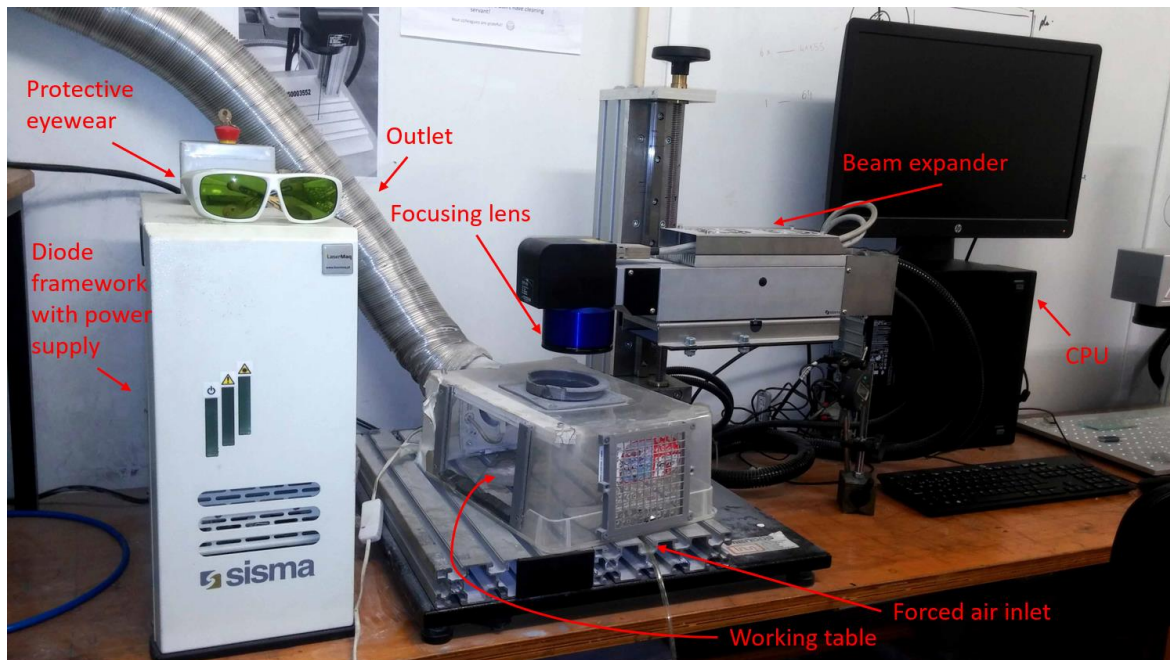
Figure 22 Laser system setup used in the experimental work (CMEMS Laboratory of the Mechanical Engineering Department of University of Minho).

Table 6 Technical specifications of the Nd:YAG OEM 60 Plus laser, according to the manufacturer.

Laser	Nd:YAG
Wavelength (nm)	1064
Maximum power (W)	6
Spot Size (mm)	0.003
Pulse width (ns)	35
Repetition rate (kHz)	20

The laser parameters controlled in this work were, number of scans (N), speed (mm/s), and number of lines (N). The other laser parameters were kept constant. For better understanding of the meaning of each laser parameter a brief description is presented:

- ❖ Laser power: laser beam energy, in Watts, delivered per pulse;
- ❖ Passes: number of scans carried out by the laser during processing;
- ❖ Scan speed: represents the marking speed, in mm/s, at the front edge of the beam;

In addition, it was required to include the study of two parameters related with the 2D drawing on Inkscape (v0.91) software. The 2D drawing also influences the microgrooves characteristics. The drawing parameters studied were the number of drawing lines (nº of lines) and the space between them (lines interspacing).

3.3.1.1.   Micro-grooves

This topic comprises the study of the laser parameters influence in the texturized groove depth, width and groove interspacing.

Initially, a study focused on laser parameters influence on groove depth and width was performed. Then, based on the best previous laser parameters, considering literature study on epithelial cell attachment, a study of interspacing groove between 25 and 100 µm was realized. Illustration from Figure 23 helps on the understanding of the groove dimensions previously referred and Table 7 and Table 8 summarize all combinations of the tested laser parameters where a laser power of 1.5 W was used.
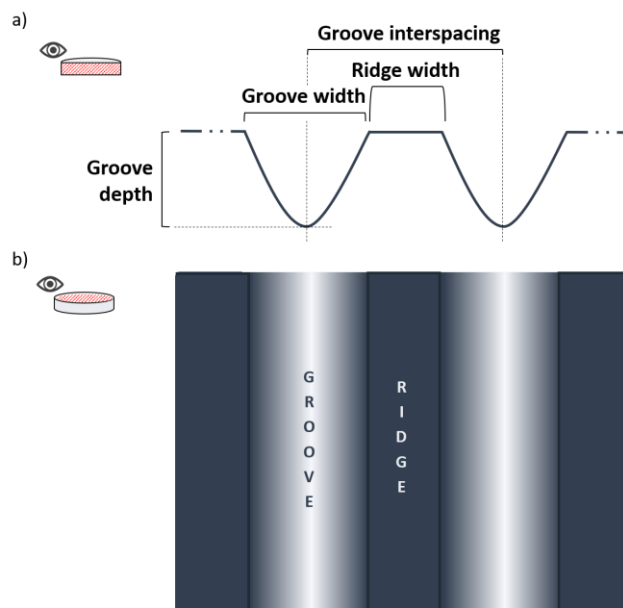
Figure 23 Representation of the cross-sectional view (a) and top view (b) of the projected micro grooved textures, with the corresponding structural nomenclature used in this dissertation.

Table 7 Laser parameters used on Nd:YAG laser for the depth and width study of the produced micro grooves.

Laser parameters		2D drawing	
N° of scans (N)	Speed (mm/s)	N° of lines (N)	Sample CODE DESIGNATION
1	128	1	N1 S128 L1
		2	N1 S128 L2
		4	N1 S128 L4
		8	N1 S128 L8
	256	1	N1 S256 L1
		2	N1 S256 L2
		4	N1 S256 L4
		8	N1 S256 L8
2	128	1	N2 S128 L1
		2	N2 S128 L2
		4	N2 S128 L4
		8	N2 S128 L8
	256	1	N2 S256 L1
		2	N2 S256 L2
		4	N2 S256 L4
		8	N2 S256 L8
4	128	1	N4 S128 L1
		2	N4 S128 L2
		4	N4 S128 L4
		8	N4 S128 L8
	256	1	N4 S256 L1
		2	N4 S256 L2
		4	N4 S256 L4
		8	N4 S256 L8
8	128	1	N8 S128 L1
		2	N8 S128 L2
		4	N8 S128 L4
		8	N8 S128 L8
	256	1	N8 S256L1
		2	N8 S256 L2
		4	N8 S256 L4
		8	N8 S256 L8

Table 8 Inkscape 2D drawing lines interspacing values used on the study of groove interspacing.

2D drawing
Groove interspacing (µm)
25
30
35
40
50
60
70
80
90
100

A general representation of a drawing is presented on Figure 24 to ease the understanding of the 2D drawing parameters studied: number of lines (N) and groove interspacing (µm).
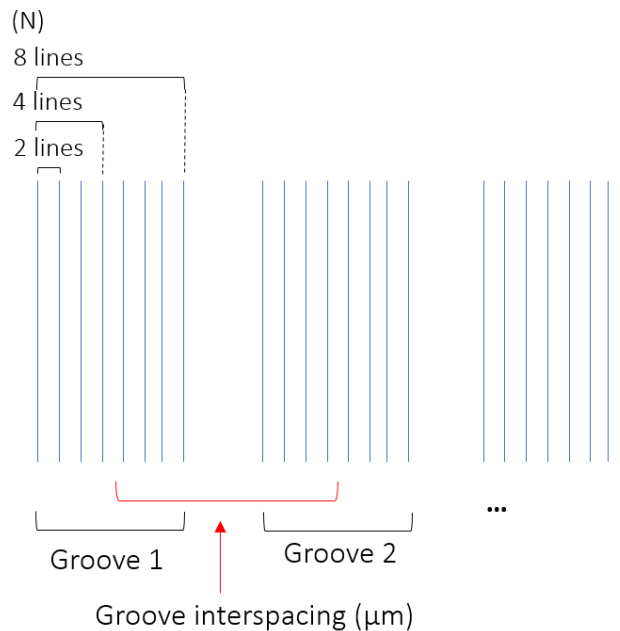
Figure 24 Representation of the drawing corresponding to a group of grooves composed by 8 successive lines.

Next step, after laser micro texturing process, was powder sintering. The samples were sintered using the thermal cycle presented in Figure 21. The produced samples with the microgrooves were then analysed in cross section by SEM to assess the final dimensions. To accomplish this, samples were transversely cut with a *gravimeta* diamond cutting disc (see Figure 25) and polished (up to P4000 grit size SiC paper).

Figure 25 Diamond cutting disc used on the cross sectional cut of Y-PSZ samples (CMEMS Laboratory of the Mechanical Engineering Department of University of Minho).

With the study of the influence of laser parameters on groove width, depth and ridge width completed, it was possible to select a set of conditions and to reproduce a series of microgrooves per sample in order to test the influence of each groove dimensional parameter on the adhesion strength between the texturized sample and artificial soft tissue. The selected parameters for the adhesion test were selected based on the resultant groove dimensions. A detailed description is presented in next chapter.

3.3.1.2.   Pre-treatment for Ag micro-functionalization

This procedure is also a micro texturing experiment but with a different purpose from the previous topic. Here, the aim is to create a surface that promotes the adhesion between the substrate (Y-PSZ) and the deposited material (micro Ag). To accomplish this, two different patterns were created, a fine pattern and a coarser pattern, to determine the best alternative to improve the adhesion between the two materials. Table 9 presents the laser parameters used in each pattern.

Table 9 Laser parameters used on the pre-treatment of zirconia surface.

	Laser parameters			2D drawing
Pattern	**Power (W)**	**Nº of scans (N)**	**Speed (mm/s)**	**Nº of lines (N)**
Fine	0.18		32	1
		1		
Coarse	5.10		100	8

3.3.2 Silver surface micro-functionalization

Silver (Ag) functionalization protocol involved the assembling of two maind experiments. First the Ag powder deposition by powder pressing, and second, the sintering of the Ag layer via Nd:YAG laser. These 2 main steps will be explained in with detail in the following two topics.

Illustration from Figure 26 represents, step by step, what is expected to happen with the combination of these two materials, from a top view and also from a cross view, where it illustrates:

(1) the substrate immediately before the deposition;

(2) the substrate with the coating after cold pressing;

(3) the powder which penetrated the texturized substrate, after removing the excess;

(4) the Au-functionalized surface (after laser sintering).
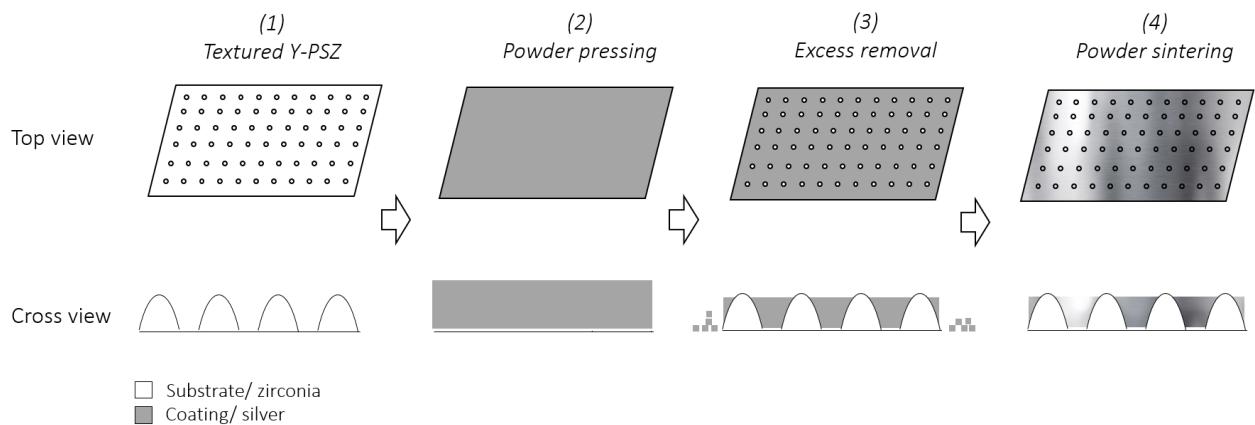
Figure 26 Schematic illustration of the sample appearance during the Ag functionalization process: (1) substrate immediately before the deposition; (2) substrate + powder after cold pressing; (3) substrate + powder after removing the excess powder.

3.3.2.1. Deposition by powder pressing

The micrometric Ag powder was deposited on each of the 2 different texturized and sintered Y-PSZ surfaces, ensuring that the surface was completely covered. Afterwards, the powder was cold pressed using the hydraulic press equipment (used previously, Figure 20) with a minor pressure of 8 MPa. A flexible polymeric sheet, 0.5 cm thick, was inserted between the sample and the press pin to ensure the penetration of the powder into the textures, as well as guarantee a homogeneous pressure distribution during pressing. Next step consisted of removing the excess of silver powder by polishing manually with a P600 grit SiC paper, until reaching the subtract.

3.3.2.2. Sintering via Nd:YAG laser

The two different texturized Y-PSZ samples with deposited Ag powder were subjected to a combination of Nd:YAG laser parameters. A concentric drawing composed of a succession of circles (one line per circle) was designed in Inkscape (v0.91) and applied in the sintering of all the samples. The respective drawing is presented in Figure 27.
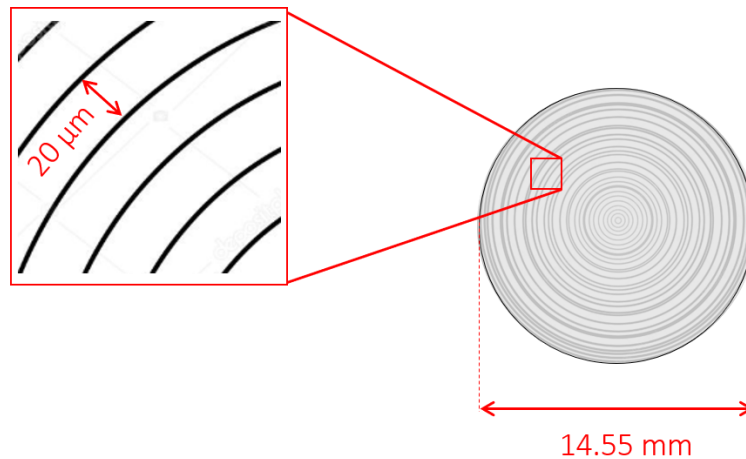
Figure 27 Schematization of the drawing used in Inkscape software on Ag laser sintering.

The studied laser parameters were: Power, scanning speed and number of scans. The remaining parameters were kept constant. Table 10 presents the parameters used on the study of Ag sintering on zirconia surface for both textures, fine and coarse. An argon flow was applied during laser processing.

After laser sintering, the samples were polished from P 600 up to P4000 grit sequence of SiC papers.

To complete Y-PSZ silver functionalization experiment, silver adhesion to the substrate was tested by ultrasonic cavitation test. This test was performed in all the samples. The procedure is described with more detail in next chapter, *Materials characterization*.

Table 10 Laser parameters used on the sintering via laser of Ag powder.

Power (W)	N° of scans (N)	Speed (mm/s)	Sample CODE DESIGNATION
6	1	64	P6S64N1
		128	P6S128N1
		256	P6S256N1
		400	P6S400N1
	4	64	P6S64N4
		128	P6S128N4
		256	P6S256N4
		400	P6S400N4
3	1	64	P3S64N1
		128	P3S128N1
		256	P3S256N1
		400	P3S400N1
	8	64	P3S64N8
		128	P3S128N8
		256	P3S256N8
		400	P3S400N8
1.5	4	32	P1.5S32N4
		64	P1.5S64N4
	12	32	P1.5S32N12
		64	P1.5S64N12

3.3.3 Gold nanoparticles (AuNP's) production by laser ablation

Before starting with the ablation process, the Au plate was cleaned with isopropanol followed by distilled water, dried in cold forced air and weighted in a precision scale.

An Au plate was used as target on the laser ablation process in which the Nd:YAG laser (OEM Plus, Italy) operated with a laser power of 0.3 mJ/pulse [176]. It operated with a scanning speed of 5 mm/s and 1 scan.

The target was fully immersed on a glass vessel containing 20 ml of an aqueous suspension with double distilled water (DDW) and sodium dodecyl sulfate - SDS ($C_{12}H_{25}SO_4Na$, Alfa-Aesar) used as a surfactant. The suspension was prepared by adding pure SDS powder to DDW, in a concentration of 0.025 mol/L, and mixed carefully. With the ablation process

initiated, the liquid was gently stirred to push the ablated particles out of the laser beam and allow the removal of more material.

Three solutions of Au NP's were prepared following this method. Two with an ablated area of 20 mm^2 which corresponded to 11 min of laser processing (Figure 28a) and one solution with an ablated area of 5 mm^2 with a duration of 5 min and 30 seconds (Figure 28b). The solution produced through the ablation of a larger Au area present a darker shade than the solution produced with a smaller ablation area. Finally, the Au plate was weighed again to quantify the ablated material.
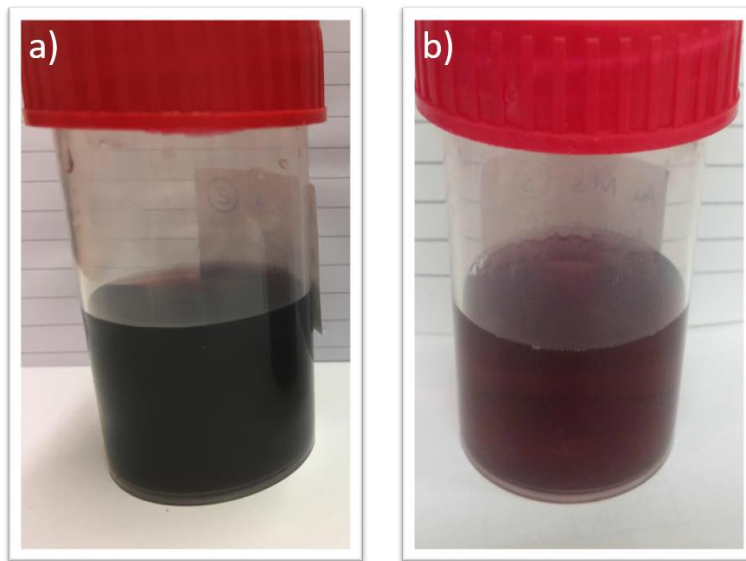
Figure 28 Au NP colloidal solution produced by laser ablation.

3.3.4   Gold surface nano-functionalization

Gold NP's Y-PSZ surface functionalization comprised two main steps:

1) the <u>deposition</u> of the Au manufactured NP, which was carried out either by:

a) Irrigation technique;

b) spray technique;

2) the <u>sintering</u> of the deposited NP's on zirconia surface, was achieved via:

a) oven;

b) CO$_2$ laser.

The deposition$\rightarrow$ sintering processing techniques combinations adopted in this work are presented in the scheme from Figure 29.
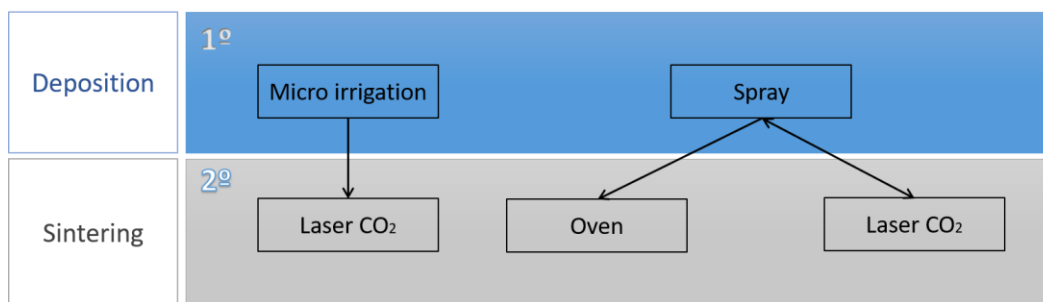
Figure 29 Schematization of the followed work line in Au NP's Y-PSZ surface functionalization.

As noted, 3 divergent experimental procedures were done, therefore, each will be explained in detail in each of the following topics.

3.3.4.1.   Deposition by irrigation and sintering via laser CO_2

This hybrid process consists on the irrigation by dropping the Au solution on the sample and then sintering by laser technology.

<u>Deposition by irrigation</u>

The method of deposition by irrigation and sintering via laser CO_2 was the first approach tested in the Au surface functionalization topic. Considering this, the substrate-laser interaction was studied during this procedure.

In this process, zirconia sample was heated on a hot plate until temperature of 75 °C aiming to evaporate liquid media (SDS) between each drop. At this temperature, a total of 20 drops ($\approx$0,46 ± 0,04 ml) of Au NP's solution were deposited (drop by drop) on the surface of the sample. Attention was taken on keeping the solution from draining out of the sample, to avoid wasting. Figure 30 shows photographs of the samples before (a), and after (b) the NP's solution deposition.
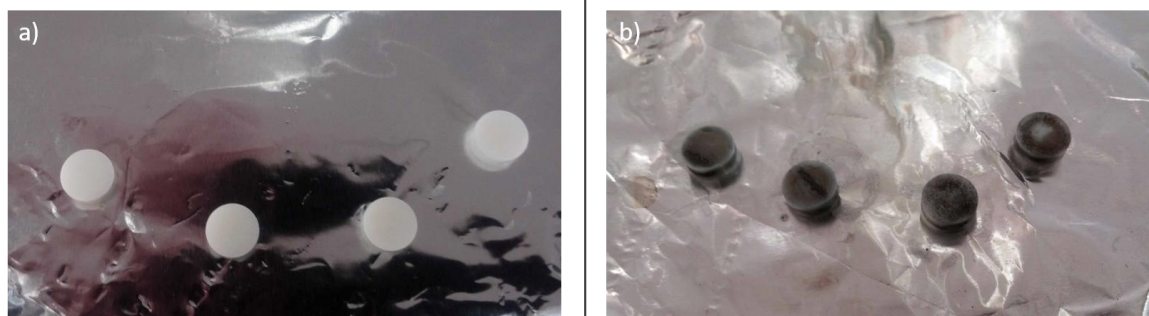
Figure 30 a) Y-PSZ samples before Au NP's deposition b) Y-PSZ samples after Au NP's deposition

Note that, initially, the temperature used for the deposition was 100 °C (water boiling point) although at the end of the procedure the sample presented cracks, therefore the temperature was intentionally decreased to minimize the temperature difference between the solution and the sample.

Sintering via CO_2 laser

After the Au NP's deposition, the sample was subjected to laser sintering. Before starting with sintering process, the sample temperature is increased to 470 °C in the heating plate, at that point the laser sintering process could begin. This increase in temperature is meant to reduce the thermal shock between the sample and the laser beam. Also, to avoid this problem, at the end of the procedure the sample was not immediately extracted from the plate but instead kept on for approximately 15 min, so that the cooling was constant.

The laser equipment used in this procedure was a CO_2 laser equipment BD-50C, Bende, China. It belongs to the category of gas lasers, emitting a radiation at a wavelength of 10640 nm. The laser equipment used is shown in Figure 31.

Figure 31 Laser system setup used in the experimental work (CMEMS Laboratory of the Mechanical Engineering Department of University of Minho).

The laser is connected to a computer by means of which it is possible to design the 2D draw needed on the laser processing and control the sintering parameters through the software EZ-CAD. The CO_2 laser technical characteristics are presented in Table 11.

Table 11 Technical specifications of the CO_2 BD-50C, Bende laser, according to the manufacturer.

Laser	CO_2
Wavelength (nm)	10 640
Maximum power (W)	50
Spot Size (mm)	0.02

Figure 32 illustrates the complete two-step procedure of deposition and sintering previously described.
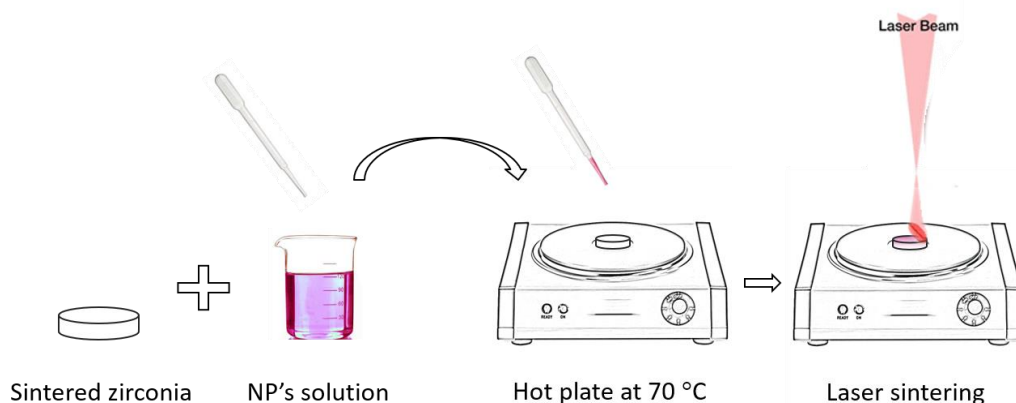
Figure 32 Schematic representation of the experimental procedure adopted in the Au NP's deposition by irrigation and sintering via CO_2 laser.

The CO_2 laser parameters optimized in the present work were: power (W), speed (mm/s), line spacing (mm), and the number of scans (N). Table 12 shows the conditions tested.

Table 12 CO_2 laser-processing parameters used on sintering of the deposited NP solution.

Test group	Sample	Power (W)	Speed (mm/s)	N° of scans (N)	Line spacing (mm)
1º	S1	15	500	3	0.1
	S2	15	500	3	0.1
	S3	15	500	2	0.1
	S4	15	500	2	0.1
2º	S1	7.5	1000	8	0.02
	S2	7.5	1000	16	0.02
	S3	7.5	1000	32	0.02
3º	S1	10	1000	2	0.02
	S2	12.5	1000	2	0.02
	S3	12.5	1000	2	0.06
4º	S1	10	1000	2	0.007
	S2	10	1000	2	0.01
	S3	11.5	1500	2	0.02

3.3.4.2.   Deposition by spray and sintering via laser CO_2

The combined process of spray deposition and laser sintering is, divided in two stages: first stage is composed of a set of purges (30 or 20) immediately followed by one laser scan, and the second stage an additional set of purges (30 or 40) followed by one last laser scan, as can be seen in Figure 33. Both processing steps will be explained in the two following topics.
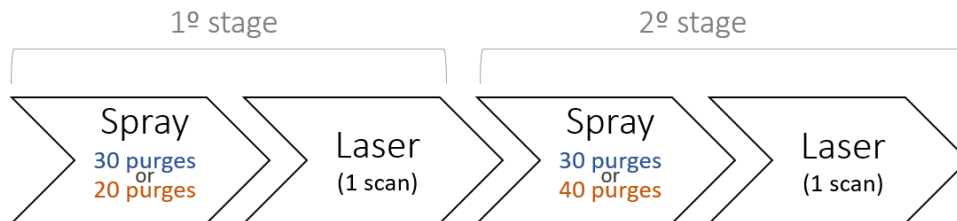
Figure 33 Schematic order of events of deposition by spray and sintering via laser CO_2 technique.

<u>Deposition by spray</u>

In a first stage of the NP's deposition by spray, 0.06 ml of NP's solution is introduced in the spray equipment dispenser. And After 60 purges, the sample proceeded to laser sintering process.

The equipment used to deposit the NP's solution was a Techcon Systems multi-purpose dispensing valve controller-TS500R, United Kingdom (Figure 34a), accoupled with a precision spray valve-TS5540 from the same manufacturer (Figure 34b). The selected output air pressure at the dispensing controller was 0.6 bar, the dispersion time 1 second and the distance between the sample and the valve disperser 35 mm. The flow rate was manually adjusted at the valve, until a visible finer deposition was attained. The quantification of the flow rate is not attainable with this equipment. These conditions were established after a primary analysis to all the equipment parameters.

Figure 34 Spray equipment combined of: a) a Techcon Systems multi-purpose dispensing valve controller-TS500R, United Kingdom; b) respective precision spray valve-TS5540, same manufacturer (CMEMS Laboratory of the Mechanical Engineering Department of University of Minho).

Sintering via laser CO$_2$

In this experimental procedure, the sintering step is carried out via CO$_2$ laser, under the exact same procedure as the one described in the topic 3.3.4.1. Figure 35 presents a general scheme of the deposition by spray and sintering via laser CO$_2$ process.
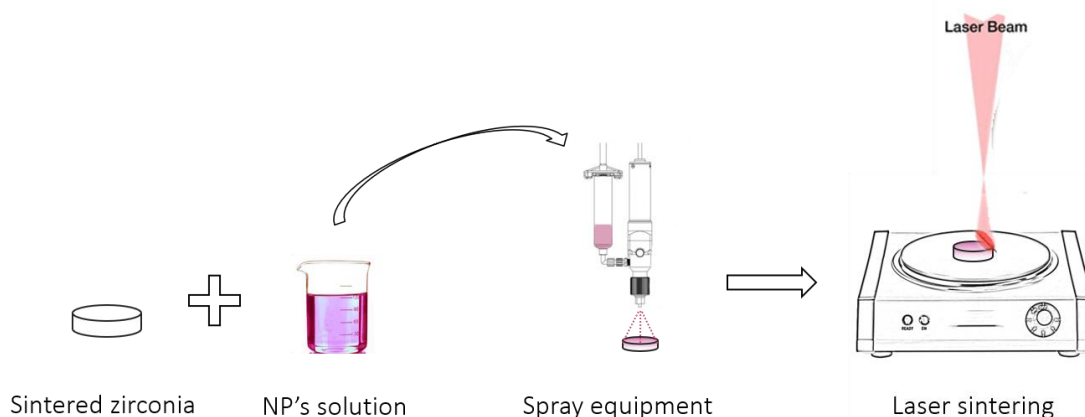
Figure 35 Schematic representation of the experimental procedure adopted in the Au NP's deposition by spray and sintering via CO$_2$ laser.

As it was mentioned on the beginning of the topic *Deposition by irrigation and sintering via laser CO$_2$*, the substrate-laser interaction was studied at that point, which allowed the selection and fixing of certain laser parameters as the number of scans (2), and the line spacing (0.02 mm). The laser parameters used in this experiment can be consulted on Table 13.

Table 13 Experimental conditions used on deposition by spray and sintering via laser CO$_2$.

Stages	Purges (1º/2ºstage)	Power (W)	Speed (mm/s)	Nº of scans (N) (1º/2ºstage)	Line spacing (mm)
1	60	11	1000	2	
		11.5	1500		
2	30/30	11	1000	1/1	0.02
		11.5	1500		
2	20/40	11	1000	1/1	
		11.5	1500		

3.3.4.3. Deposition by spray and sintering in the oven

In this Au NP's surface functionalization, the process of NP's deposition was carried out by spray and the sintering process was in the oven. Both processing steps will be explained in the two following topics.

Deposition by spray

In this experimental procedure, as in the previous technique, the deposition step is carried out by spray, which has the same parameters and conditions as the ones described in topic 3.3.4.2.

<u>Sintering in the oven</u>

Considering the information provided by the graphic from Figure 9 (previous chapter) about gold melting temperature at nanometric scale, the sample was placed in the oven at a temperature of 530 °C during 30 minutes in vacuum at 10^{-2} mbar. Figure 36 shows a scheme of the entire Au surface functionalization.

Sintered zirconia NP's solution Spray equipment Oven, T$_{máx}$= 530 °C (+ vacuum)
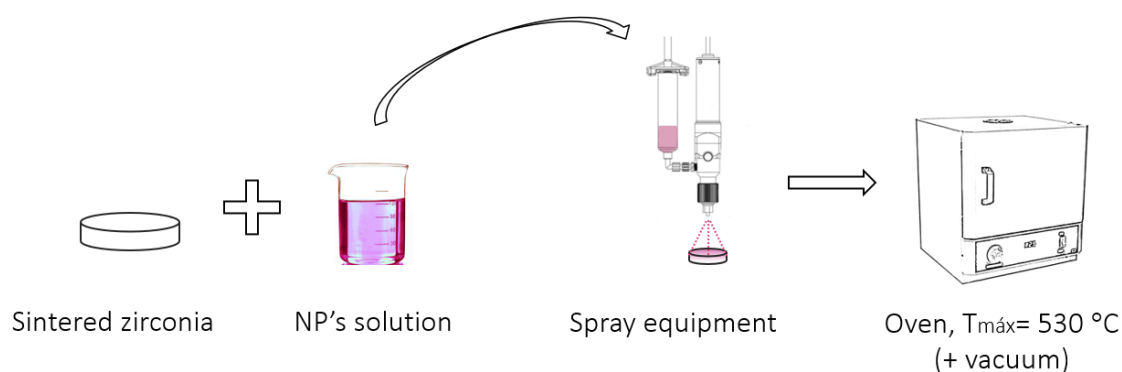
Figure 36 Schematic representation of the experimental procedure adopted in the Au NP's deposition by spray and sintering in the oven

3.4 Materials characterization

In this subchapter, the techniques used for the characterization of the produced materials will be presented and described. The evaluation of the materials and processing methods influence on the final properties aims to guarantee the success of the pre-established objectives of this work. These techniques comprise chemical, morphological, physical and mechanical material characterization.

3.4.1 Ultrasonic adhesion test

Ultrasound cavitation is described as a phenomenon of simultaneous and repetitive bubble formation, growth and implosive collapse of the bubbles in a liquid medium. In a heterogeneous solid/liquid system, the collapse of the cavitation bubble near the surface produces a rush of the fluid to fill the void, forming a liquid jet against the surface. These jets

causes a disruption of the interfacial boundary layers removing the material and occupying the active sites [177,178].

As a first approach on testing the adhesion efficiency between different materials, all samples were subjected to an ultrasonic cavitation test using an ultrasonic processor (UP200St, Hielscher, Germany), shown in Figure 37. The samples were submitted to a power of 100 W and a frequency of 40 kHz for 1 minute in a vessel containing isopropanol.

Figure 37 Ultrasonic processor, UP200St, Hielscher, Germany (CMEMS Laboratory of the Mechanical Engineering Department of University of Minho).

3.4.2 Optical microscopy

Optical Microscopy (OM) allows a fast visualization of surface features that are not discerned by the eye, making use of adequate magnification lens and visible light to expose the microscopic features of a surface. As a first approach for samples imaging an optical microscope (OM), hund H500, Helmut Hund GmbH, Germany equipped with a digital camera Leica DM 2500M, Leica Microsystems, Germany, was used (Figure 38). The treated samples were analyzed in order to evaluate the effects of the laser-processing parameters on the samples surface as well as to assess the NP's (agglomerates) presence.

Figure 38 Leica DM 2500M, Leica Microsystems, Germany (Mechanical Engineering Department of University of Minho).

3.4.3 Scanning electron microscopy and energy dispersive X-ray spectroscopy

Scanning electron microscopy (SEM) captures micrographs with extreme detail, resolution and depth of focus. The particularity of this technology is on the use of an electron beam, instead of visible light, that allows higher magnification imaging. From the interaction of the electron beam with the target material different types of species are released and, the detection and analysis of each, reveals different kinds of information's, for instance characteristic X-rays are used for elemental analysis, secondary electrons for image rendering of the topography and backscattered electrons for image rendering according to the atomic number and phases near the surface. This technology was required to evaluate the topographic changes of the different surface treatments applied on the samples. Additionally, an electron microprobe analyzer is used to realize chemical analysis in selected areas of the samples. In this way, energy dispersive X-ray spectroscopy (EDS) provided a qualitative and relative quantitative chemical composition data, for the gold NP's and for the silver functionalized Y-PSZ surfaces. The equipment used was a FEG-SEM; NOVA 200 Nano SEM, FEI, EUA (Figure 39).

Figure 39 FEG-SEM; NOVA 200 Nano SEM, FEI, EUA, with integrated EDAX - Pegasus X4M (EDS/EBSD) (Laboratory for Materials Characterization Services of the University of Minho (SEMAT))

3.4.4   Atomic absorption spectroscopy

Atomic absorption spectroscopy (AAS) is a technique that identifies and measures quantities of chemical elements present in a sample. This is achieved by measuring the radiation that is absorbed by the chemical element under study and reading the spectrum reproduced when the sample is excited by radiation. The qualitative analysis relies on the fact that every atom has a unique pattern of wavelengths at which it will absorb energy, due to the unique configuration of electrons in its outer shell. The quantitative analysis is based on the Beer Lambert law which relates the quantity of light absorbed with the quantity of metal present in the sample [179,180]. ASS was used to evaluate the presence of Au NP's in the solution produced by laser ablation using a UV–vis absorption spectrophotometer Model 2501 PC (Shimadzu).

3.4.5   Scanning transmission electron microscopy

Scanning transmission electron microscopy (STEM) combines the principles of scanning electron microscopy (SEM) with transmission electron microscopy (TEM). STEM peculiarity is in the analyses of transmitted electrons to determine the amount of energy they have lost in interactions with the sample, which is useful in investigation of the atomic and chemical composition, the electronic properties, as well as, local thickness measurements of materials. The advantage in the combination of TEM with SEM is in the correlation of signals,

namely, secondary electrons, scattered beam electrons, characteristic X-rays, and electron energy loss that cannot be spatially correlated in TEM. This technology offers higher magnification than SEM itself, therefore, it was required to determine the particle size distribution and shape of the Au nanoparticles produced. The observation of the nanoparticles was performed with a transmission electron detector Nova 200 Nano SEM operating at 20 kV (Figure 39). Two droplets of solution were deposited on carbon-coated copper grids and dried in air.

3.4.6 Contact surface roughness

Surface roughness was determined using a mechanic profilometer (Surftest SJ 201, Mitutoyo, Tokyo, Japan) following ISO 1997 standard. This measuring device is composed by a diamond stylus with 2 μm of diameter with measuring range capacity from-200 μm to 160 μm. The sampling length was 0.8 mm, at 0.25 mm/s. Three different regions were evaluated in each Y-PSZ sample, in the direction parallel to the scanning direction. The surface roughness was characterized by the arithmetic mean surface roughness (R_a) and average maximum peak to valley (R_z). Figure 40 shows the profilometer used on the present work during operation.
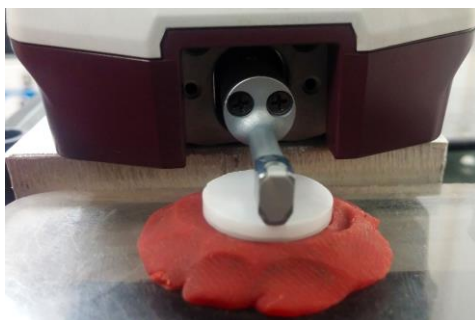
Figure 40 Surface roughness tester Surftest SJ-210 from Mitutoyo, Japan (CMEMS Laboratory of the Mechanical Engineering Department of University of Minho).

3.4.7 Reciprocating friction test

To study gold NP's and micro silver adhesion on zirconia surface, as well as, to determine both static and dynamic coefficient of friction (COF) a reciprocating pin-on-plate tribometer (Bruker-UMT-2, USA) was used. In order to better simulate the final desired application, young bovine bones were used as plate while the pin was the examined material surface. The bone plates were mounted in an acrylic electrochemical cell attached to the tribometer. Figure 41 illustrates the friction tests performed in context of this work.
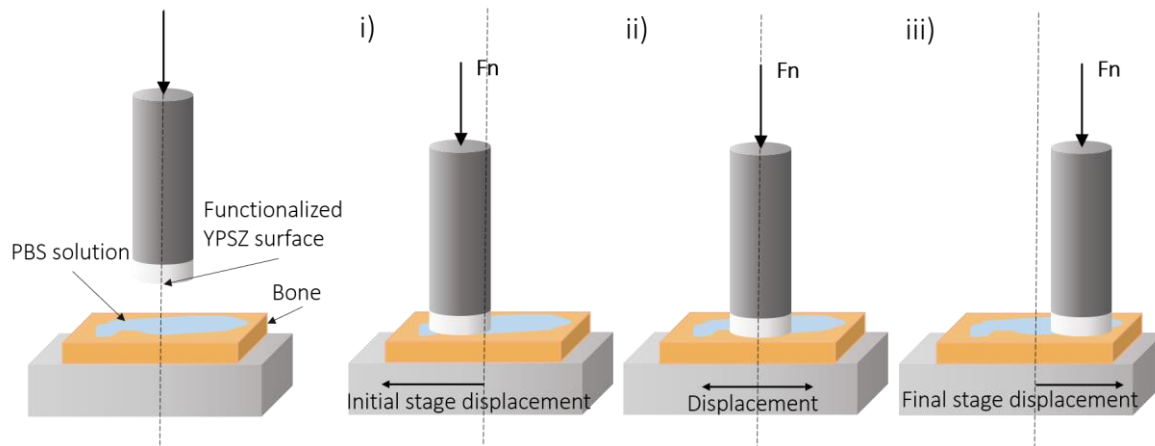
Figure 41 Schematic representation of the friction test: i) initial static friction test; ii) dynamic friction test; iii) final static friction test.

The friction tests consisted of three stages as follows: (i) determination of the initial static coefficient of friction by a single displacement in one direction (Figure 41i); (ii) measurement of the dynamic coefficient of friction during 17 seconds of reciprocating sliding (Figure 41ii); (iii) determination of the final static coefficient of friction by a single displacement in the opposite direction of the first reading (Figure 41iii). A normal load of 100 N was applied on the pin, at a frequency of 1 Hz and a stroke length of 5 mm of the plate, and continuously hydrating the bones with a Phosphate Buffered Saline (PBS) fluid. The PBS fluid is composed of NaCl (0.4 g/L), KCl (0.4 g/L), $CaCl_2$ $2H_2O$ (0.795 g/L), Na_2S $9H_2O$ (0.005 g/L), NaH_2PO_4 $2H_2O$ (0.69 g/L) and urea (1 g/L).

The experimental set up is visible in Figure 42. All the tests were carried out under the same conditions, the only variable was the surface treatment applied to zirconia samples. For each condition, three samples were tested, by using a new bone plate for each sample.

In this work, it was intended to evaluate the bone characteristics after the friction tests to conclude about the material transferred to the bone, although, this was not possible due to technical problems. This can be accomplished in further works.
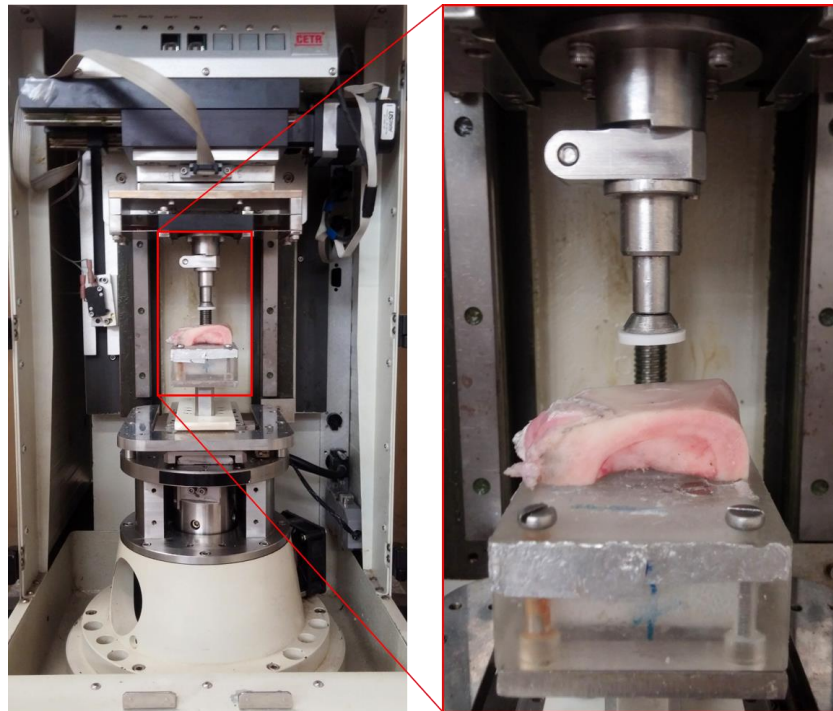
Figure 42 Tribometer Bruker-UMT-2, USA. (Tribology Laboratory of the Mechanical Engineering Department of University of Minho)

3.4.8   Mechanical interlock test

Considering the desired barrier effect against bacteria it is important that the soft tissue successfully retains in the surface of the implant, more precisely, within the designed microgrooves. Therefore, the influence of the groove width, depth and ridge width on the mechanical retention, in this case, of synthetic gum, will be tested. The synthetic gum used is a poly-vinyl siloxane (Gingifast, Zhermack, Italy) an elastomer typically used on mould impression in prosthodontics that better simulates natural gum tissue.

In the preparation of the samples for the mechanical test, the artificial gum was poured in a mould placed in the top of the texturized surface (Figure 43). Within 10 minutes, the samples were ready for the mechanical interlock test. Three samples were tested for each condition. A Schematic representation of the interlock which is expected to occur is presented in Figure 44
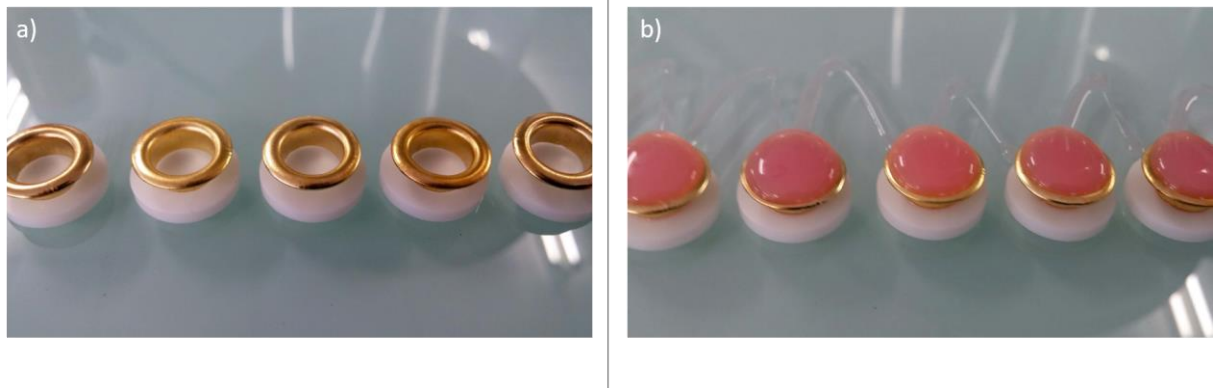
Figure 43 Schematization of the sample preparation for the mechanical test: a) metallic mould in top of the Y-PSZ texturized sample, b) synthetic gum poured in the metallic mould.
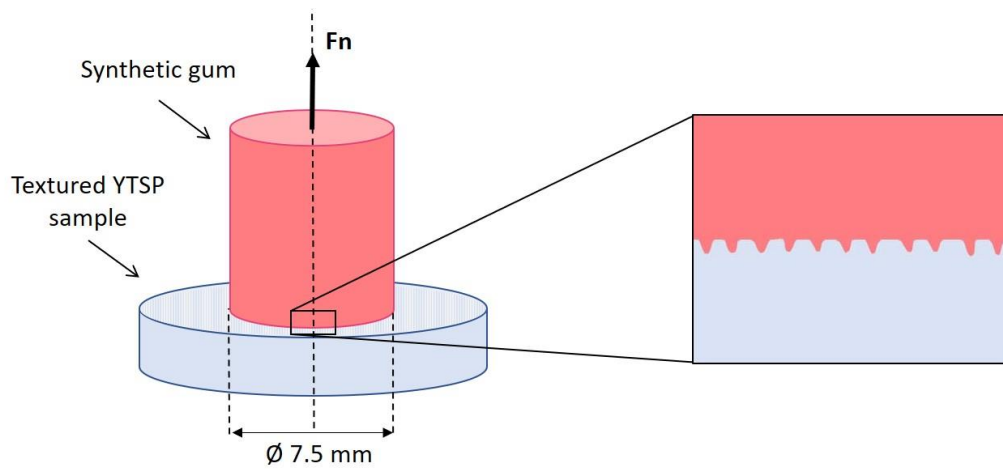
Figure 44 Schematic representation of the mechanical interlock test, with a zoom in on the contact surface between the synthetic gum and the textured Y-PSZ.

The uniaxial tensile stress tests were performed in a universal testing machine Hounsfiled, England (Figure 45), two metal clamps were adapted in order to ensure the stress was applied following the longitudinal axis of the sample. Tests proceeded at a constant crosshead speed of 0.25 mm/min at room temperature (≈25 °C).
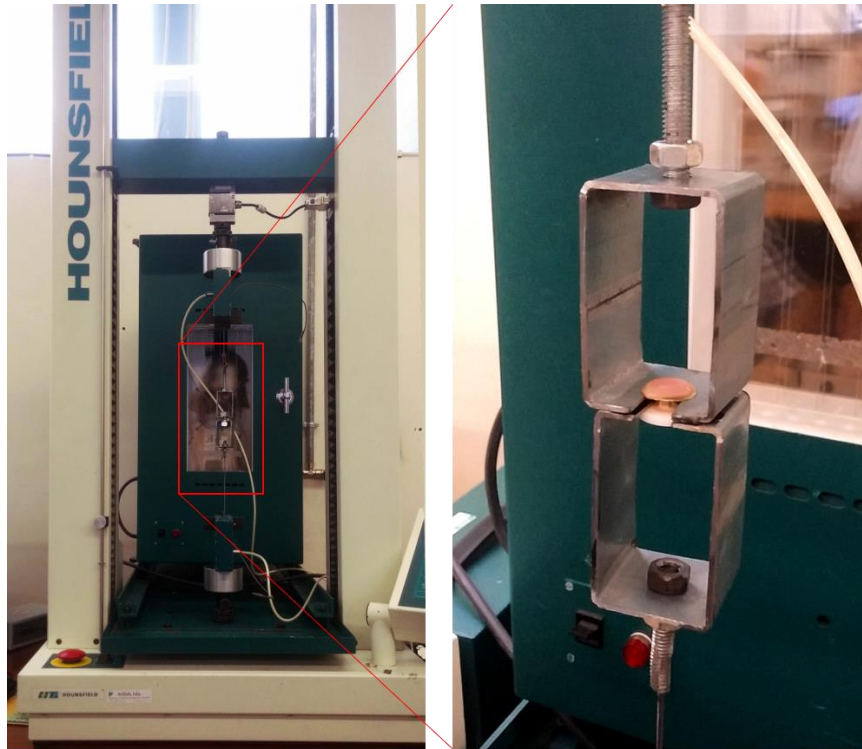
Figure 45 Tensile strength equipment, Hounsfiled, England (Laboratory of the Textile Engineering Department of University of Minho)

CHAPTER 4

RESULTS AND DISCUSSION

The results obtained in this dissertation will be presented in this chapter, throughout the four subchapters (4.1, 4.2, 4.3, 4.4) related with the two main objectives of this work. One of the main objectives is related to the production of a physical barrier to the passage of bacteria which was attained by the creation of microgrooves by laser. Regarding this purpose, a structural and mechanical analysis of the microgrooves, as well as an evaluation of the finishing effect of the laser is presented and discussed in the first subchapter (4.1). The second main objective, is the development of a surface with biocidal properties, which was attained by the multi-scale surface functionalization which comprises the remaining three subchapters (4.2, 4.3, 4.4). The second subchapter (4.2) presents the results of silver micro-functionalization, followed by morphological analysis, and reciprocating friction test. The third subchapter (4.3) presents the results of the gold nanoparticles solution morphological and chemical characterization. Finally, the Au NP's and Ag micro-zirconia surface functionalization was analysed in terms of morphological and reciprocating friction as a means of evaluating the adhesion of the particles to the substrate (4.4).

4.1 Textured Y-PSZ with microgrooves

This subchapter begins with the study regarding the effect of laser parameters in the microgroove's width, depth and interspacing produced on the Y-PSZ surface. After the selection of the most adequate microgroove profile, in terms of width and depth, considering reported literature values favourable to soft tissue cells attachment, interspacing adjustments were performed. Posteriorly, mechanical tests regarding the influence of groove width, depth and ridge width on the mechanical interlock to artificial soft tissue were also conducted. This subchapter ends with the evaluation of the surface roughness resultant from laser processing.

4.1.1   Surface analysis

SEM images represented in Figure 46 allowed to analyse each one of the 32 different laser ablated microgrooves (using the parameters from Table 7), and to determine the correspondent depth and width. Images of Figure 46a)-h) represents all combinations of number of scans with the scanning speed. Each image contains 4 conditions regarding the number of lines from point of 2D design construction, varying from 1 line (designated as L1) to 8 lines (designated as L8), namely L1, L2, L4 and L8). After microgrooves production, three measurements were taken from each dimension (width and depth) by means of *Image J* software. The obtained results are listed in Table 14.

From results different aspects can be appointed. The depth and width of the groove is strongly influenced by the scanning speed tested. Low material is removed when high scanning speed (values) are applied. Since the pulse frequency is constant, the higher the scanning velocity the lesser the number of pulses per line, diminishing the overlapping (energy concentration) and consequently the removal of material. This effect is more pronounced in the obtained depth but more discreet in the obtained width (Table 14). Regarding the effect of the number of scans on groove profile (Figure 46, downwards), it is evident an increase on the groove depth and a more discreet increase on correspondent width (Table 14).
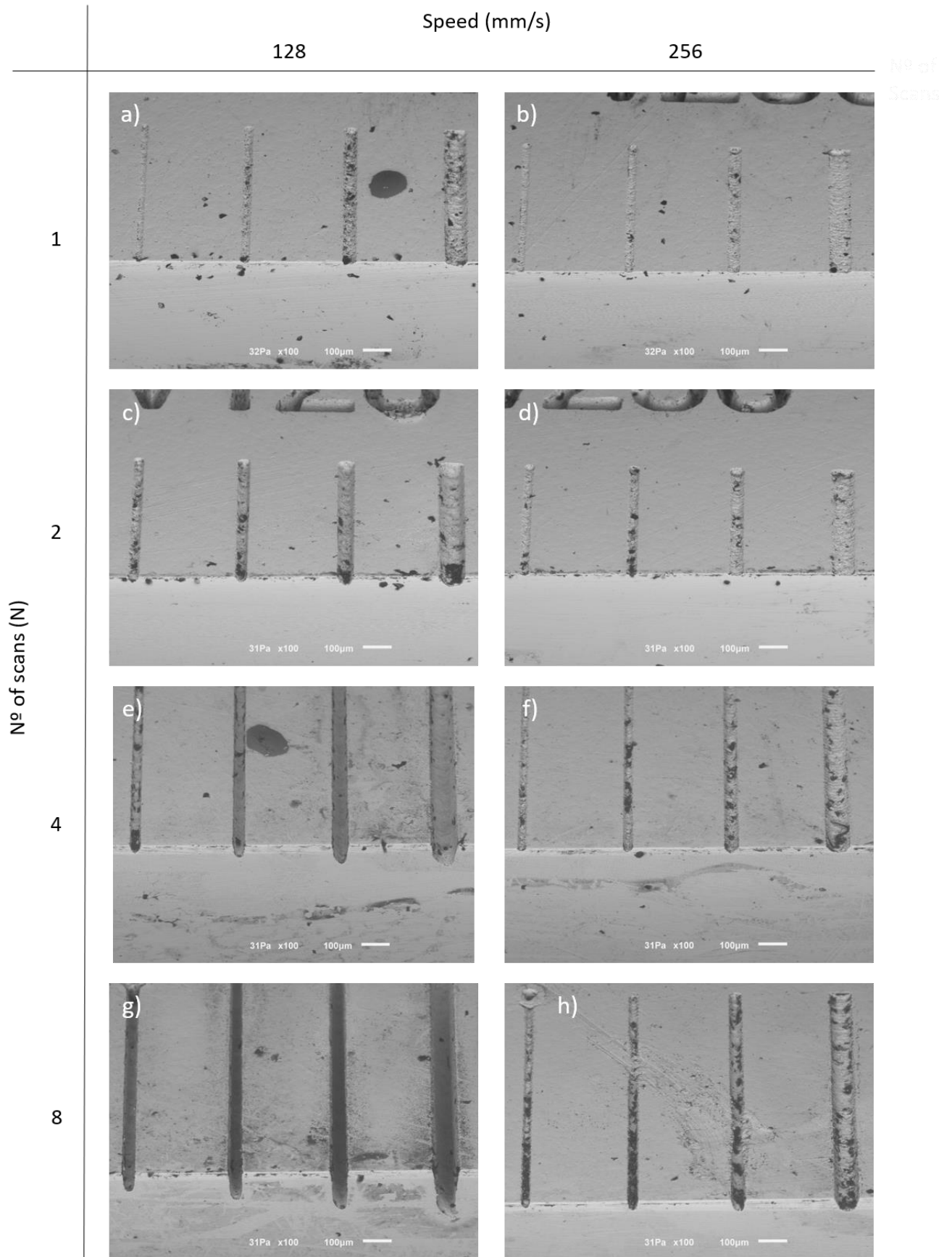
Figure 46 Tilted SEM images of the microgrooves produced via laser ablation: a) sample N1 S128 (L1,L2,L4,L8); b) sample N1 S256 (L1,L2,L4,L8); c) sample N2 S128 (L1,L2,L4,L8); d) sample N2 S256 (L1,L2,L4,L8); e) sample N4 S128 (L1,L2,L4,L8); f) sample N4 S256 (L1,L2,L4,L8); g) sample N8 S128 (L1,L2,L4,L8); h) sample N8 S128 (L1,L2,L4,L8).

Table 14 Average values (mean ± SD) of width and depth of the designed microgrooves. Estimated from Image J treatment of SEM images.

Sample	Average width ± SD (µm)	Average depth ± SD (µm)
N1 S128 L1	22.7 ± 1.3	8.9 ± 0.4
N1 S128 L2	29.8 ± 1.4	10.9 ± 0.4
N1 S128 L4	46.3 ± 0.9	13.9 ± 0.8
N1 S128 L8	76.3 ± 0.6	27.5 ± 0.7
N1 S256 L1	21.8 ± 2.0	4.5 ± 0.1
N1 S256 L2	28.4 ± 1.3	5.7 ± 0.4
N1 S256 L4	40.9 ± 1.5	6.7 ± 0.4
N1 S256 L8	76.1 ± 0.8	10.4 ± 0.9
N2 S128 L1	36.9 ± 0.7	13.1 ± 0.8
N2 S128 L2	42.5 ± 0.9	25.0 ± 0.5
N2 S128 L4	57.5± 1.0	42.4 ± 1.3
N2 S128 L8	88.3 ± 1.3	43.7 ± 1.1
N2 S256 L1	31.9 ± 1.1	8.2 ± 0.2
N2 S256 L2	35.8 ± 1.4	16.5 ± 0.9
N2 S256 L4	46.9 ± 0.8	12.2 ± 0.7
N2 S256 L8	77.3 ± 1.1	14.1 ± 0.1
N4 S128 L1	36.4 ± 2.0	39.2 ± 0.3
N4 S128 L2	43.3 ± 1.7	65.1 ± 0.5
N4 S128 L4	56.9 ± 3.5	99.0 ± 0.9
N4 S128 L8	100.0 ± 1.7	111.3 ± 0.6
N4 S256 L1	30.2 ± 0.4	12.7 ± 0.1
N4 S256 L2	33.1 ± 0.8	22.0 ± 0.8
N4 S256 L4	48.5 ± 1.0	30.5 ± 0.2
N4 S256 L8	84.9 ± 0.2	34.4 ± 0.7
N8 S128 L1	47.6 ± 1.0	91.4 ± 0.1
N8 S128 L2	47.5 ± 1.7	137.1 ± 1.2
N8 S128 L4	56.8 ± 3.1	190.5 ± 0.7
N8 S128 L8	98.8 ± 1.0	238.8 ± 1.4
N8 S256L1	28.8 ± 1.3	28.9 ± 0.2
N8 S256 L2	36.1 ± 0.1	46.7 ± 0.8
N8 S256 L4	48.8 ± 1.2	57.6 ± 0.8
N8 S256 L8	85.5 ± 1.3	63.6 ± 1.5

Regarding SEM images, it is possible to verify that the number of lines have a strong effect on the width, since the 2D drawing software controls the geometric plane coincident of the working table, and an increase in the number of lines added to the drawing widens the patch. Similarly, a great increase on depth of groove was achieved with the increase of number of lines which can be related with the overlapping between lines of pulses, as mentioned in section *2.7.1 Laser ablation in chapter 2*.

From all the obtained results, the most adequate profile dimensions considering the physical barrier correspond to condition N1 S256 L1 (1 scan, 256 mm/s scan speed and 1 line). However, to complete physical barrier, another study focused on groove interspace was

conducted. To ease the readers interpretation a general representation of a drawing is presented on Figure 47.
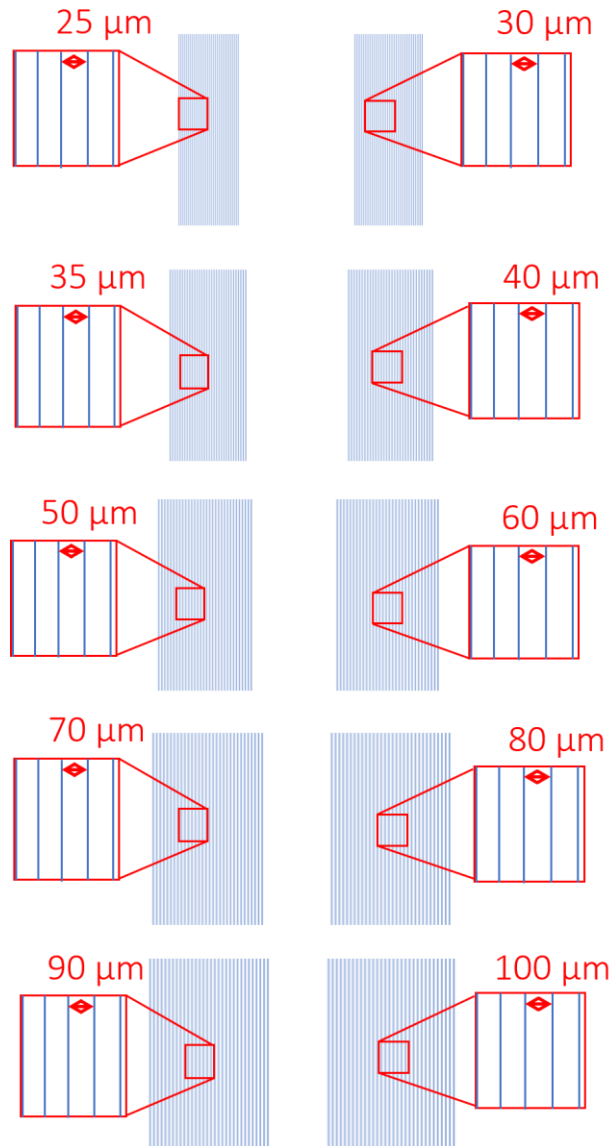
Figure 47 General representation of the drawing reproduced in software Inkskape to use in groove interspace study.

Figure 48 present the SEM images of the microgrooves produced with 2D software corresponding to S25, S30, S35, S40, S50, S60, S70, S80, S90 and S100.
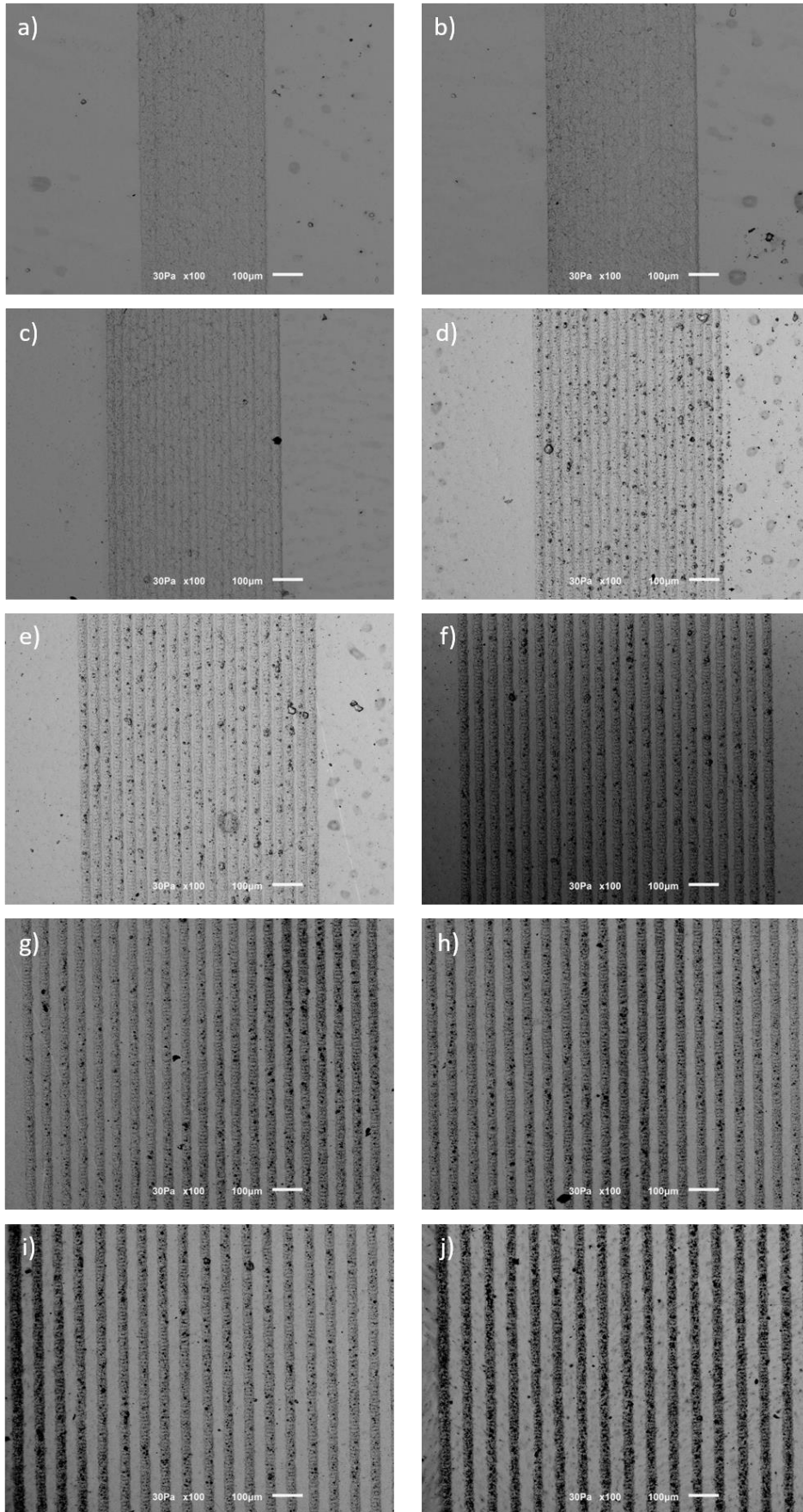
Figure 48 Top SEM images of Y-PSZ micromachined surface with 2D drawing line spacing parameter from sample: a) S25; b) S30; c) S35; d) S40; e) S50; f) S60; g) S70; h) S80; i) S90; j) S100.

The successive grooves are well aligned and were successfully replicated. It is also noticeable that ridge width increases with groove interspacing. As it was expected since groove width remained constant (Table 15). The groove interspacing obtained is not in agreement with the inputted software parameters, which is explained by the retraction of the Y-PSZ sample (20 %), since micro-machining is carried out before the sintering step.

Table 15 Table with line spacing and ridge width average values (mean ± SD) of micro machined Y-PSZ obtained by software Image J.

2D drawing	Grooves interspacing ± SD (µm)	Ridge width ± SD (µm)
S25	-	
S30	-	
S35	-	
S40	28.8 ± 2.1	≈ 0
S50	38.3 ± 1.0	8.5 ± 0.2
S60	49.7 ± 1.7	21.4 ± 1.5
S70	57 ± 1.5	22.7 ± 1.1
S80	62.4 ± 1.0	28.1 ± 0.8
S90	72.7 ± 1.7	35.8 ± 2.4
S100	75 ± 1.5	40.7 ± 0.8

The SEM images from Figure 48 allowed to verify that, using the most adequate laser conditions, and a line spacing inferior to 40 µm (S40) the groove walls overlap and cease to exist. Therefore, successive grooves closer than approximately 28.8 µm are not attainable by this specific technology.

A set of processing parameters was selected to test the influence of the groove dimensions (width and depth) on the mechanical resistance. A group of grooves with approximately the same width (50 µm) and a group of grooves with approximately the same depth (40 µm) were selected from the previous study (Figure 46 and Table 14). Table 16 present the selected groove dimensions and the corresponding identification, where the varying dimension are in bold.

Table 16 Groove depth and width values to include on the mechanical study. Varying dimensions in bold.

Average width ± SD (µm)	Average depth ± SD (µm)	Sample
36.4 ± 2.0	39.2 ± 0.3	N4 S128 L1
57.5± 1.0	42.4 ± 1.3	N2 S128 L4
88.3 ± 1.3	43.7 ± 1.1	N2 S128 L8
46.9 ± 0.8	**12.2 ± 0.7**	N2 S256 L4
48.8 ± 1.2	**57.6 ± 0.8**	N8 S256 L4
47.5 ± 1.7	**137.1 ± 1.2**	N8 S128 L2

To study a dimensional parameter influence on a specific property, the remaining must be kept constant. Therefore, in width and depth study, the ridge width also needed to be constant. Considering this, a ridge width (groove wall) of 21.4 µm (corresponding to a 60 µm on Inkscape) was selected from Table 15. Since groove interspacing was only studied, until then, for the favourable profile condition (N1S256L1) and considering that the ridge width must be kept constant in all the conditions, the groove interspacing was adjusted for each condition, using the relation: Groove interspacing = Average width + Ridge width (Figure 23 illustrates this relationship). Finally, and considering the material retraction (20 %), an increment was performed on groove interspacing values of the 2D drawing software. All the adjustments are shown on Table 17.

Table 17 Information about the adjustments done to reach a groove interspacing which corresponds to a constant ridge width, to use as an input on the 2D drawing software.

Groove width ± SD (µm)	Ridge width ± SD (µm)	Groove interspacing (µm)	Groove interspacing 2D drawing (µm)
36.4 ± 2.0		57.9 ± 2.5	72.3
57.5± 1.0		79.0 ± 1.8	98.7
88.3 ± 1.3	21.4 ± 1.5	109.7 ± 2.0	137.2
46.9 ± 0.8		68.4 ± 1.7	85.5
48.8 ± 1.2		70.3 ± 1.9	87.9
47.5 ± 1.7		69.0 ± 2.2	86.2

A study on the influence of the ridge width on groove mechanical resistance was also necessary, therefore, condition N8S256L4 (48.8 ± 1.2 µm width and 57.6 ± 0.8 µm depth) was selected for its width and depth proximity. The ridge width dimensions to study are included on the previous groove interspace study (Figure 48 and Table 15). On a similar way to the previous adjustments, the groove interspacing to use as an input on 2D drawing software was determined by the sum of ridge and groove width, finalizing with the adjustment for the

expected 20 % retraction. Table 18 presents relevant information on the dimensional adjustment.

Table 18 Information about the adjustments done to reach a line spacing which corresponds to the desired ridge width, to use as an input on the 2D drawing software.

Sample	Ridge width ± SD (µm)	Groove width ± SD (µm)	Groove interspacing (µm)	Groove interspacing 2D drawing (µm)
	8.5 ± 0.2		57.3 ± 1.2	71.6
N8S256L4	21.4 ± 1.5	48.8 ± 1.2	70.3 ± 1.9	87.8
	35.4 ± 2.4		84.7 ± 2.7	105.8

Table 19 displays all the pertinent information about the selected groove width, groove depth, ridge width and groove interspacing for the present study, as well as, 2D drawing adjustments that were necessary.

Table 19 Information on groove width, groove depth, ridge width and groove interspacing to include on the mechanical tests, as well as the adjustments on groove interspacing to use as input on the 2D software.

Study	Groove width ± SD (µm)	Groove depth ± SD (µm)	Ridge width ± SD (µm)	Groove interspacing (µm)	Groove interspacing 2D drawing (µm)
	36.4 ± 2.0	39.2 ± 0.3		57.9 ± 2.5	72.3
Groove width	**57.5± 1.0**	42.4 ± 1.3		79.0 ± 1.8	98.7
	88.3 ± 1.3	43.7 ± 1.1	21.4 ± 1.5	109.7 ± 2.0	137.2
	46.9 ± 0.8	**12.2 ± 0.7**		68.4 ± 1.7	85.5
Groove depth	48.8 ± 1.2	**57.6 ± 0.8**		70.3 ± 1.9	87.9
	47.5 ± 1.7	**137.1 ± 1.2**		69.0 ± 2.2	86.2
			8.5 ± 0.2	57.3 ± 1.2	71.6
Ridge width	48.8 ± 1.2	57.6 ± 0.8	**21.4 ± 1.5**	70.3 ± 1.9	87.9
			35.4 ± 2.4	84.7 ± 2.7	105.8

The inkscape drawings used on groove width (w1-36.4 µm, w2-57.5 µm, w3-88.3 µm), depth (d1-12.2 µm, d2-57.6 µm, d3-137.1 µm) and ridge width (r1-8.5 µm, r2-21.4 µm, r3-35.4 µm) study are presented in Figure 49.
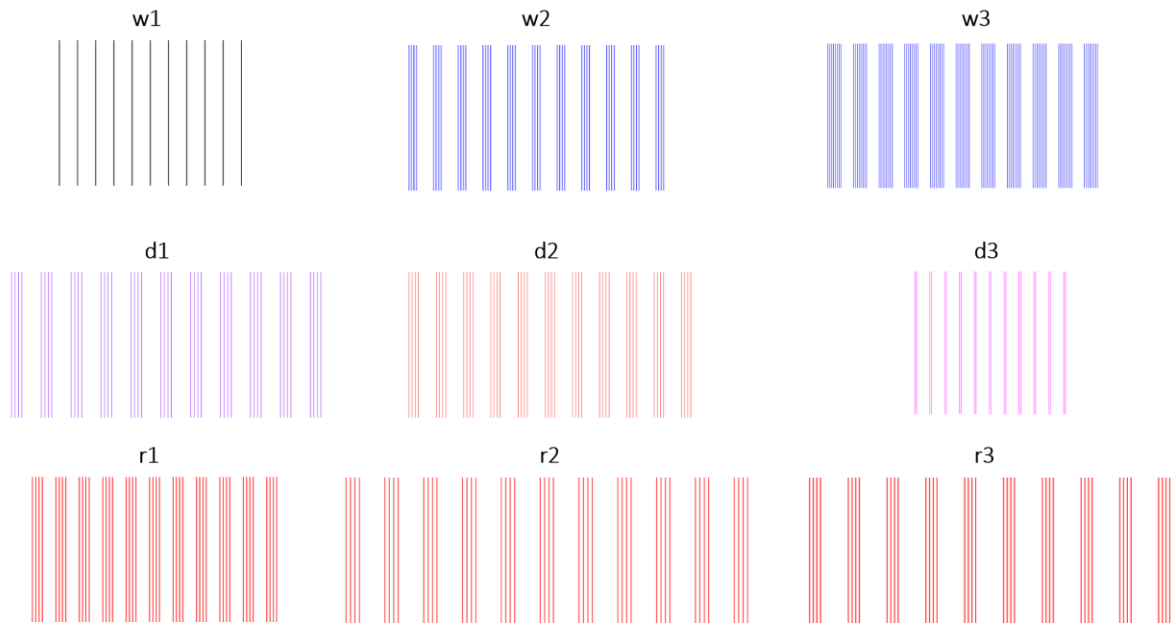
Figure 49 Drawings reproduced in software Inkscape to use in groove profile dimensions study: width study: w1-36.4 μm, w2-57.5 μm, w3-88.3 μm; depth study: d1-12.2 μm, d2-57.6 μm, d3-137.1 μm; Ridge study: r1-8.5 μm, r2-21.4 μm, r3-35.4 μm.

The resulting SEM images from this first study are shown on Figure 50. Both width and depth vary as it was expected. Although, ridge width does not correspond to the expected because its value should have remained constant (21.4 μm) on the width and depth study (Figure 50a,b,c and Figure 50d,e,f). Consequently, the ridge corresponding to 8.5 μm (on groove interspacing study) was destroyed (Figure 50g). For a better analysis of the dimensions obtained, Table 20 presents the expected and the obtained groove and ridge width values. A readjustment of the groove interspacing was made in the 2D drawing software based on the difference between these values. The readjusted groove interspacing and correspondent values to use as input are included in the same table (Table 20). These are the final adjustments and therefore the final software parameters inputted in Inkscape.

Figure 51 presents the SEM images from the grooves after the necessary dimensional adjustments, namely, the groove interspacing (ridge wall) adjustments. The ridge width is constant for the groove width and depth study. The sample which presented the walls fragmented (smaller ridge width), presents now distinguishable ridge walls (Figure 51g).
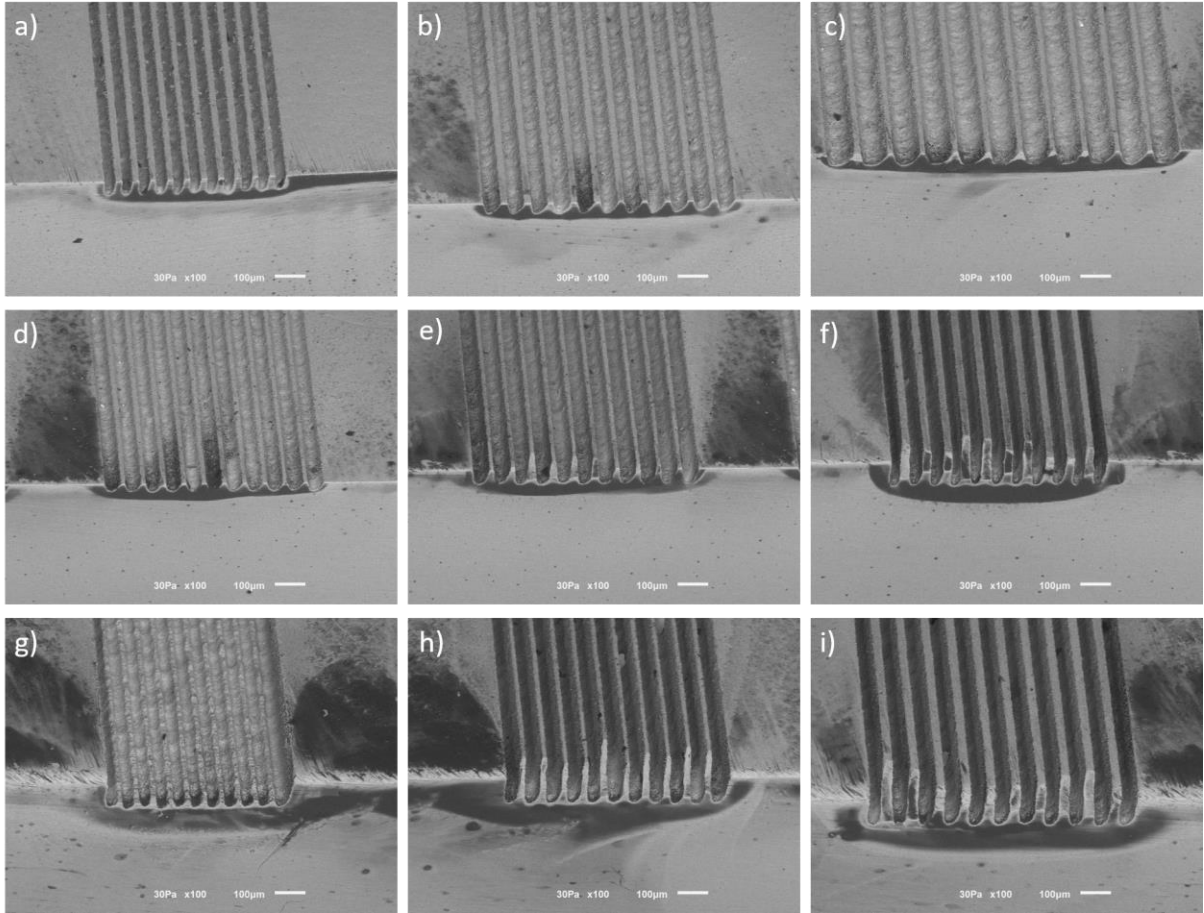
Figure 50 Series of successive identical grooves for groove width study: a) 36.4 μm ,b) 57.5 μm, c) 88.3 μm; for groove depth study: d) 12.2 μm, e) 57.6 μm, f) 137.1 μm; and for ridge width study: g) 8.5 μm, h) 21.4 μm, i) 35.4 μm.

Table 20 Information on expected and obtained groove and ridge width values, and groove spacing new values inputted on the 2D drawing software.

Study	Expected groove width ± SD (μm)	Obtained groove width ± SD (μm)	Expected ridge width ± SD (μm)	Obtained ridge width ± SD (μm)	Groove interspacing ± SD (μm)	Groove interspacing 2D drawing (μm)
Groove width	36.4 ± 2.0	**36.3 ± 1.0**		**20.6 ± 0.5**	–	–
	57.5± 1.0	**56.1 ± 1.3**		**20.0 ± 0.1**	–	–
	88.3 ± 1.3	**89.4 ± 0.8**	21.4 ± 1.5	**17.1 ± 0.1**	115.1 ± 1.7	143.9
Groove depth	46.9 ± 0.8	51.7 ± 0.5		**14.0 ± 0.3**	81.6 ± 1.6	102.1
	48.8 ± 1.2	52.5 ± 1.5		**13.0 ± 0.3**	82.3 ± 2.1	102.9
	47.5 ± 1.7	41.5 ± 0.3		**21.9 ± 0.0**	–	–
Ridge width		–	8.5 ± 0.2	–	63.0 ± 1.4	78.7
	48.8 ± 1.2	53.7 ± 0.5	21.4 ± 1.5	**12.4 ± 0.6**	81.6 ± 1.6	102.0
		51.9 ± 1.3	35.4 ± 2.4	**26.1 ± 1.0**	97.4 ± 2.7	121.7
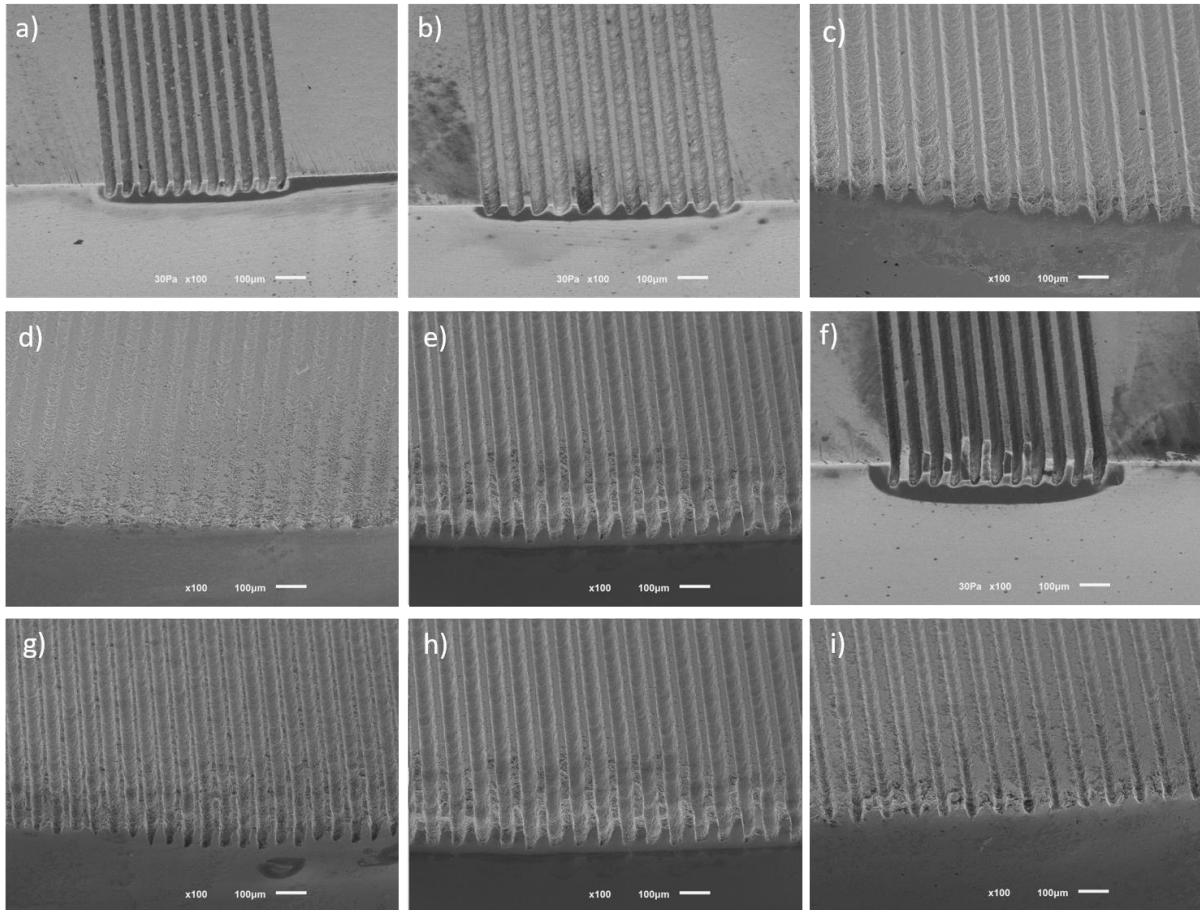
Figure 51 SEM images from the microgrooves after the final adjustments to line interspacing (ridge width).

4.1.2   Mechanical interlocking analysis

Mechanical interlocking test was performed to evaluate the retention capacity of the microgrooves produced to artificial gum and predict the implant barrier performance during service.

Table 21 displays the groove dimesional parameters that are about to be studied, as well as, the nomenclature adopted to ease the following result discussion. Group 'W' corresponds to the groove width study, 'D' to the groove depth study, 'R' to the groove ridge study and sample 1,2 and 3 to the different dimensions to be studied, additionally, a sample C corresponding to the literature optimal condition for tissue cell development and lastly, a control which represents the Y-PSZ sample with no grooves.

Table 21 Parameters to introduce in the study of groove dimensions on the mechanical interlocking test. Group W-groove width study, group D-groove depth study, group R-ridge width study, each comprising sample 1, 2 and 3. Also sample C which corresponds to the parameters appropriate for soft tissue cell spreading and the control Y-PSZ sample.

Group	Sample	Groove width ± SD (μm)	Groove depth ± SD (μm)	Ridge width ± SD (μm)
	1	36.4 ± 2.0		
W	2	57.5± 1.0		
	3	88.3 ± 1.3		
	1		12.2 ± 0.7	
D	2		57.6 ± 0.8	
	3		137.1 ± 1.2	
	1			11.1 ± 1.6
R	2			21.9 ± 0.7
	3			41.1 ± 1.5
	C	21.8 ± 2.0	4.5 ± 0.1	7.0 ± 2.9
	Control	0	0	0

Table 22 present the critical failure load from the tensile strength tests to all the 33 samples, including three samples per condition tested (test 1, test 2 and test 3). Some of the tests failed too early, and no value was recorded before failure, suposelly due to the limit detection of the equipment. Those cases are shown on the table with a "–" and were considered as 0 for means of average values calculation, for instance, none the control samples registered any values, as so, the critical failure load considered was 0 N. Graphic from Figure 52 show the average critical failure load for the three conditions of each group, in a comparative point of view. In a general perspective, there is an increase on the critical failure point with the increase of groove width and depth which is not so evident in the case of the ridge width.

Table 22 Critical failure load resulting from mechanical interlock test to the produced textured Y-PSZ samples.

Group	Sample	Critical failure load (N) Test 1	Critical failure load (N) Test 2	Critical failure load (N) Test 3
	1	5.750	–	–
W	2	9.575	6.925	–
	3	17.250	14.825	15.500
	1	5.425	–	–
D	2	12.250	14.000	6.325
	3	18.075	19.500	12.000
	1	11.500	8.180	8.430
R	2	12. 580	14.000	6.325
	3	12.675	9.250	14.750
	C	4.325	3.250	–
	Control	–	–	–
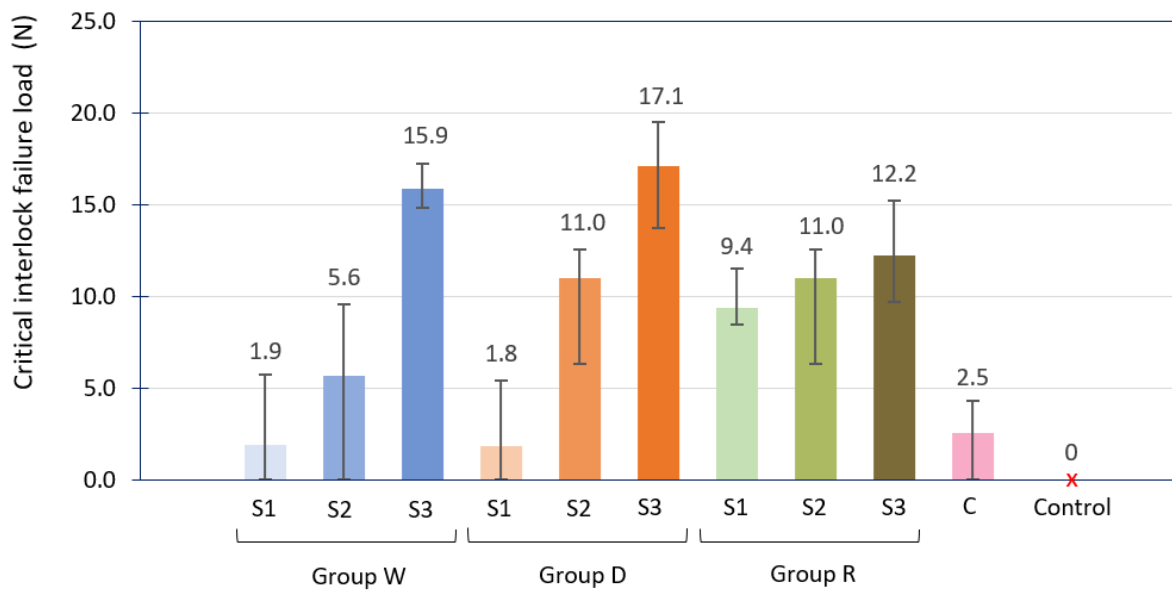
Figure 52 Critical interlock failure load between Y-PSZ microgrooves and the synthetic gum tissue according to groove dimensions.

In general, all the microgrooves present better results to the critical interlock failure when compared to the control sample. There seems to be a dependence Considering width parameter, it can be seen from Figure 52 that there is a significant difference (approximately 52 μm) between extreme conditions (S1 and S3) which means that great groove width lead to higher critical interlock failure load i.e. higher mechanical retention. This is visible also in depth parameter, a difference (aproximately 125 μm) between extreme conditions (S1 and S3) lead to higher critical interlock failure load.

The groove presenting a better interlock was sample 3 from the group D, followed by sample 3 from group W. In group R, even though the ridge wall variation is slight, the critical failure increase with ridge width. In the case of the groove dimensions described in literature as suitable for cell adhesion (sample C), it presented one of the lowest values of critical interlock failure load. This might be probably because it reunites the lowest depth and width value. This may be explained by the fact that a lower contact area between the sample and gum tissue decreases the amount of attachment points between surfaces. This was the reason why this study expanded its dimensions to higher width, depth and ridge values, even though these were not yet studied for its soft tissue cell attachment ability.

4.1.3   Roughness evaluation

The roughness caused by the laser passage on the Y-PSZ surface is an important factor considering the application. To study this parameter a sample from the previous 2D drawing line spacing study was used. The sample chosen was S25 for the absence of groove walls which would compromise the roughness Ra results. Thus, Figure 53 and Figure 54 show representative 2D roughness profiles from the unprocessed and laser processed region of surface, respectively, while Table 23 gathers the arithmetic average roughness (Ra) and the average maximum peak to valley (Rz) and standard deviations.
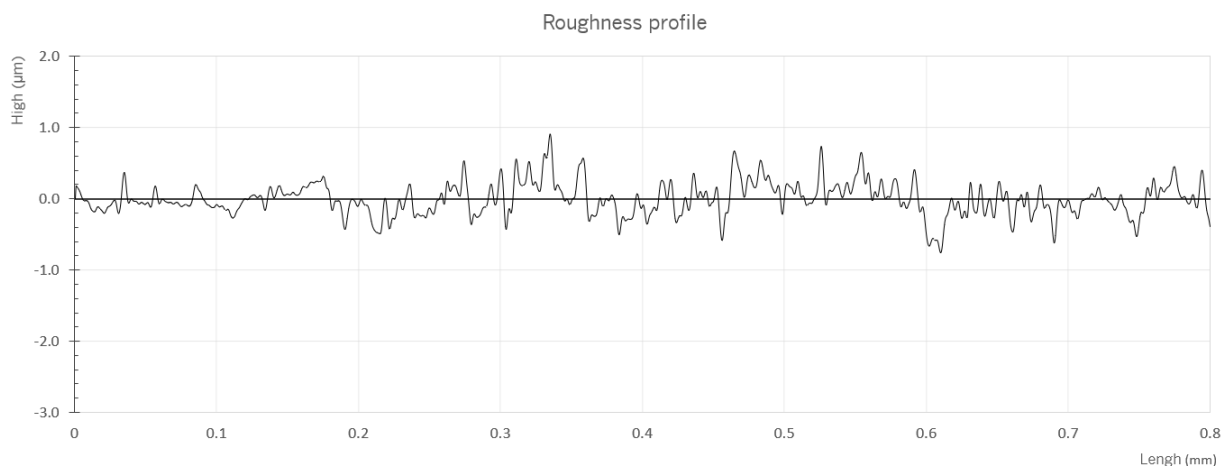
Figure 53 Representative 2D roughness profiles from the unprocessed region of the sample.
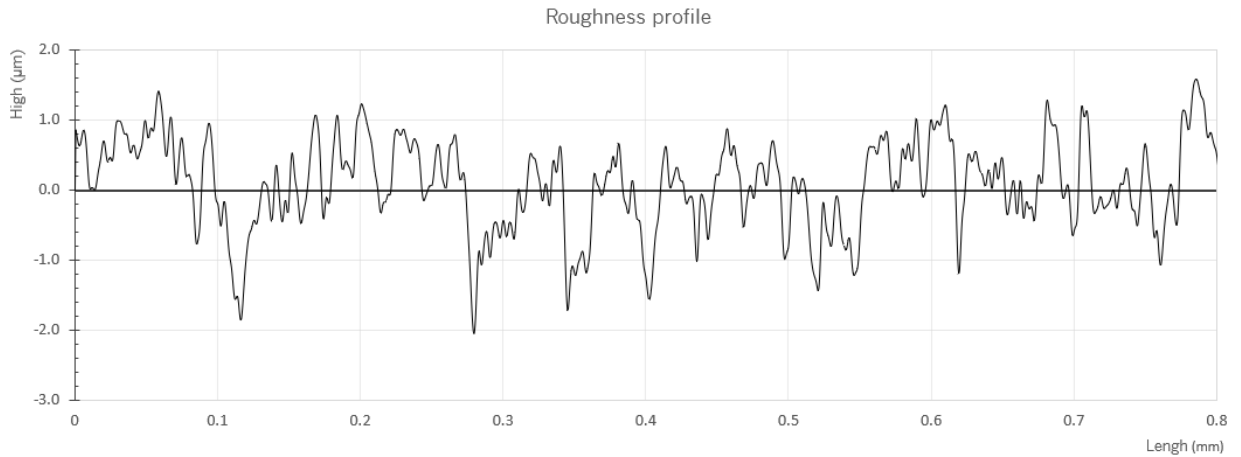
Figure 54 Representative 2D roughness profiles from the processed region of the sample.

Table 23 Surface roughness of laser processed and unprocessed region of the sample. The arithmetical mean roughness (Ra) and average maximum peak to valley values (Rz) with the correspondent standard deviation.

Region	Average Ra ± SD (µm)	Average Rz ± SD (µm)
Laser processed	0.584 ± 0.027	5.947 ± 0.449
Unprocessed	0.196 ± 0.050	2.903 ± 0.455

The roughness values corresponding to the laser passage is ≈ 0.6 µm, the Ra from the unprocessed region of the sample is ≈ 0.2 µm (Figure 55). The literature studies point 0.2 µm as the ideal Ra value to inhibit bacterial adhesion (see topic *Bacterial antifouling 2.3.3*). The roughness resultant from laser processing may not avoid bacterial adhesion, however, studies about epithelial cell attachment to the microgrooves need to be performed to conclude about the potential of this level of roughness.
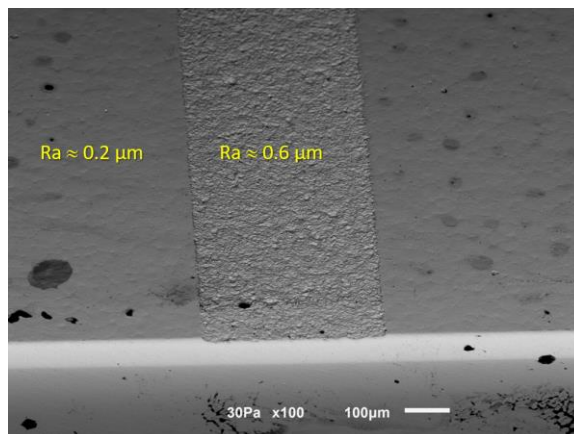
Figure 55 SEM image from the two different regions of a sample, before laser and after laser passage and correspondent roughness.

4.2 Silver surface micro-functionalization

This section presents the results of the practical work based on silver Y TSP surface micro-functionalization. Two different textures (with different roughness level) were produced to evaluate the most adequate texture to retain silver powder during and after sintering. Regarding the sintering process of micro Ag powder onto the textured zirconia surface, different laser parameters were tested. Morphologic evaluation was performed by SEM to characterize the created patterns, as well as, to do cross sectional analysis of the Y-TSP – Ag interface. Finally, the adhesion of the micro Ag on the Y-PSZ surface was evaluated by reciprocating friction tests and analyzed by SEM/EDS.

4.2.1 Micro-textures for Ag deposition

Two different textures with different roughness level, designated as coarse and fine patterns, were tested to adhere micro Ag on zirconia surface. The morphology of these textures is presented in Figure 56, a and b, corresponding to coarse and fine patterns, respectively.
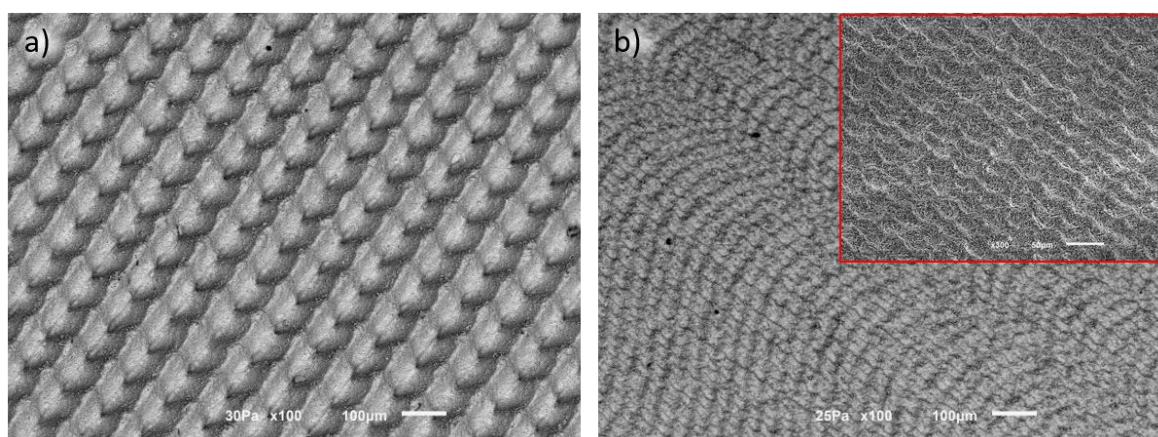
Figure 56 SEM images from a tilted view of a) the coarser texture at 100 X magnification and b) the finer texture produced at 100 X magnification with a close up to 300X magnification (scale bar= 50 µm).

After the textures production, next step consisted on silver powder sintering and polishing (to remove external oxide layer). Finally, its adhesion was tested by ultrasonic cavitation. In the present functionalization method, the polishing step acted as an exclusion process for most of the laser conditions, since the silver added disintegrated with the friction associated to polishing, indicating a bad sintering of the silver powder. In the case of the fine pattern, the samples that resisted to the polishing step, from all the samples, were P6S128N1

(Power: 6 W, laser speed: 128 mm/s, number of laser scans: 1), P6S64N1, P3S64N1, and P1.5S64N4. On the other hand, only two conditions on the coarser pattern resisted to the polishing step, sample P6S128N1 and sample P3S128N1.

The ultrasonic adhesion test allowed to evaluate the silver effective adhesion to the substrate. It was observed that in the case of the sample with silver deposited over the fine pattern, air confined between the silver and the substrate was easily observed, confirming a poor adhesion between both materials. This observation led to the exclusion of the samples with the fine pattern, therefore, only samples P6S128N1 and P3S128N1 deposited over the coarse pattern proceeded to the characterization.

4.2.2   Silver deposition and sintering

The top view and cross-sectional SEM images from P3S128N1 and P6S128N1 are shown, respectively on Figure 57 an Figure 58.

In general, the cross-sectional images (c) and d)) show that silver powder was successfully impregnated in the Y-PSZ cavities without compromising the substrate. No cracks are visible, indicating that the Ag sintering process seems not to affect Y-PSZ mechanical integrity. Some black points are visible which can be related to SiC resultant from the polishing process.

Regarding the sintering process of the silver powder some observations can be made. Top view images of the sample show the existence of micro porosity, localized specially at the silver region of the surface. Despite this, the interface does not show porosity indicating a good adhesion between silver and Y-PSZ. The porosity observed may be indicative of inefficient powder pressing. The cross-sectional analysis reveals that silver is well densified. However, loose powder at the bottom of the grooves indicates a poor sintering in the lower regions of the textures. The laser power used seems to be related to the depth of sintering. When a lower laser power was applied (3 W), approximately 36 μm downward sintered silver is observed (Figure 57c). While for a higher laser power (6 W), approximately 58 μm downward seems to be sintered (Figure 58c). Suggesting that a great laser power lead to a better sintering process.
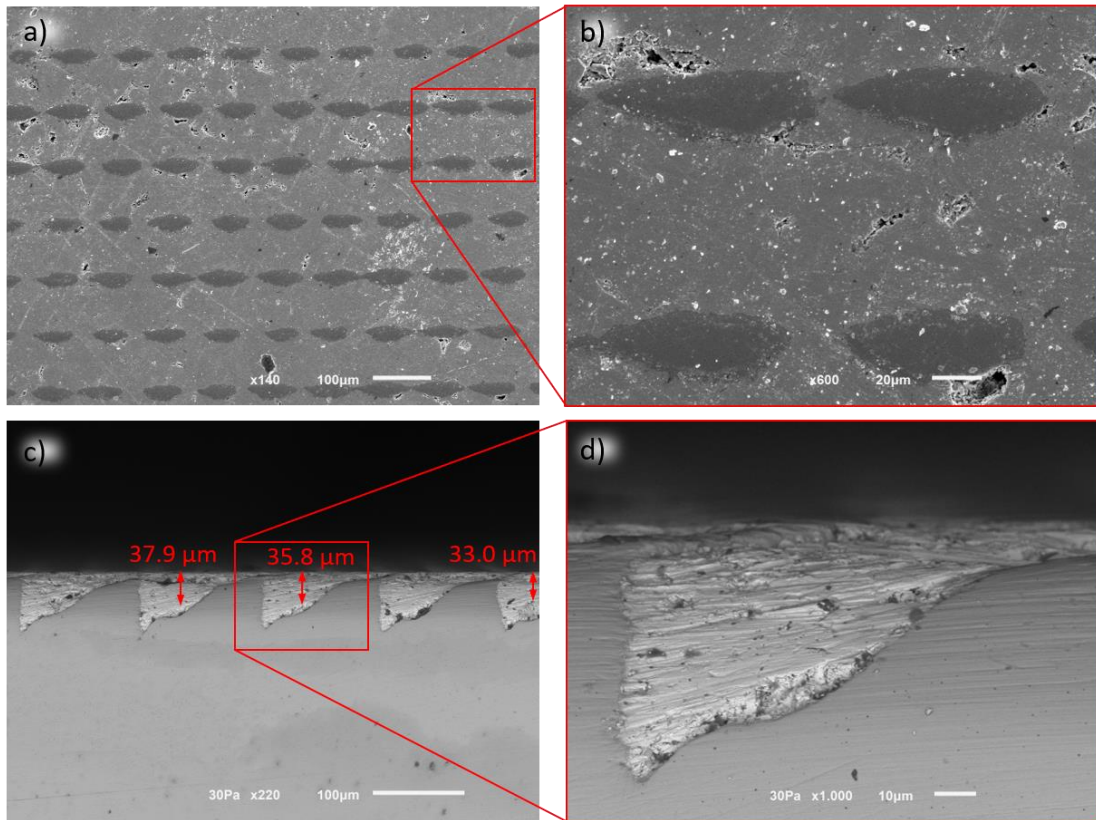
Figure 57 Top and cross sectional SEM images from sample P3S128N1: a) and b) top view with 140 X and 600 X magnification, respectively, c) and d) the cross sectional view with 220 X and 1000 X magnification, respectively.
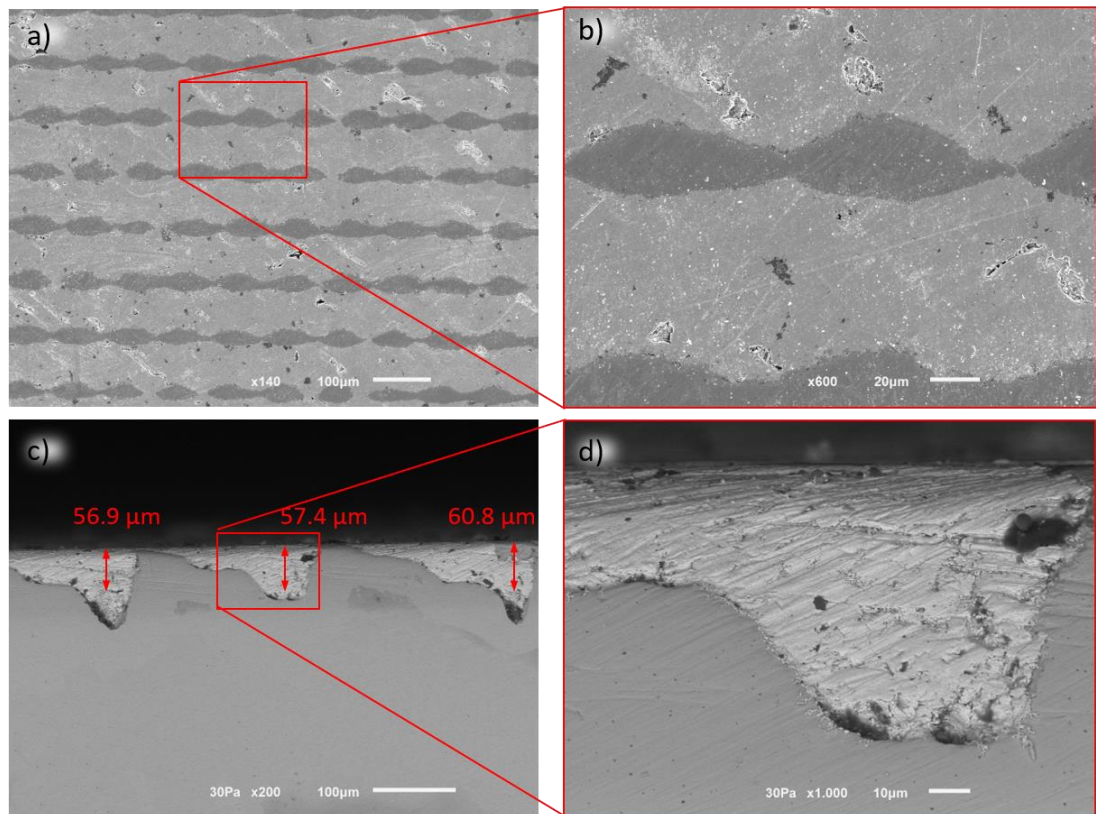
Figure 58 Top and cross sectional SEM images from sample P6S128N1: a) and b) top view with 140 X and 600 X magnification, respectively, c) and d) the cross sectional view with 220 X and 1000 X magnification, respectively.

4.2.3 Reciprocating friction test

As mentioned in chapter 3, friction tests were employed to study the friction performance and the adhesion of the micro sized Ag to the Y-PSZ surface. In order to simulate the dental implant insertion in body environment, the experiments were performed against bone in lubricated conditions. The obtained results from the experiments are presented in Figure 59.
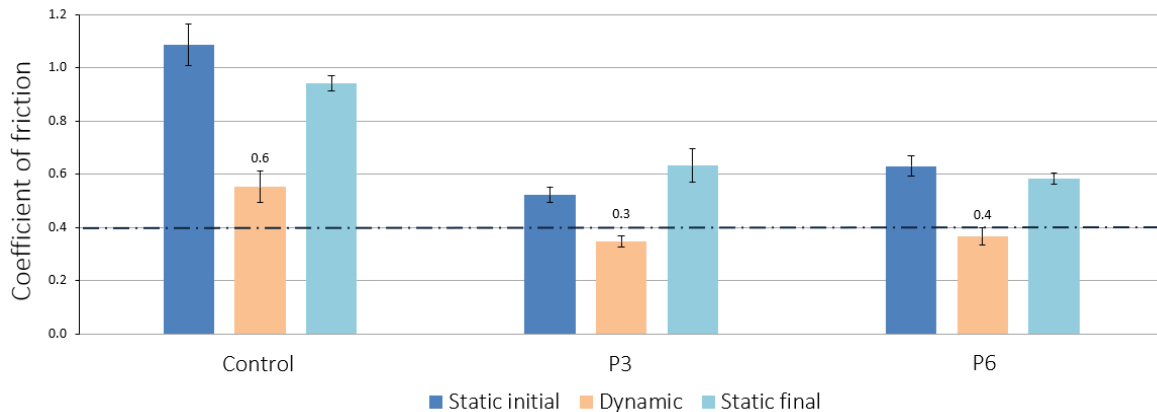
Figure 59 Average static initial, dynamic and static final coefficient of friction (COF) from conditions P3 and P6 and from the control sample.

The results from the friction tests comprises the average static initial, dynamic and static final coefficient of friction (COF) from conditions P3 and P6 and the control sample, for comparison purposes.

In general, all the samples have an average dynamic COF lower than the correspondent static initial and final stage values. This was expected, since the force required to begin the movement is always greater than the one needed to maintain it.

The control sample presents a higher dynamic COF (0.6) than the other samples (0.3 and 0.4), explained by the texturized characteristic of its surface, which was design specifically for Ag deposition. Also, its static initial COF is higher than the static final COF, which may be explained by the allocation of bone in between the pillars during the dynamic friction stage. This allocation might have proportionated a plain layer and therefore diminished the resistance of the material to the plate/bone on the static final measurement. This effect is not so evident in the functionalized samples, because, in this case, the textures were filled with Ag material which provided a levelled surface.

If the initial and the dynamic stages of friction represent the moment of insertion of the implant, the final static friction stage may represent the force necessary to displace it.

Thus, the final stage COF may give indication about the adhesion of the bone to the implant, after implantation, as well as, about primary stability of the implant. Since no significant decrease was observed between the initial and final static COF in conditions P3 and P6, the friction seemed not to affect the COF of the samples, neither the primary stability potential of the material. This might suggest the application of this material at lower regions of the implant.

After the friction test, the same samples were subjected to morphological and chemical analysis. SEM images from the control sample (textured Y-PSZ before Ag addition) after the friction test are presented on Figure 60. The sample present a dark area in the lower regions of the texture which may represent bone ($Ca_{10}(PO_4)_6(OH)_2$). EDS analysis (Figure 61) was performed on the black area to confirm this and the results revealed the presence of bone characteristic elements (Ca, P), as well as, the presence of the expected Y-PSZ (Zr,O,Y). The presence of Na and Cl chemical elements resulted from the PBS used as lubricant.

SEM images from Figure 62 and Figure 63 represent the surface of the sample P3 and P6, respectively.
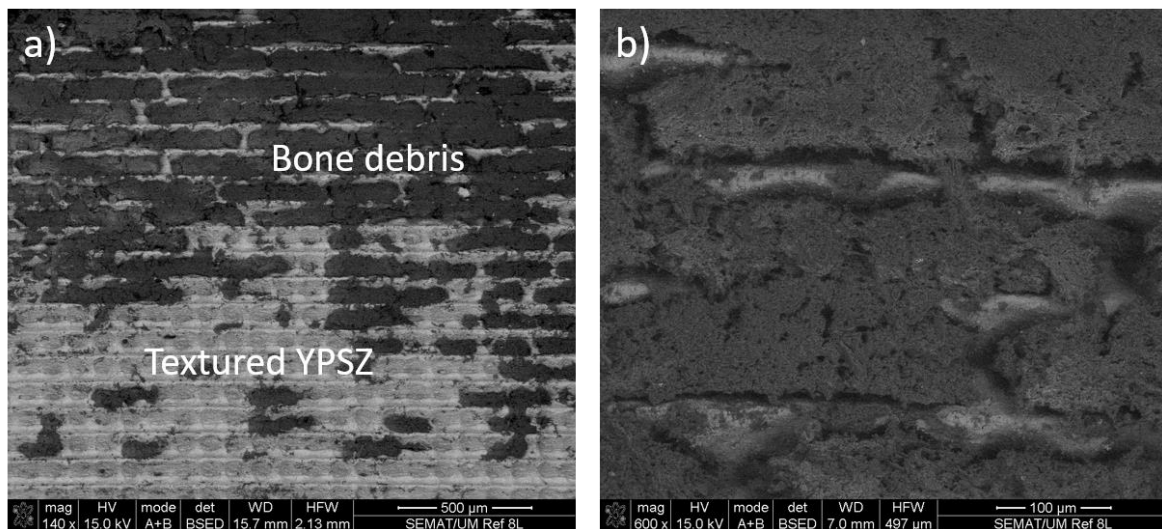
Figure 60 SEM images, from the textured Y-PSZ sample (prior to Ag addition) after the friction test against bone.
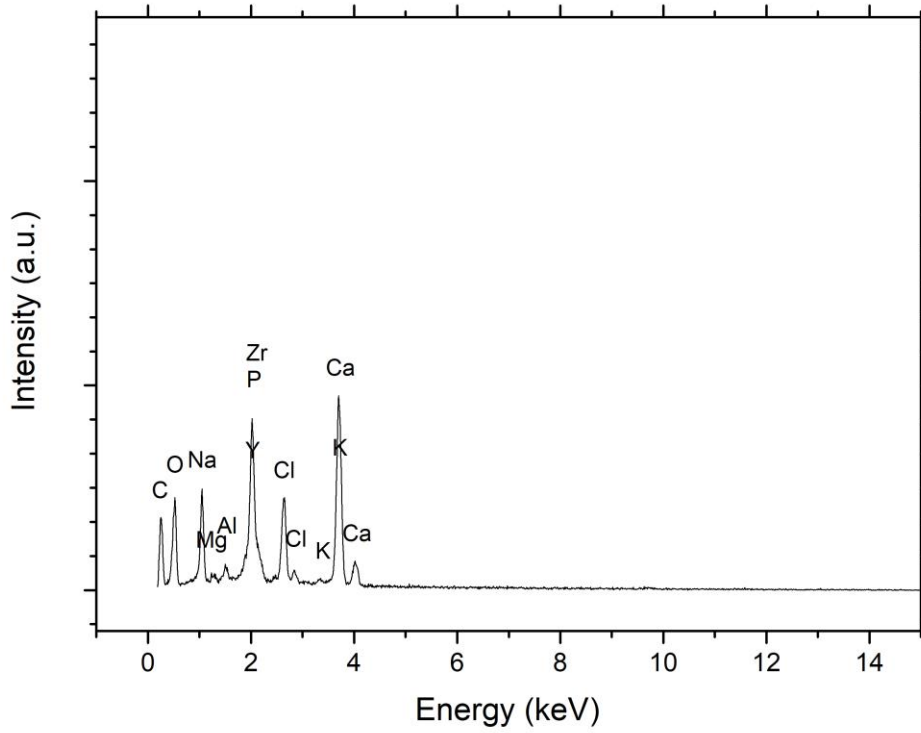
Figure 61 EDS spectrum of the textured Y-PSZ sample (prior to Ag addition) after the friction test against bone.
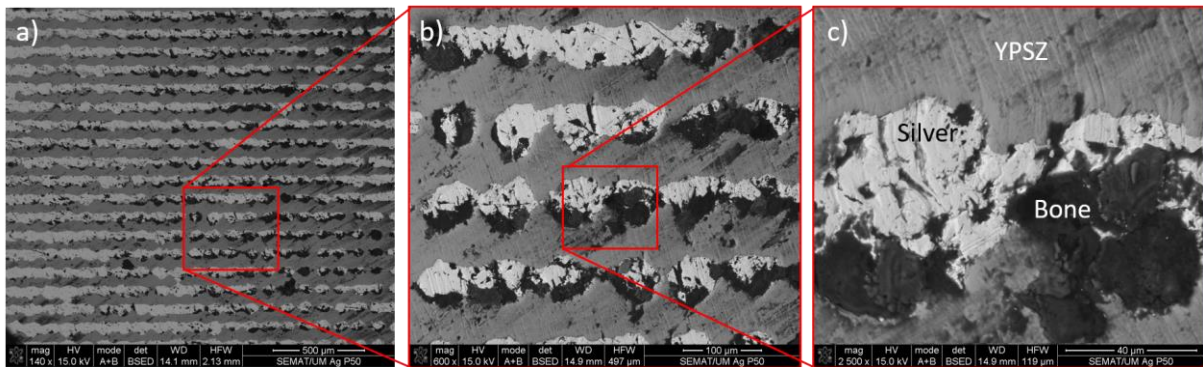
Figure 62 SEM images from sample P3S128N1 after reciprocating friction test against bone.
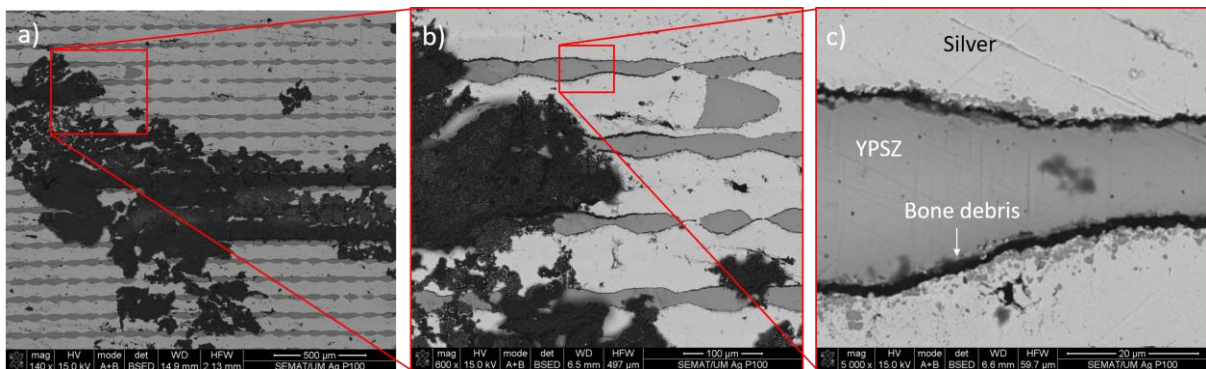
Figure 63 SEM images from sample P6S128N1 after reciprocating friction test against bone.

Three different regions, described by three distinct shades of grey, are visible in the surface of both samples. The dark area may represent bone, and with a closer analysis to both figures (Figure 62c and Figure 63c), it is visible preferential allocation on the interface of both materials, although chemical analysis is necessary to conclude about the composition of each specific region. Considering this, the study proceeded with EDS analysis on three different regions of the surface. The marked areas on Figure 64 represent the analysed regions and the resultant EDS spectra is presented on Figure 65.
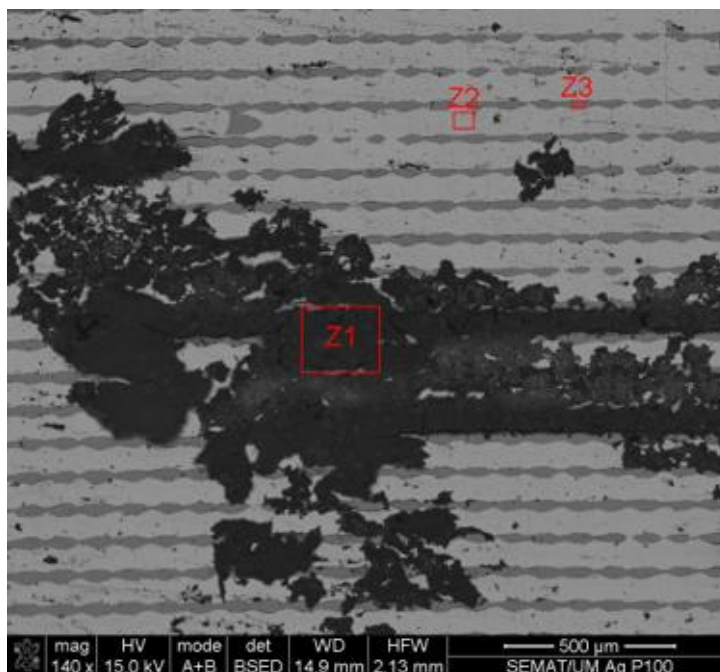
Figure 64 SEM image from sample P6S128N1 after the friction test against bone with marked regions: Z1, Z2 and Z3, for purposes of chemical analysis.
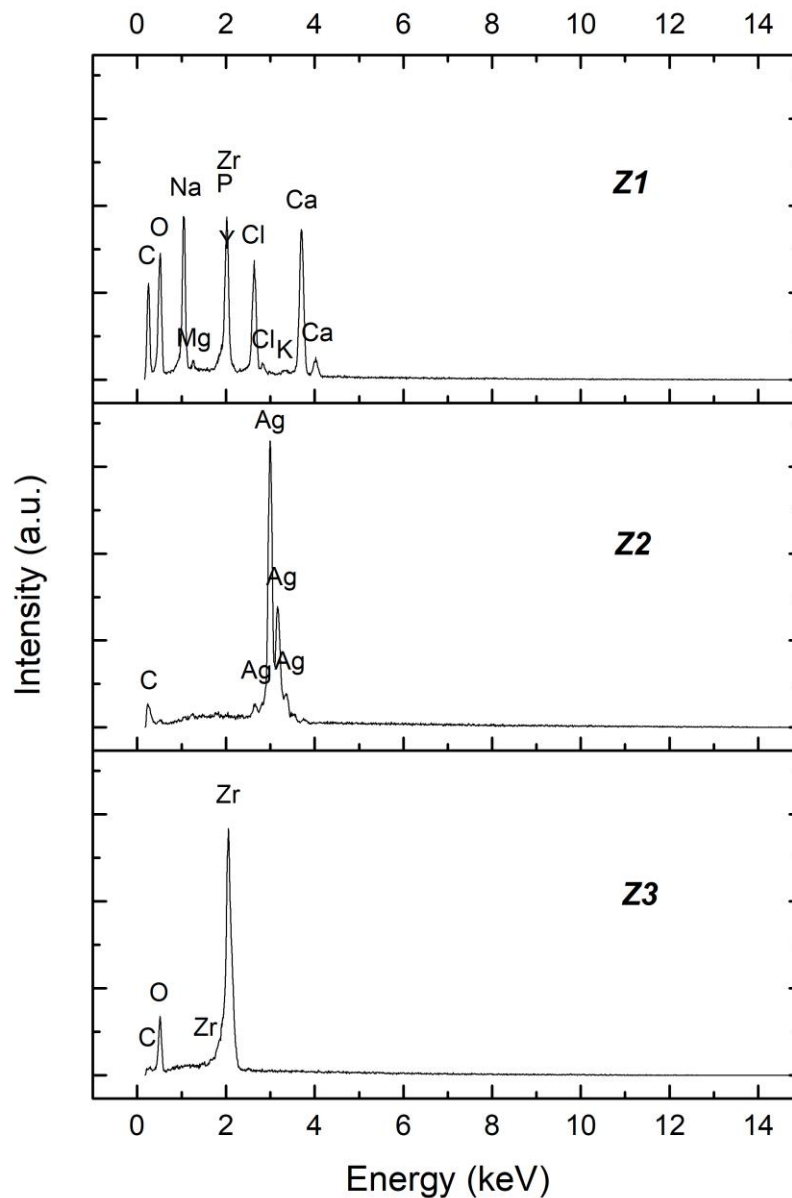
Figure 65 EDS spectra of P6S128N1 sample after reciprocating friction test against bone in different regions, Z1, Z2 and Z3.

The darker region on SEM image, region Z1, has an EDS spectrum similar to the spectrum of the control sample, with high levels of bone and Y-PSZ characteristic elements (Ca, P, Zr, O, Y). Region Z2 (the whiter shade) which occupies the larger portion of the sample surface is identified as Ag, and at last, region Z3 in predominantly composed of Y-PSZ constituents. Elemental composition for the darker region (Figure 66), in the case of sample P3 was also determined, from which resulted a spectrum composed mainly of bone and Y-PSZ constituents (Figure 67).
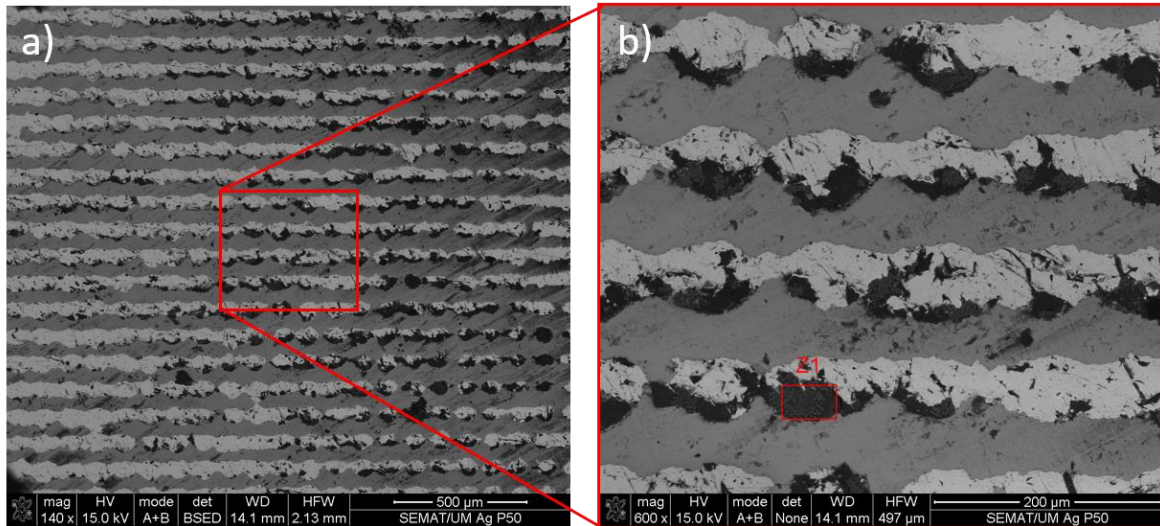
Figure 66 SEM images image from sample P3S128N1 with a marked region (Z1) for purposes of chemical analysis.
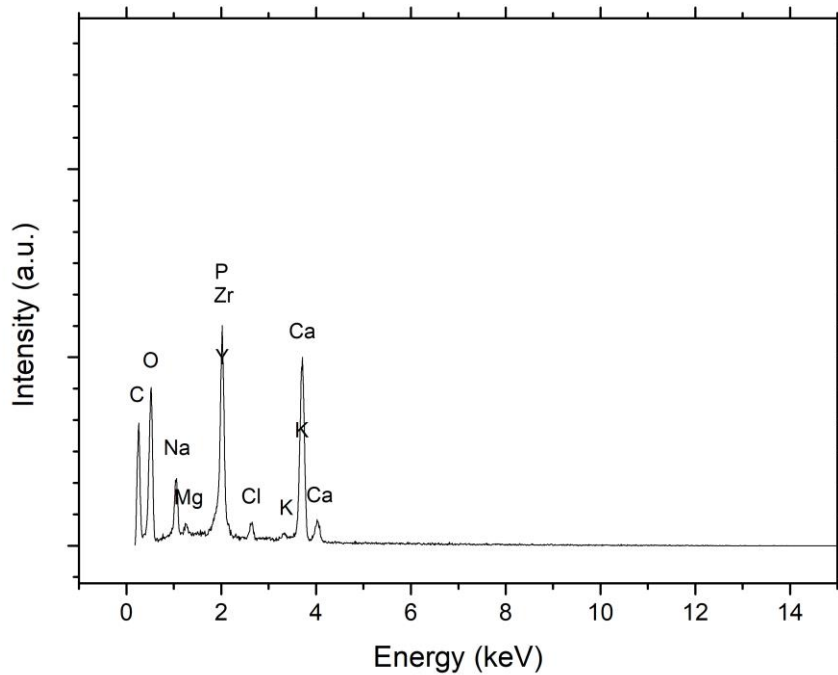
Figure 67 EDS spectrum of region Z1 from sample P3S128N1 after reciprocating friction test against bone.

EDS and SEM analysis confirms the allocation of bone in the material surface which justifies the slight difference between the static initial and final COF values. The abraded bone particles seem to be allocated preferentially in the interface of the materials. Additionally, the SEM images show that there was no silver removal during friction.

4.3 Gold NP's solution

The solutions of gold nanoparticles produced in this work were chemically characterized by atomic absorbance spectroscopy (AAS). After a comparative analysis, one of the solutions produced proceeded to morphological characterization by STEM, where size and particle size distribution were evaluated.

4.3.1 Chemical analysis

By analysing the resulting AAS spectrum for sample 1, 2 and 3 of the NP's solution produced (Figure 68) resulted an absorbance peak of 518 nm for sample 1 and 2 (red and blue line) and of 516 nm for sample 3 (green line) which is in agreement with the characteristic gold NP peak absorption mentioned in literature (addressed in section 2.5.1 from chapter 2). Sample 3 present a much lower absorption intensity when compared to sample 1 and 2, indicating an inferior concentration of AuNP's since a lower absorption peak suggests a lower concentration of the element in suspension. Such observation is explained by the fact that sample 3 was produced by the ablation of ¼ of Au area compared to sample 1 and 2.
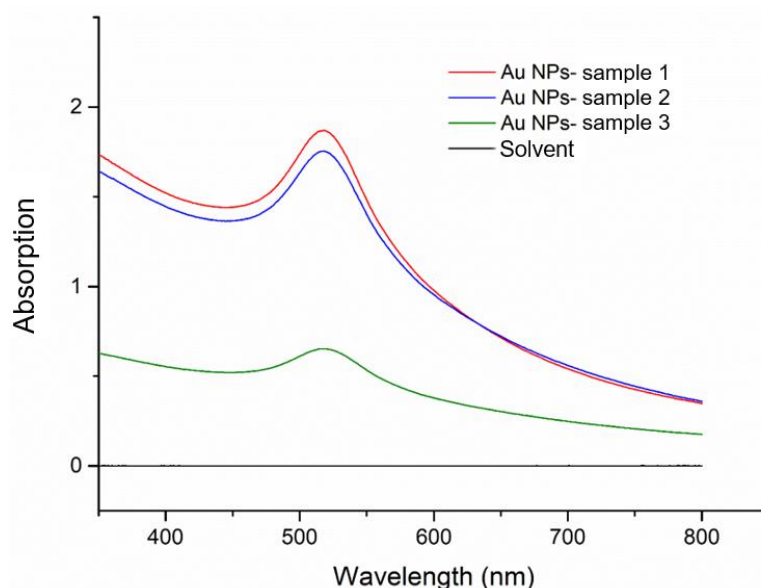
Figure 68 Absorption spectra of sample 1, 2 and 3 of Au nanoparticles prepared by laser ablation in DDW + SDS liquid medium and the control sample (solvent).

The sample which proceeded to morphological characterization was the sample with higher maximum absorption peak, sample 1.

4.3.2   Morphological analysis

Analysis from STEM images of the solution produced (Figure 69) allowed to confirm the presence of nanometric particles in the solution. The NP's obtained are characterized by a spherical morphology and appear in different sizes. To determine the NP's mean size and size distribution, measurements were taken to the NP's using the captured STEM images and image treatment software, Image J. Nanoparticles smaller than 15 nm were produced with a mean size of 5 ± 3 nm. The histogram of size distribution is presented in Figure 70.
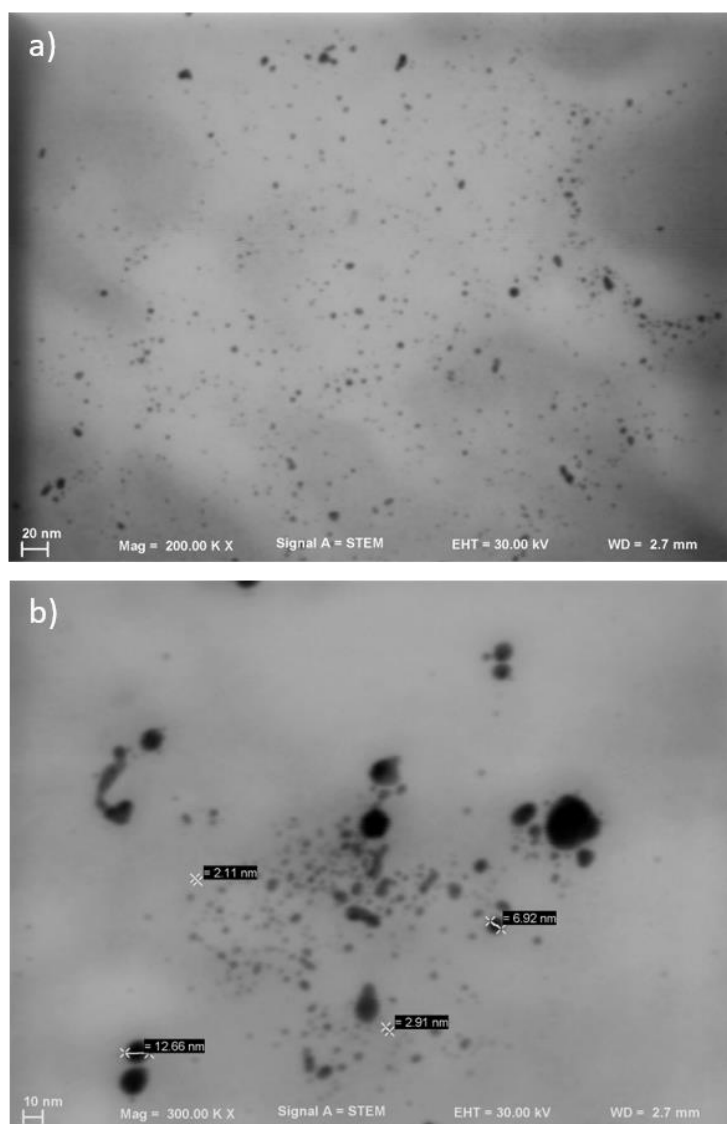
Figure 69 STEM images of the colloidal nanoparticles produced by laser ablation in DDW + SDS liquid medium: a) Image with 200.000 X magnification and b) with 300.000 X magnification.
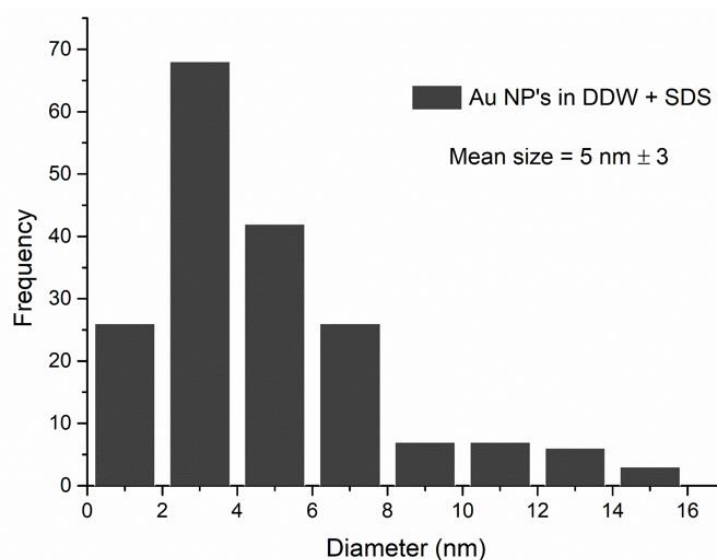
Figure 70 Histogram of the colloidal nanoparticles prepared by laser ablation in DDW + SDS liquid medium.

4.4 Gold surface nano-functionalization

This subchapter presents and discusses three methods of Au NP's surface functionalization. It begins with the optimization of the CO_2 laser parameters, in the first method evaluation and it proceeds with the other method's morphological characterization, with an analysis on NP's agglomerates size and dispersion. The colour effect, on the sample, provided by the laser is also considered. The samples produced with the method presenting better results, proceeded to the reciprocating friction tests, to evaluate the friction performance and the adherence of the AuNP's to the Y-PSZ surface.

4.4.1 Deposition by Irrigation and sintering via laser CO_2

The first method used for Au surface functionalization (Irrigation-deposition $\rightarrow$ Laser-sintering) was pioneer on testing the interaction between the substrate (Y-PSZ) and the laser (CO_2). By selecting a set of laser parameters, evaluating its effect and repeatedly adjusting the parameters, it allowed to reach a parameters combination that favoured NP's adhesion without compromising the material integrity. This laser parameter optimization was crucial on further experiments involving CO_2 laser.

Figure 71, 74, 76 and 78 present the resultant samples obtained in 1º, 2º, 3º and 4º testing group, respectively, as well as, information on the correspondent laser parameters, and 72, 73, 75, 77 and 79 the correspondent OM images.

In the 1º test group it is visible a colour variance in the surfaces of the samples, a soft pink in samples 1, 2 and 3 and a greyish blue in sample 4. This colour effect is an important aesthetic factor on the intended application, being preferable a pink shade to a dark shade. Figure 72 presents the captured OM images corresponding to sample 1 and 2. Image analysis shows the presence of poorly dispersed shinny spots in both samples (Figure 72 b and d), that considering the 50 µm image magnification may represent Au NP's agglomerates. However, surface defects are clearly visible at both magnification lens, namely cracks were formed in both samples, 1 and 2. Also, the reduction from 3 to 2 number of scans didn't seem to attenuate the surface defects.

Test group	Sample	Power (W)	Speed (mm/s)	N° of scans (N)	Line spacing (mm)
1º	S1	15	500	3	0.1
	S2	15	500	2	0.1
	S3	15	1000	2	0.02
	S4	7.5	1000	2	0.02

Figure 71 Photographs of S1, S2, S3 and S4 samples of the second testing group, obtained by Y-PSZ surface Au NP's irrigation and laser sintering procedure and information on the adjusted laser parameters

Figure 72 Optical microscopy images from the 1º group samples surface: a & b) images from sample S1 with 10 X and 50 X magnification, respectively; c & d) images from sample S2 with 10 X and 50 X magnification, respectively.

In sample 3, scanning speed was doubled (500 → 1000 mm/s) and line spacing reduced in ≈ 80 % (0.1 → 0.02 mm). Figure 73 a and b indicate a reduction in surface cracks formation and simultaneously an increase in the number of Au NP's agglomerates. In 10 x magnification (Figure 73b) a melting effect on the Y-PSZ surface is more evident, even though it has been present since the first condition. There was a decrease of 50 % in laser power (15 to 7.5 W) in sample 4 (maintaining all the other parameters from sample 3), by OM analysis no cracks were observed, no Y-PSZ surface re-melting and close to none Au NP's agglomerates are visible (Figure 73c, d).

The 1º samples group analysis showed that decreasing the number of scans (3 to 2) didn't reduce the cracks on the sample, however, when increasing laser speed 100% and decreasing line spacing 80%, at constant laser power and number of scans, a reduction of the cracks was observed. This positive effect could only have been caused by the scanning speed increase. Since a decrease in line spacing should only have increased energy density and caused cracks, which did not, indicating 0.02 mm is a tolerable line spacing. Decreasing the

power in 50 %, eliminated the cracks completely, although, the colour of the sample is highly undesirable considering the application. Also, there is no re-melting indicating that the transition from the original dark colour (before laser scanning-Figure 30 b) to pink, in this process, may have been caused by the laser thermal effect, thus, by Au NP's sintering.
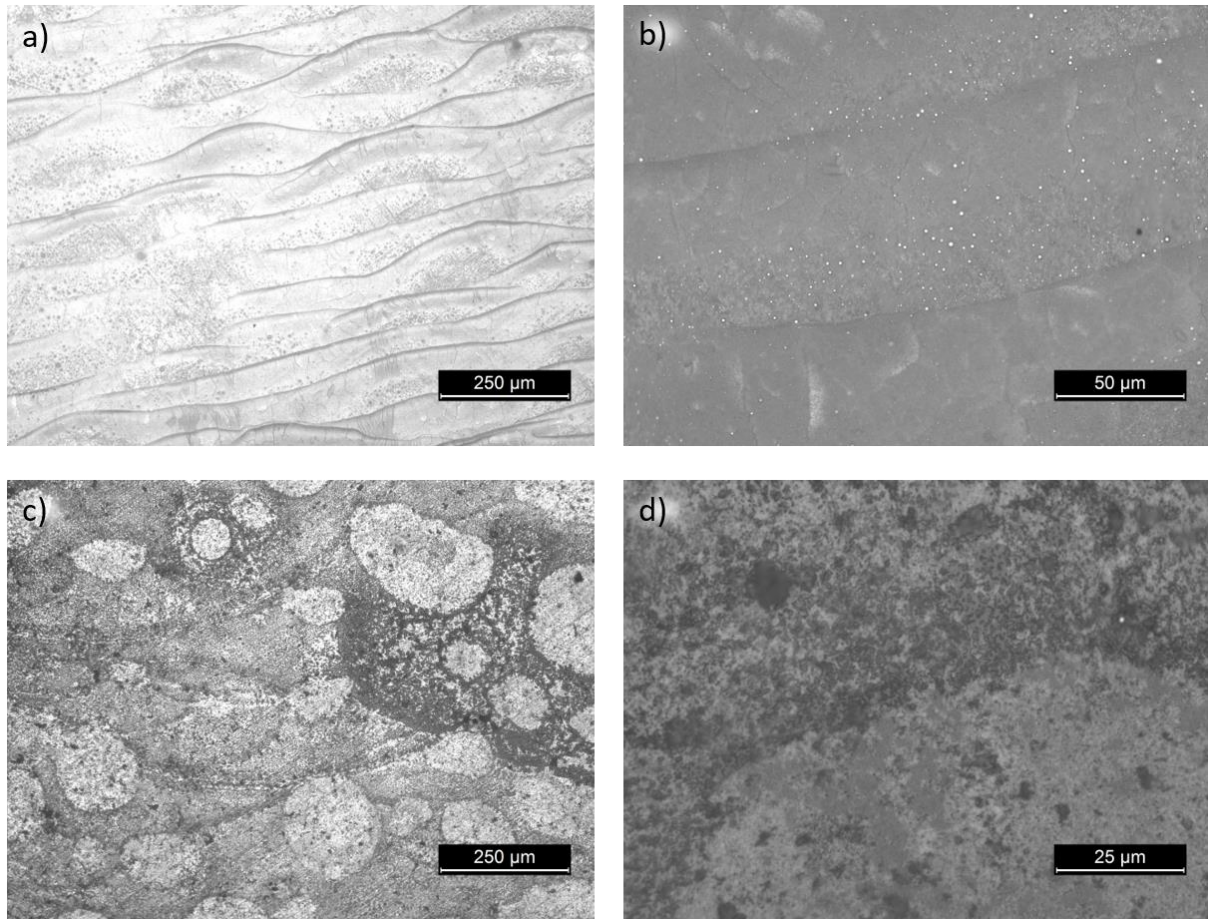
Figure 73 Optical microscopy images from the 1º group samples surface: a & b) images from sample S3 with 10 X and 50 X magnification; c & d) images from sample S4 with 10 X and 50 X magnification.

In 2º group tests (Figure 74), laser power was kept at 7.5 W, speed at 1000 mm/s and line spacing at 0.02 mm, since these parmeters showed no evidence of cracks in the first group of samples. In this group the number of scans was increased (8,16,32), and the resultant colour, as well as, the existance of surface cracks was evaluated. Even though no cracks are observable on OM images of any sample of this group (Figure 75), in samples's photographs from Figure 74, the sample presents a colour indicative that there in no sintering. All the samples show a greyish colour, indicating that increasing the number of scans doesn't favour the sintering process, 10 x magnification OM images (b,d,f) show a irregular layer (unsintered), which difficulted the focus on NP's aglomerates.

Test group	Sample	Power (W)	Speed (mm/s)	N° of scans (N)	Line spacing (mm)
	S1	7.5	1000	8	0.02
2º	S2	7.5	1000	16	0.02
	S3	7.5	1000	32	0.02

Figure 74 Photographs of S1, S2 and S3 samples of the second test group, obtained by Y-PSZ surface Au NP's irrigation and laser sintering procedure and information on the adjusted laser parameters
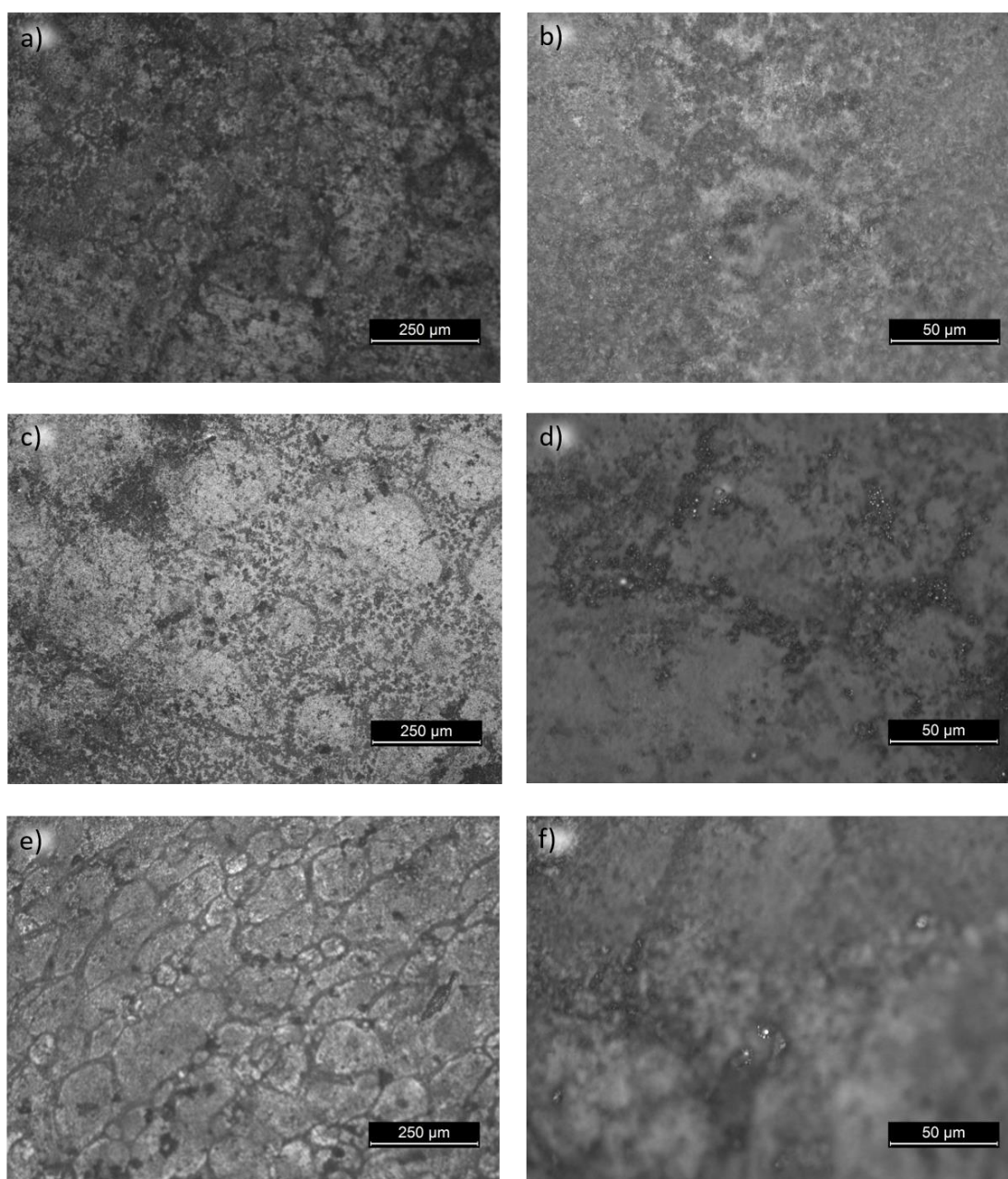
Figure 75 Optical microscopy images, with 10 X and 50 X magnification, from 2º test group: a & b) sample S1; c & d) sample S2 and e & f) sample S3.

Sample 1 from 3º group showed no improvement in colour by increasing laser power from 7.5 to 10 W (Figure 76), and no surface cracks are detected. An appealing colour was attained in sample 2, after increasing laser power in 2.5 W, although, Figure 77c, d show existent cracking on Y-PSZ surface. In other to reduce these cracks, in sample 3, it was given an increasing in line spacing in 3 times, but it returned to a greyish colour. By Figure 77e analysis cracks don't seem to have diminished.

Test group	Sample	Power (W)	Speed (mm/s)	N° of scans (N)	Line spacing (mm)
3º	S1	10	1000	2	0.02
	S2	12.5	1000	2	0.02
	S3	12.5	1000	2	0.06

Figure 76 Photographs of S1, S2 and S3 samples of the third test group, obtained by Y-PSZ surface Au NP's irrigation and laser sintering procedure, and information on the adjusted laser parameters.
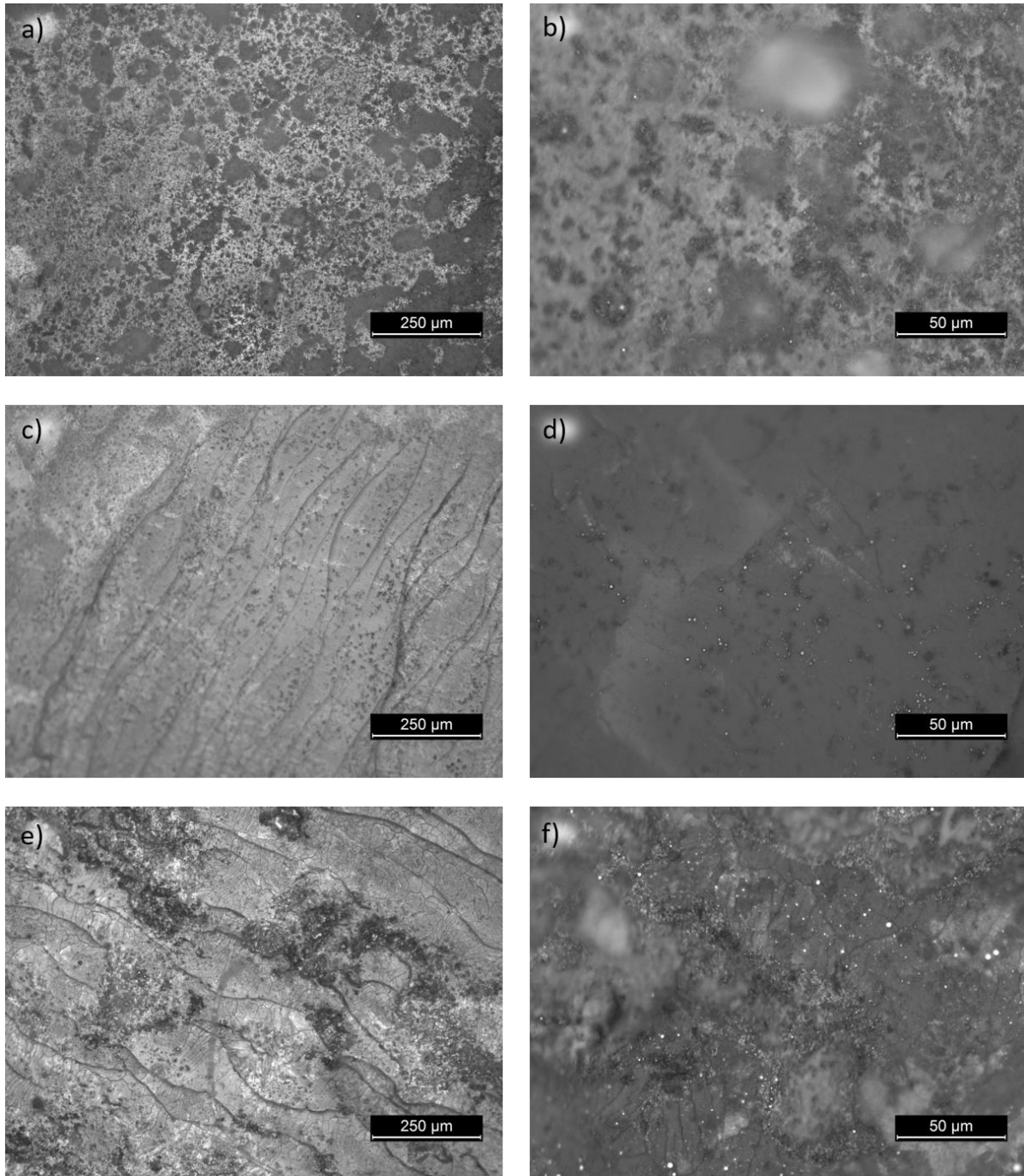
Figure 77 Optical microscopy images, with 10 X and 50 X magnification, from 3º test group: a & b) sample S1; c & d) sample S2 and e & f) sample S3.

In sample 1 from the final test group (4º-Figure 78), instead of increasing laser power and increasing line spacing (as done previously), laser power was decreased (from 12.5 to 10 W) along with line spacing in 1/3 of 0.02 mm (≈0,007 mm). In this way, it is intended to keep the thermal effect without vanishing with the desired colour. However, this decrease in line spacing was too intense and induced cracks, as it is possible to see on Figure 79. Considering this, in sample 2, line spacing was, again, increased to 0.01 mm, corresponding to a 3 μm

difference between S2 and S1. And, in fact, cracks were eliminated (Figure 79), although, the soft pink shade vanished.

The ideal parameters combination was achieved in sample 3 with a slight increase on laser power (from 10 to 11.5 W) and setting line spacing back to 0.02 mm. Sample 3 presents the aesthetic desired colour which is also indicative of the NP's sintering, and simultaneously, show no surface defects on the sample. Thus, these parameters were used in the following experiments involving CO_2 laser and Y-PSZ as substrate.

Test group	Sample	Power (W)	Speed (mm/s)	N° of scans (N)	Line spacing (mm)
4°	S1	10	1000	2	0.007
	S2	10	1000	2	0.01
	S3	11.5	1500	2	0.02

Figure 78 Photographs of S1, S2 and S3 samples of the fourth test group, obtained by Y-PSZ surface Au NP's irrigation and laser sintering procedure, and information on the adjusted laser parameters
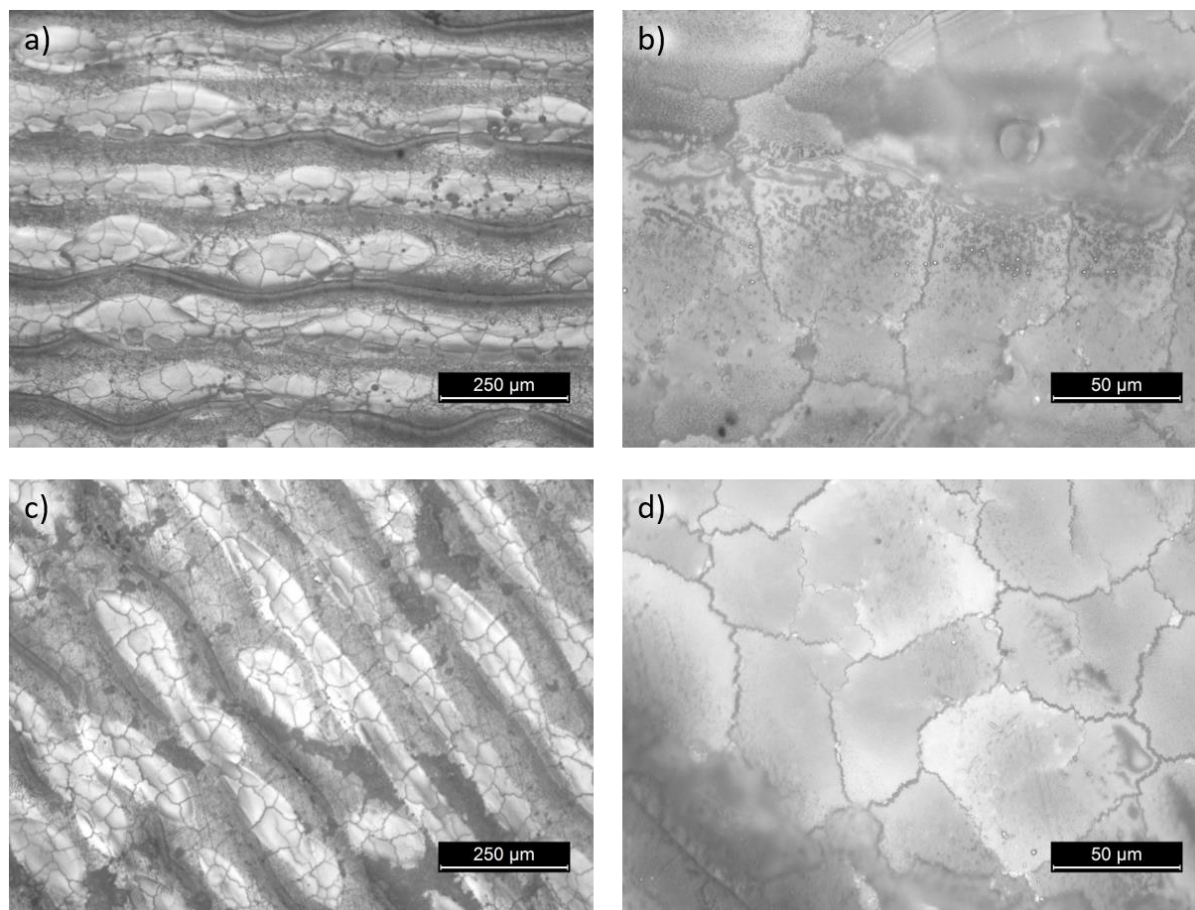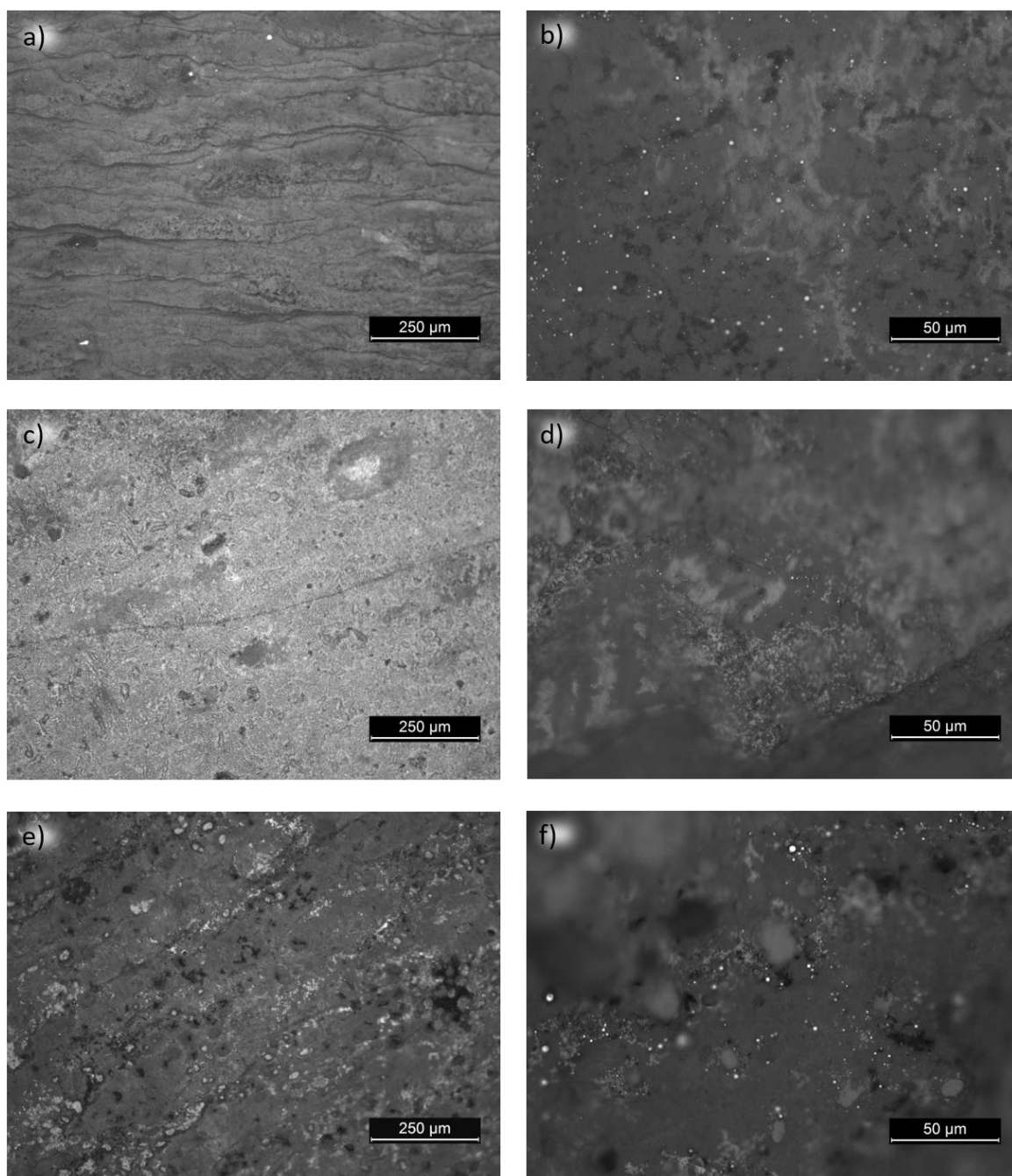
Figure 79 Optical microscopy images, with 10 X and 50 X magnification, from 4º group: a & b) sample S1; c & d) sample S2 and e & f). sample S3.

4.4.2 Deposition by spray and sintering in the oven

The second method used for the Au NP's surface functionalization was deposition by spray and sintering in the oven, a photograph of the sample obtained by this method is presented on Figure 80. The sample present a rose shade that is indicative of the nanoparticles sintering, although after a complete OM analysis to the surface (Figure 81), no traces of nanoparticles agglomerates were detected.

Figure 80 Photographs of the Y-PSZ sample after Au NP's spray and sintering in the oven procedure
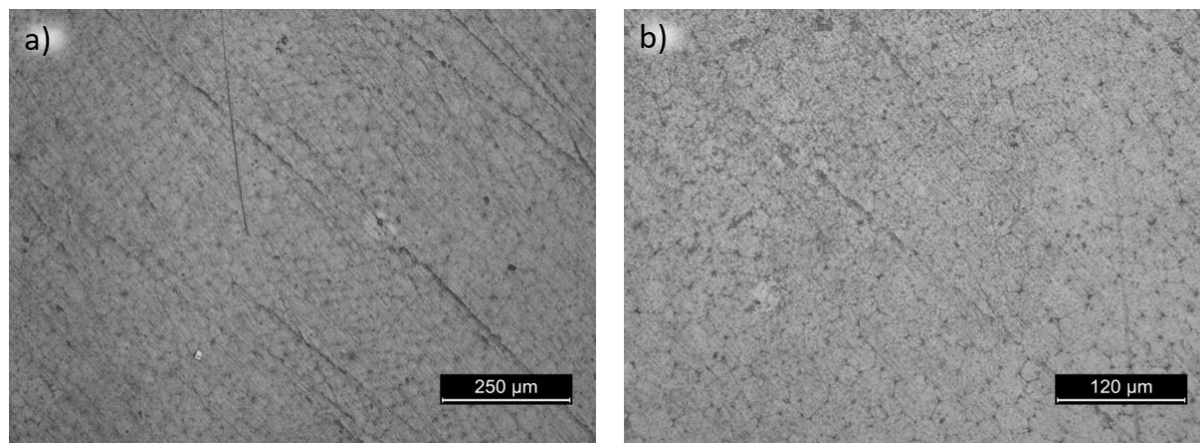
Figure 81 OM images of the sample obtained by spray deposition and sintering in the oven with vacuum.

4.4.3   Deposition by spray and sintering via laser CO_2

The third method used for the Au NP's surface functionalization was deposition by spray followed by laser sintering. Beside the optimal condition resultant from the optimization, a new laser condition was introduced. A slight decrease on the laser power, corresponding to 11 W, and on the laser scanning speed to 1000 mm/s. Figure 82 presents the laser conditions applied in each sample, as well as, the respective photographs, where 60 doses of Au solution were purged.

Condition	Power (W)	Speed (mm/s)	N° of scans (N)	Line spacing (mm)
A	11.5	1500	2	0.02
B	11	1000	2	0.02

Figure 82 Photographs of the samples obtained by spray of Au NP's solution and laser sintering procedure, using laser conditions A and B, and description of the laser parameters.

Both samples present a pale rose tonality with a very homogeneous surface colour. Next step consisted on testing the best combination of spray purges with laser passages. The colour of the sample did not change with the different combination of purges. Optical microscope images from Figure 83 and Figure 84 show the samples obtained from the 3 combinations of purges tested: a) & b) Sixty purges of Au NP's solution followed by 2 passages of laser, b & d) 2 X repetition of a combination of 30 purges of Au NP's solution with 1 passage of laser, e & f) 20 purges of Au NP's solution and 1 passage of laser followed by 40 purges of Au NP's solution and 1 final passage.
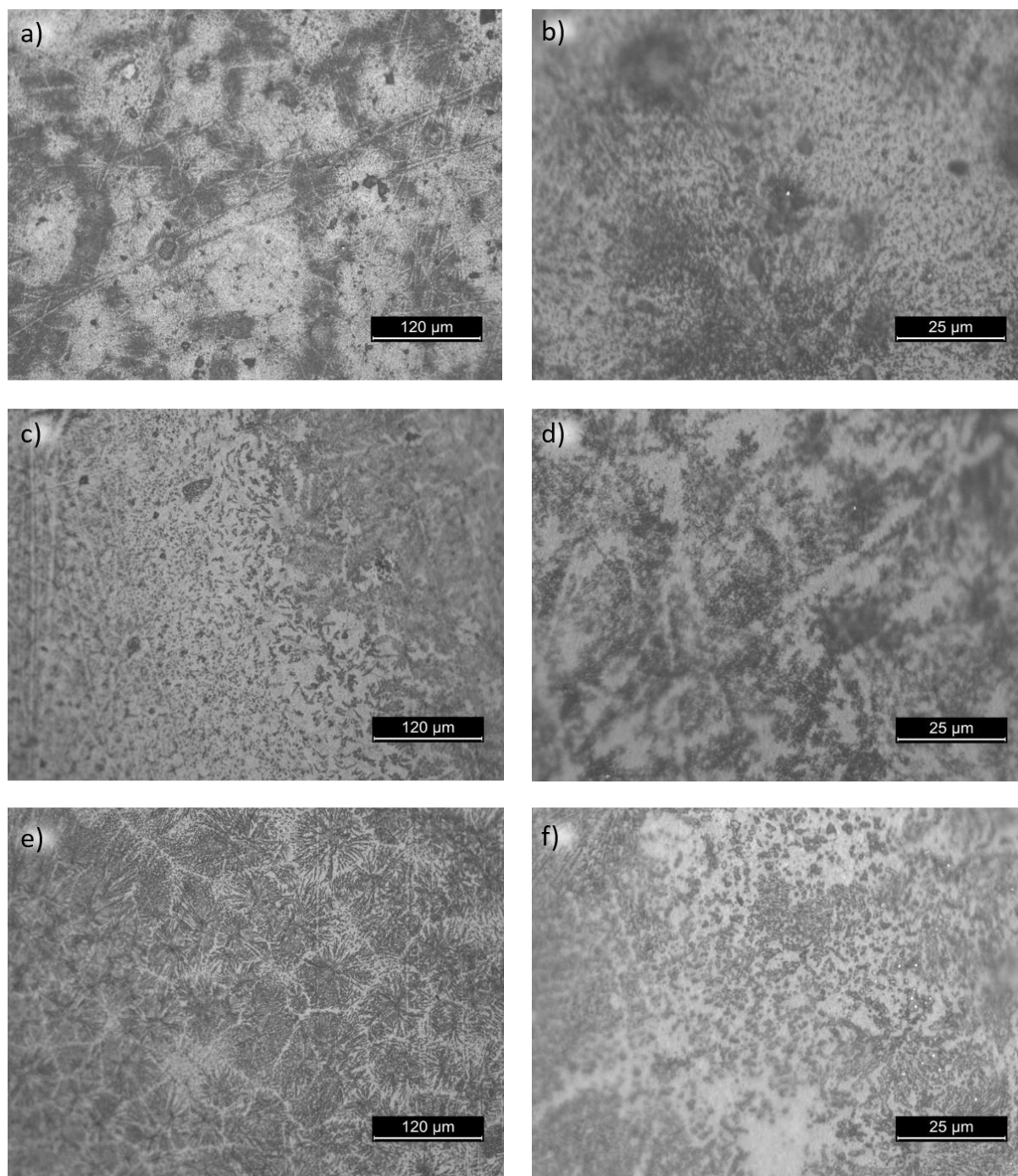
Figure 83 Optical microscopy images of the sample obtained with laser condition A, with 20 X and 100 X magnification of the spray deposition followed by laser sintering procedure used on Y-PSZ Au nano-functionalization. a & b) Sixty purges of Au NP's solution followed by 2 passages of laser, b & d) Set of 30/30 purges of Au NP's solution combined with 1/1 passages of laser, e & f) Set of 20/40 purges of Au NP's solution combined with 1/1 passages of laser.
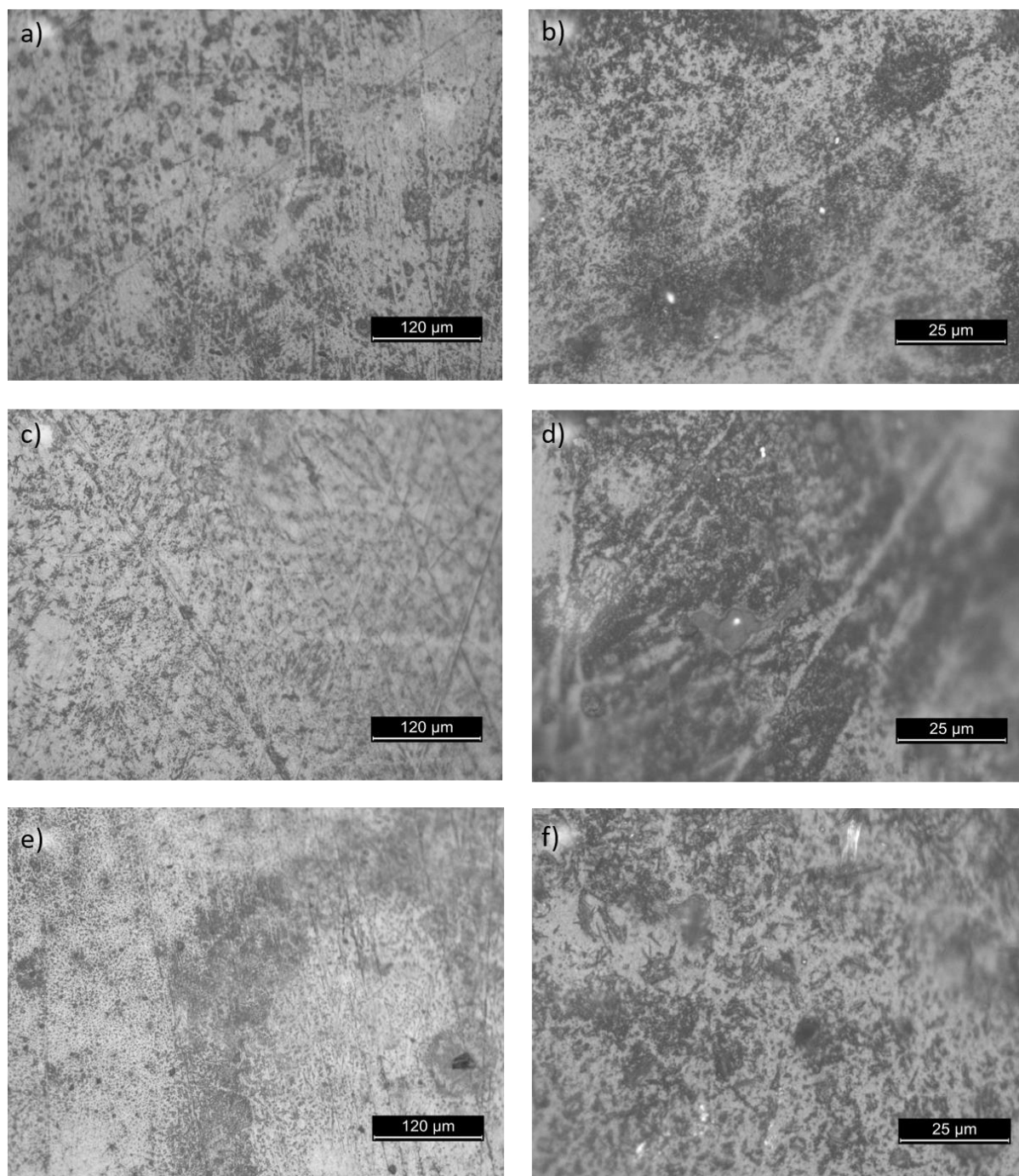
Figure 84 Optical microscopy images of the sample obtained with laser condition B, with 20 X and 100 X magnification of the spray deposition followed by laser sintering procedure used on Y-PSZ Au nano-functionalization. a & b) Sixty purges of Au NP's solution followed by 2 passages of laser, b & d) Set of 30/30 purges of Au NP's solution combined with 1/1 passages of laser, e & f) Set of 20/40 purges of Au NP's solution combined with 1/1 passages of laser.

Both samples show no evidence of cracks, and NP's agglomerates are very few in the 100 X magnification when compared to irrigation depositing method. Comparing the different combinations, it seems the 20/40 purges of Au NP's solution combined with 1/1 laser passages (Figure 83e, f & Figure 84e, f) show more quantity of NP's agglomerates. Although, SEM analysis needed to be performed to deliver a more precise analysis.

Of the three methods of Y-PSZ Au NP's functionalization, two showed positive results, since in the procedure involving the oven at vacuum no NP's agglomerates are detected. Samples obtained by the 3º method (spray deposition and laser sintering) present better colour homogeneity and clearance on OM images compared to the method using deposition by irrigation, therefore, this method will proceed to the following characterization.

SEM Images of the Au NP's functionalized Y-PSZ surface, obtained with 20 purges of Au NP's solution and 1 passage of laser followed by 40 purges of Au NP's solution and 1 final scan using laser conditions A and B, are presented on Figure 85a, b and Figure 85c, d respectively.
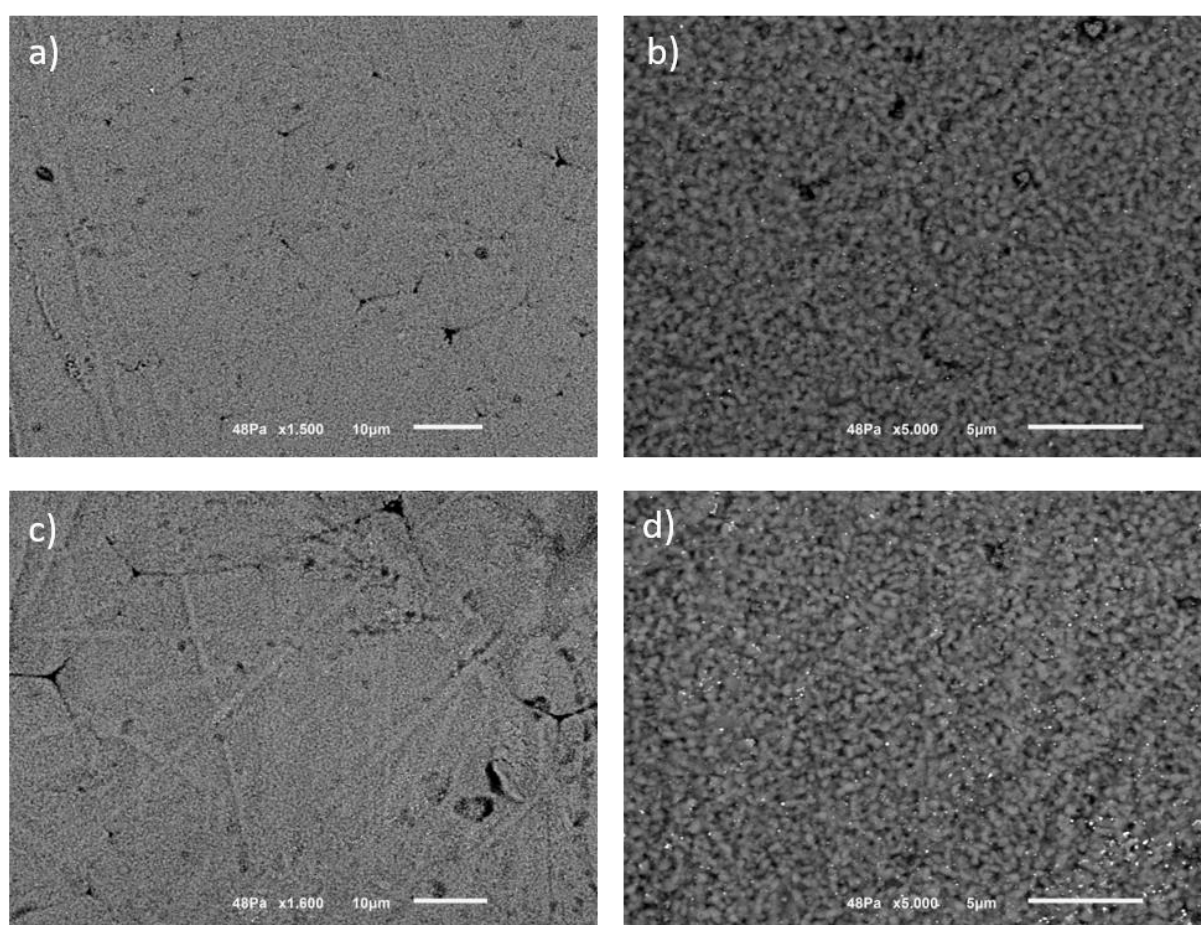
Figure 85 SEM images of Au NP's functionalized Y-PSZ obtained by spray and laser sintering procedure: a & b) Laser sintering using laser condition A, with 1500 X and 5000 X magnification, respectively; d & e) Laser sintering using laser condition B, with 1500 X and 5000 X magnification, respectively.

SEM images analysis confirm the presence of NP's in Y-PSZ surface, in both laser conditions. Also, in both conditions, the NP's seem to be very well dispersed. Looking at 5000 X magnification images, a low amount of agglomerates is visible when compared to NP's alone, especially in the samples obtained using laser condition A (Figure 85b).

The samples obtained by using laser condition A and B will, from this point, be referred as sample P11.5 and P11, respectively.

4.4.4 Reciprocating friction test

As previously mentioned in this work, friction tests were employed to study the friction performance and the adherence of the AuNP's on the Y-PSZ surface. The coefficient of friction (COF) results obtained from the experiments are presented in Figure 86.
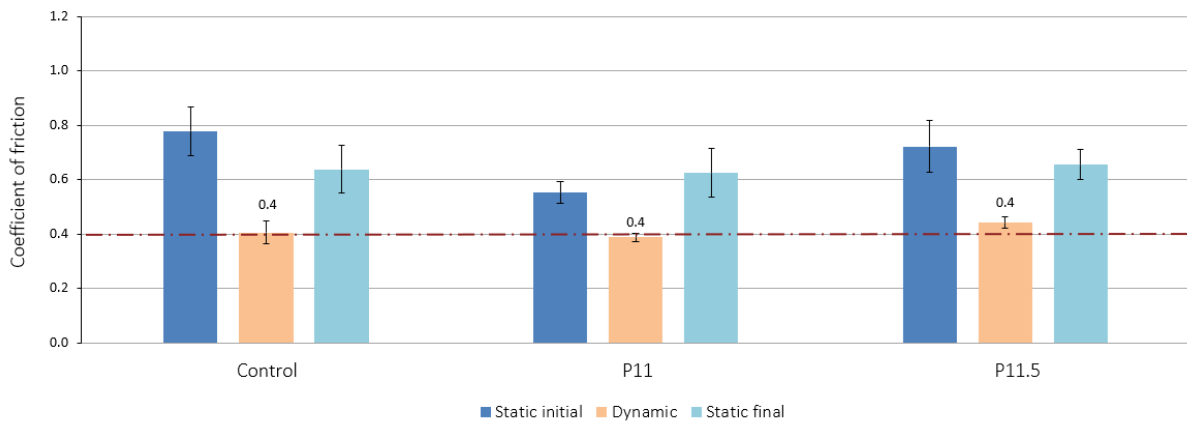
Figure 86 Average static initial, dynamic and static final coefficient of friction (COF) from conditions P11 and P11.5 and the control sample.

The results from the friction tests revealed an average dynamic COF of 0.4. The static initial and static final values are higher than 0.4 for all the samples as expected. Both conditions (P11 and P11.5) have a friction behaviour similar to the control sample, thus, it is possible to conclude the laser treatment applied in this experiment did not affect the COF of the sample.

Considering that the static initial and the dynamic stages represent the insertion of the implant, the final static friction test may represent the force necessary to displace it. Since no significant decrease was observed between the initial and final static COF in conditions P11 and P11.5, the friction seemed not to affect the COF of the samples, neither the primary stability potential of the material. This may be a good indicative of the primary stability of the implant and of the potential of application of this material at lower regions of the implant.

After the reciprocating friction test, the samples went through morphological and chemical characterization. SEM images of sample P11 with different magnifications are presented in Figure 87. From the analysis of these images it is possible to discriminate 2 regions, a whiter which seems to represent Y-PSZ, and a darker region which is likely to be

abraded bone, additionally, some shiny spots are detectable in the higher magnification image (Figure 87b), demonstrating the prevalence of the NP's added to the Y-PSZ surface. A much clearer region of the surface is shown in SEM images from Figure 88 where the NP's are well defined and range from approximately 8.7 to 51 nm (Figure 88b). The actual composition of this sample was evaluated through EDS, either on the darker (Figure 87) as in the whiter regions (Figure 88), accordingly, the resulting spectra is presented in Figure 89.
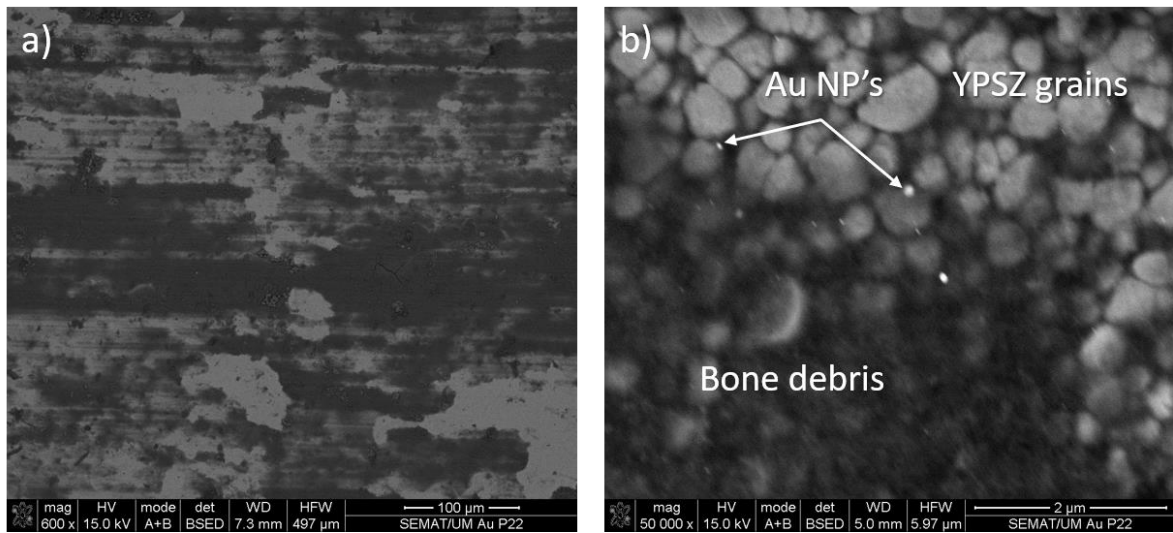
Figure 87 SEM images from sample P11 of a darker region of the surface after reciprocating friction test.
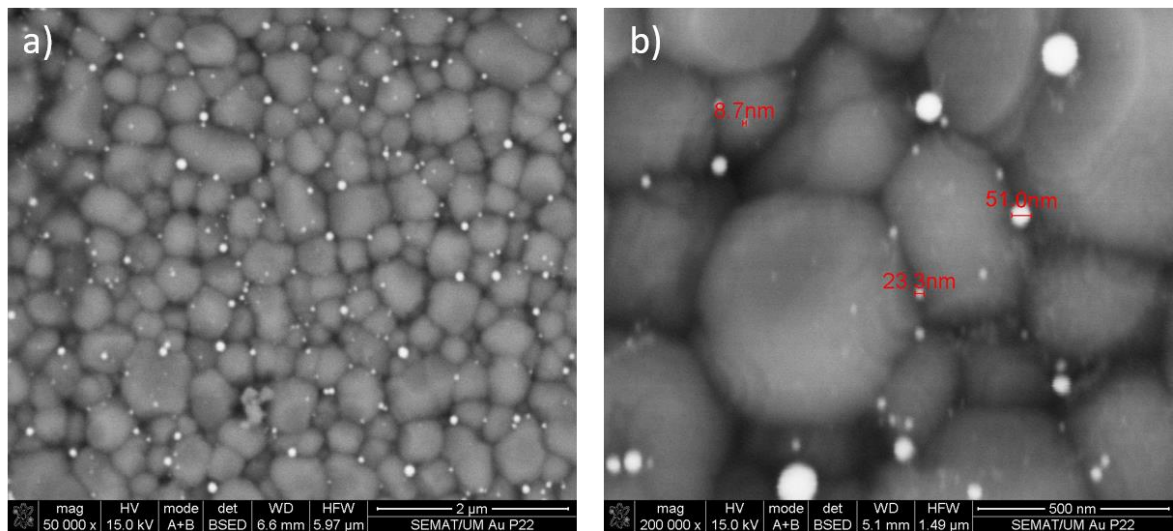
Figure 88 SEM images from sample P11 of a whiter region of the surface after reciprocating friction test.
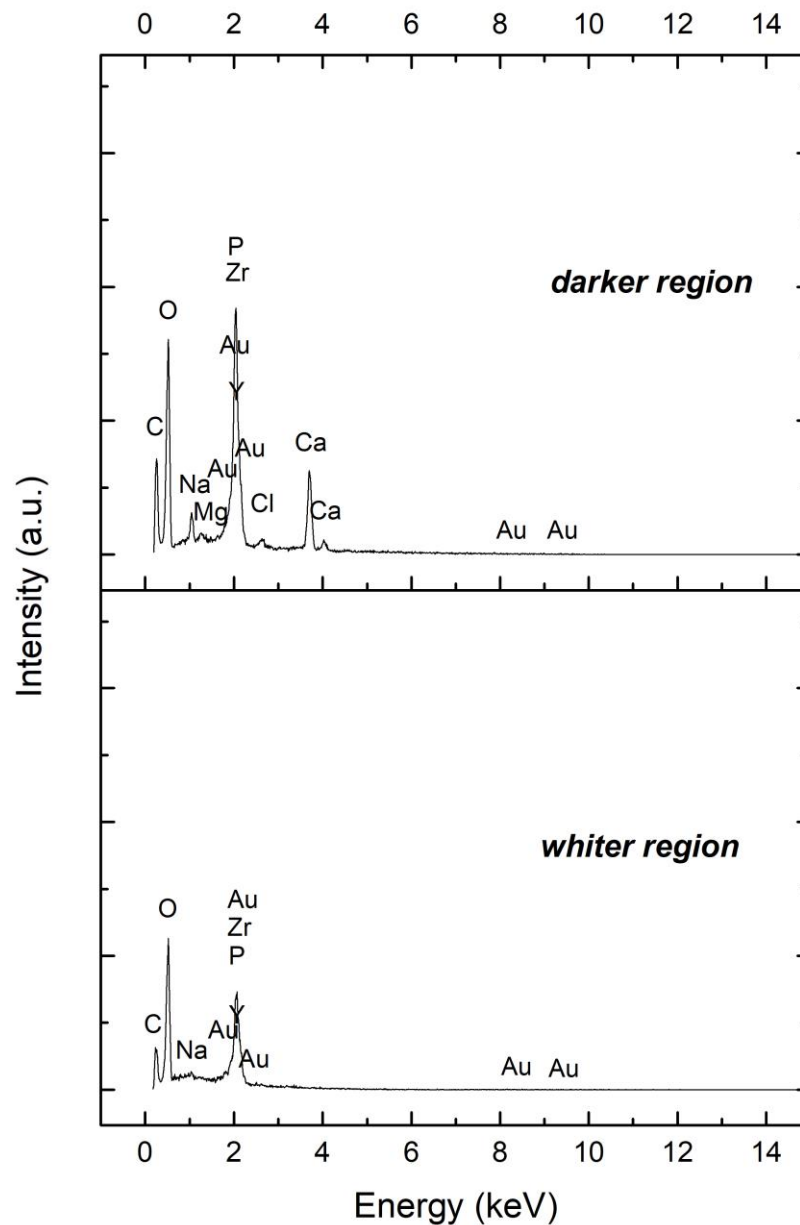
Figure 89 EDS spectra of sample P11 after reciprocating friction test against bone in two different regions. A darker (bone debris) and whiter region (Y-PSZ + Au).

Both spectrums are very conclusive, bone constituents (Ca and P) and Au coexist in the same area (darker region) of the surface, which indicates that the Au NP's did not detached from the substrate with the friction effect against the bone, revealing a good adhesion of the particulates.

The sample P11.5 has a similar morphology after friction as the previous sample studied, as shown in Figure 90 and Figure 91. Nanoparticles are visible in the middle of the dark shade region while in the whiter region nanoparticles are perfectly discriminated with

diameters from 13.1 to 43.7 µm and, in a similar way to the elemental composition spectra of the previous sample, Au and bone are the principal constituents detected at the region analysed (Figure 92).
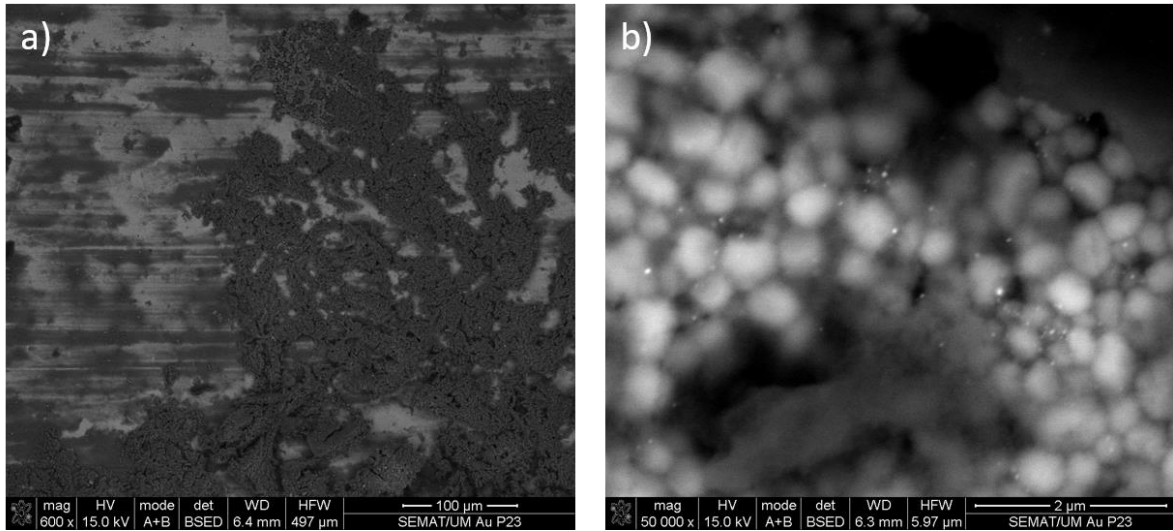
Figure 90 SEM images from sample P11.5 of a darker region of the surface after the reciprocating friction test.
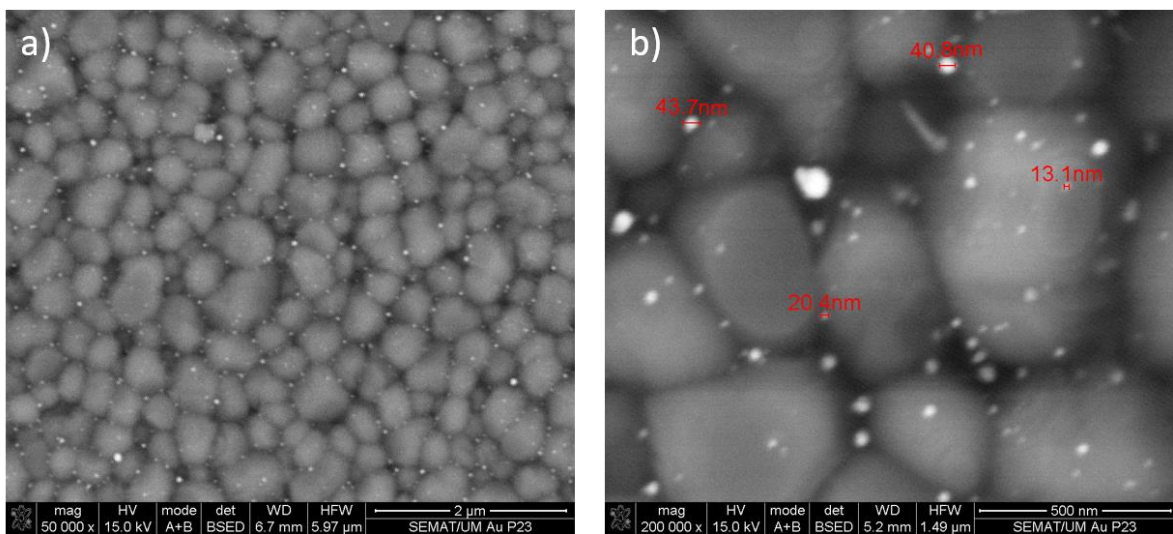
Figure 91 SEM images from sample P11.5 of a whiter region of the surface after the reciprocating friction test.
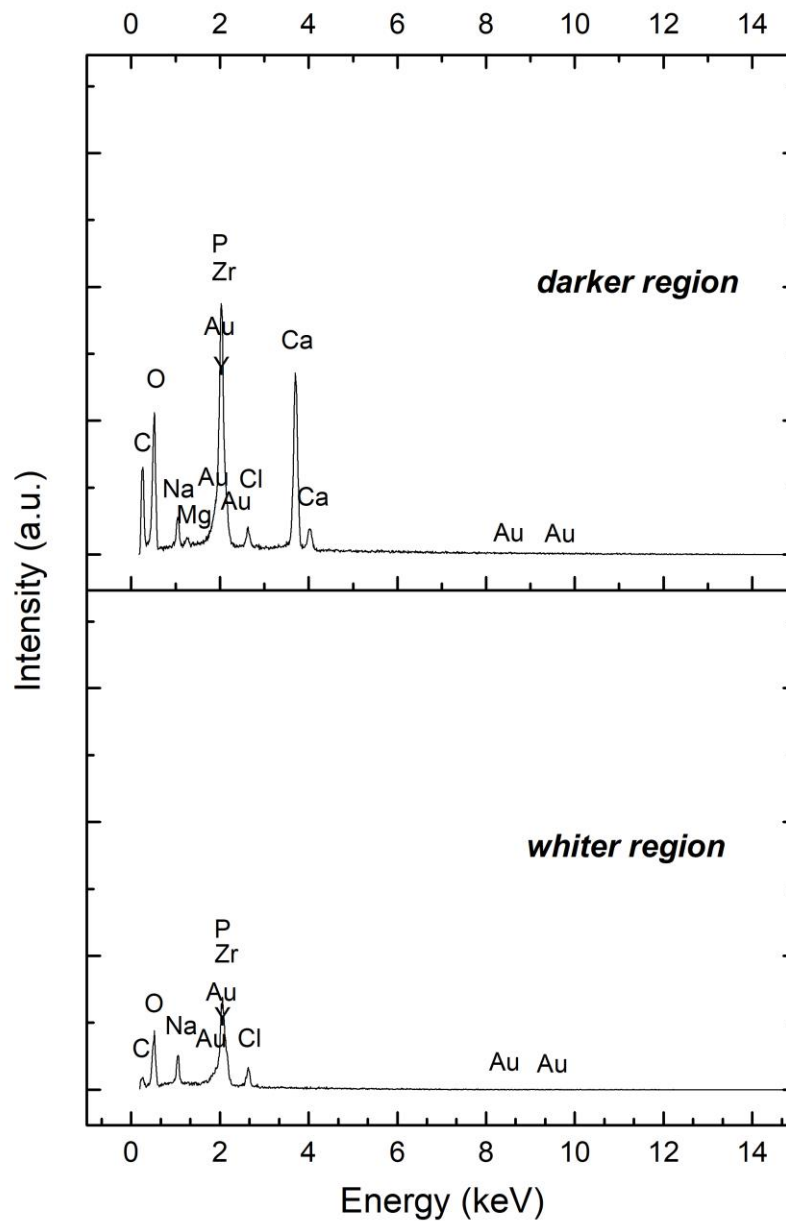
Figure 92 EDS spectra of sample P11.5 after reciprocating friction test against bone in two different regions. A darker (bone debris) and whiter region (YSTP + Au).

4.5 Overall discussion

This work begins with a study of the laser ablation parameters influence in the resultant profile dimensions of the grooves, namely, groove width, groove depth and ridge width. From this study, ten different grooves were selected based on its profile dimensions and were reproduced parallelly on a surface to introduce in the mechanical tests. Nine different fully texturized samples were divided in three groups: One group of grooves with

increasing groove width (36.4 µm, 57.5 µm and 88.3 µm), a second group with increasing groove depth (12.2 µm, 57.6 µm and 137.1 µm), and the third with increasing groove ridge (11.1 µm, 21.9 µm and 41.1 µm) to evaluate the influence of each dimensional parameter during the mechanical interlock test to artificial soft tissue. Additionally, a sample was produced with dimensions cited in literature (width: 21.8 µm, depth: 4.5 and ridge: 7 µm) to introduce in the study. The 11 samples (including the control) were mechanically evaluated and the results showed that the creation of microgrooves on Y-PSZ surface results on an improvement on the retention level of the artificial soft tissue. It was noticed a proportionality between groove width and depth and the mechanical retention, not so evident in the case of the ridge width. The condition related with the literature review (on soft tissue cell attachment) presented one of the lowest critical interlock load values. Finally, the roughness evaluation showed an increase in roughness caused by the laser processing.

The micro-functionalization of Y-PSZ with silver began with a study about the best of two patterns to increase Ag adhesion, a fine pattern and a coarser pattern. The pattern which resisted to the ultrasonic adhesion test was the coarser pattern, indicating a general mechanical mechanism of adhesion at the interface of Y-PSZ and Ag. A total of 20 laser conditions were tested in the Ag sintering stage, from which two conditions resisted to processing and to the ultrasonication and proceeded to characterization. Despite the existence of some defects at the surface, the morphological analysis indicates a good attachment between silver and Y-PSZ. The cross-sectional analysis suggests a well densified layer of silver; however, some morphological defects are observable at the lower regions of the pattern, which seemed to be related with the depth capacity of the laser. Finally, the samples went through reciprocating friction tests, followed by SEM/EDS in order to analyse its surface. Despite the evidence of friction, showed by the presence of bone allocated at the surface, no silver was detached from the surface revealing a good adhesion.

The production of the gold NP's by laser ablation was successfully completed. The morphological analysis revealed a NP's mean size of 5 ± 2 µm. A gold characteristic peak of 518 nm was confirmed by AAS.

The nano-functionalization of the Y-PSZ surface with Au began with the laser parameters optimization to study the interaction between the laser and the substrate. Fourteen laser conditions were tested until two optimal conditions were reached. Subsequently, three methods combining different procedures of deposition and sintering

were tested from which one was selected to proceed with characterization. The selected technique was spray deposition and laser sintering, based on NP's agglomerates content, surface homogeneity and selectivity of the laser process. In a similar way to silver, SEM and EDS analysis was performed after the friction tests. A layer of adhered bone is evident beneath which NP's are still visible, indicating that the NP's were preserved during the reciprocating friction test. In addition, there was no significant difference between the friction behaviour of the processed samples and the control which indicates that this functionalization technique does not affect the COF of the sample.

These preliminary results are very promising and suggest a high viability of the materials produced for application on dental implants.

The three different solutions proposed and studied in this work can function independently. However, it would be highly advantageous to combine them in a dental implant design with three distinct regions, times and modes of antibacterial action. To take advantage of the inherent potential of each alternative, a possible strategy would involve a design with three distinct regions, as schematized in Figure 93:

A) A primary implant region of interaction with bacteria, composed of finely dispersed Au NP's, to promote a *biocidal effect*. Nanoparticles high specific surface area may enhance a high dissolution rate in biologic medium and promote a short-term effect. Thus, to take the maximum advantage of the Au NP's functionalized surface potential, an immediate interaction with bacteria is required;

B) The *physical barrier,* the development of microgrooves on the implant surface, would act as a second region of action, increasing the retention of soft tissue to the surface and preventing the entry of bacteria to the implant zone;

C) A third implant region with an Ag ring which ensure a *biocidal effect* at a lower soft tissue level. The Ag micro-functionalization would complement the Au nano-functionalization by providing a long-term bactericidal action (assuming that the microscale Ag layer presents lower dissolution in biological medium).
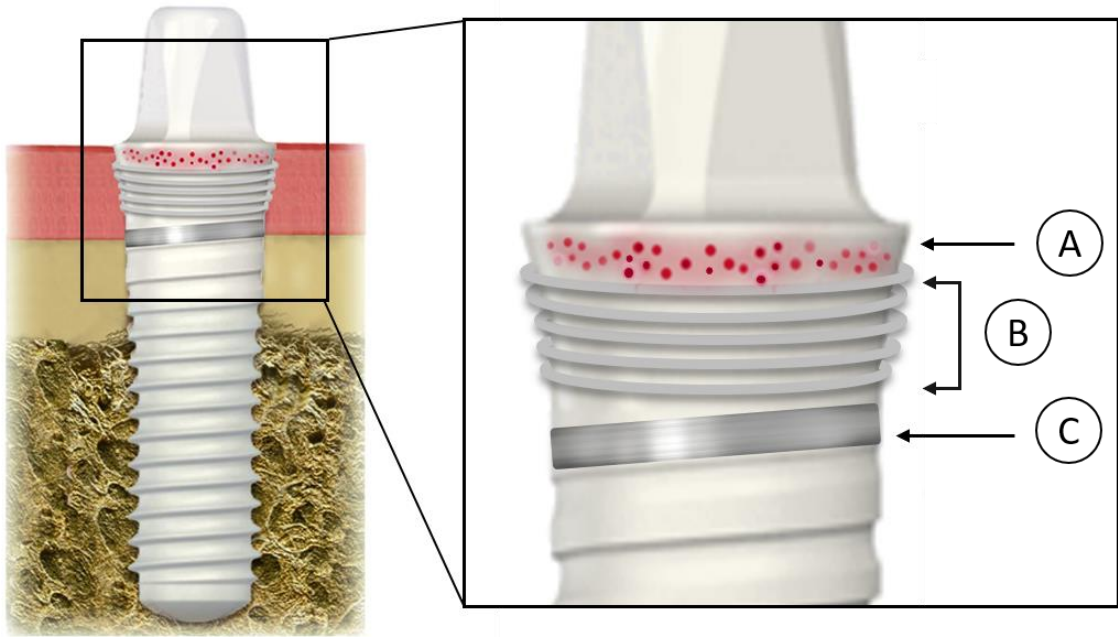
Figure 93 Illustration of a potential design resultant from the combination of the three solutions proposed in the present work: region A- gold nano-functionalized surface (biocide effect), region B: micro grooved surface (physical barrier), region C: silver micro-functionalized (biocide effect).

CHAPTER 5

CONCLUSIONS

Chapter 5 presents the main **conclusions** drawn from this dissertation and present some suggestions for **future works**.

The main objective of the present dissertation was the development of a zirconia surface with the ability to interact with bacteria in two ways, as physical barrier and as a biocide. The barrier effect would be accomplished with the production of laser processed microgrooves. And, the biocide effect, with the production of Ag micro and Au nano-functionalized Y-PSZ surfaces. Therefore, from the obtained results in this work some conclusions can be drawn:

∴ Microgrooves with different profile dimensions were produced and reproduced onto the surface of Y-PSZ by laser ablation. The mechanical interlock test revealed an improvement in the retention of the artificial soft tissue. The surface roughness increases with the laser processing;

∴ Microscale silver was deposited and sintered on the Y-PSZ texturized surface without introducing morphological defects on the substrate.

∴ Despite the evidence of some defects on the Ag functionalized surface, silver seems to be very well attached to Y-PSZ. Cross sectional analysis indicates a good densification of the silver although the lower regions of the texture present some defects;

∴ The coarser texture showed to be more effective on adhesion of micro Ag on Y-PSZ surface by laser sintering comparatively to the fine texture;

∴ A ≈ 5 nm gold NP's colloidal suspension was successfully produced by laser ablation technique;

∴ Three methods of Au NP's functionalization were tested and the one presenting best morphological results proceeded to chemical and mechanical characterization. Thus, the Y-PSZ surface was functionalized by a hybrid process of spray deposition and laser sintering;

∴ The laser parameters, regarding Au NP's sintering, were optimized with success. The NP's were deposited without compromising the Y-PSZ surface structural integrity;

∴ Reciprocating friction tests were performed on the micro and nano-scale functionalized surfaces and the materials did not disintegrate during friction despite the evidence of adhered bone on its surface. Additionally, the surfaces presented a high final COF which predicts a good primary stability of the implant.

The results of this study are very promising and suggest a high potential of the solutions proposed to solve the problem of peri-implantitis.

Furthermore…

In the context of the application, it would be interesting to:

- Proceed with an overall improvement of the micro Ag functionalization processing;

- To analyse the bone plates used in the reciprocating friction tests of the chemically functionalized surfaces;

- Evaluate the epithelial cells response to the microgrooves created;

- Study the dissolution rate of the Ag microparticles and of the Au nanoparticles over a pre-determined period (hours to days);

- Determine the cytotoxicity of the surfaces produced to mammalian cells;

- Study the antibacterial potencial of the surfaces created in a bacterial incubation test.

REFERENCES

[1]   M. Singh, L. Kumar, M. Anwar, & P. Chand, "Immediate dental implant placement with immediate loading following extraction of natural teeth", *National Journal of Maxillofacial Surgery*, vol. 6, pp. 252–255, 2015.

[2]   L. Gaviria, J.P. Salcido, T. Guda, & J.L. Ong, "Current trends in dental implants", *Journal of the Korean Association of Oral and Maxillofacial Surgeons*, vol. 40, pp. 50–60, 2014.

[3]   R. Alsadeg, "Dental Implants - Success Vs Failure Rate", *Journal of Dental Health, Oral Disorders & Therapy*, vol. 4, pp. 4–5, 2016.

[4]   L. Levin, "Dealing with dental implant failures", *Journal of Applied Oral Science*, vol. 16, pp. 171–175, 2008.

[5]   H.-J. Han, S. Kim, & D.-H. Han, "Multifactorial evaluation of implant failure: a 19-year retrospective study", *The International Journal of Oral & Maxillofacial Implants*, vol. 29, pp. 303–310, 2014.

[6]   O.E. Ogle, "Implant Surface Material, Design, and Osseointegration", *Dental Clinics of North America*, vol. 59, pp. 505–520, 2015.

[7]   P.F. Manicone et al., "Biological considerations on the use of zirconia for dental devices", *International Journal of Immunopathology and Pharmacology*, vol. 20, pp. 9–12, 2007.

[8]   J. Li, Y. Liu, L. Hermansson, & R. Söremark, "Evaluation of biocompatibility of various ceramic powders with human fibroblasts in vitro", *Clinical Materials*, vol. 12, pp. 197–201, 1993.

[9]   H. Warashina et al., "Biological reaction to alumina, zirconia, titanium and polyethylene particles implanted onto murine calvaria", *Biomaterials*, vol. 24, pp. 3655–3661, 2003.

[10]   C. Piconi et al., "Y-TZP ceramics for artificial joint replacements", *Biomaterials*, vol. 19, pp. 1489–1494, 1998.

[11]   R. Depprich et al., "Osseointegration of zirconia implants compared with titanium: An in vivo study", *Head and Face Medicine*, vol. 4, pp. 1–8, 2008.

[12]   L. Rimondini, L. Cerroni, A. Carrassi, & P. Torricelli, "Bacterial Colonization of Zirconia Ceramic Surfaces: An in Vitro and in Vivo Study", *International Journal of Oral and Maxillofacial Implants*, vol. 17, pp. 793–798, 2002.

[13]   A. Scarano, M. Piattelli, S. Caputi, G.A. Favero, & A. Piattelli, "Bacterial Adhesion on

Commercially Pure Titanium and Zirconium Oxide Disks: An In Vivo Human Study", *Journal of Periodontology*, vol. 75, pp. 292–296, 2004.

[14] C. Sanon et al., "A new testing protocol for zirconia dental implants", *Dental Materials*, vol. 31, pp. 15–25, 2015.

[15] K. Sivaraman, A. Chopra, A.I. Narayan, & D. Balakrishnan, "Is zirconia a viable alternative to titanium for oral implant? A critical review", *Journal of Prosthodontic Research*, 2017.

[16] M. Gahlert et al., "Biomechanical and histomorphometric comparison between zirconia implants with varying surface textures and a titanium implant in the maxilla of miniature pigs", *Clinical Oral Implants Research*, vol. 18, pp. 662–668, 2007.

[17] D. Buser et al., "Enhanced bone apposition to a chemically modified SLA titanium surface", *Journal of Dental Research*, vol. 83, pp. 529–533, 2004.

[18] D.L. Cochran et al., "The use of reduced healing times on ITI® implants with a sandblasted and acid-etched (SLA) surface: Early results from clinical trials on ITI® SLA implants", *Clinical Oral Implants Research*, vol. 13, pp. 144–153, 2002.

[19] A. Sicilia et al., "Titanium allergy in dental implant patients: A clinical study on 1500 consecutive patients", *Clinical Oral Implants Research*, vol. 19, pp. 823–835, 2008.

[20] H. Egusa, N. Ko, T. Shimazu, & H. Yatani, "Suspected association of an allergic reaction with titanium dental implants: A clinical report", *Journal of Prosthetic Dentistry*, vol. 100, pp. 344–347, 2008.

[21] H. Reactions, "Hypersensitivity Reactions to Titanium: Diagnosis and Management", *American Contact Dermatitis Society*, vol. 26, pp. 7–25, 2015.

[22] V. Vijayaraghavan, A. V. Sabane, & K. Tejas, "Hypersensitivity to titanium: A less explored area of research", *Journal of Indian Prosthodontist Society*, vol. 12, pp. 201–207, 2012.

[23] A. Mellado-Valero, A.I. Muñoz, V.G. Pina, & M.F. Sola-Ruiz, "Electrochemical behaviour and galvanic effects of titanium implants coupled to metallic suprastructures in artificial saliva", *Materials*, vol. 11, 2018.

[24] R.H.J. Hannink, P.M. Kelly, & B.C. Muddle, "Transformation Toughening in Zirconia-Containing Ceramics", *Journal of the American Ceramic Society*, vol. 83, pp. 461–487, 2004.

[25] L. Treccani, T. Yvonne Klein, F. Meder, K. Pardun, & K. Rezwan, "Functionalized ceramics for biomedical, biotechnological and environmental applications", *Acta Biomaterialia*,

vol. 9, pp. 7115–7150, 2013.

[26] M. Hisbergues, S. Vendeville, & P. Vendeville, "Review zirconia: Established facts and perspectives for a biomaterial in dental implantology", *Journal of Biomedical Materials Research - Part B Applied Biomaterials*, vol. 88, pp. 519–529, 2009.

[27] Q. Fang, P.S. Sidky, & M.G. Hocking, "Erosion and corrosion of PSZ-zirconia and the t-m phase transformation", *Wear*, vol. 233–235, pp. 615–622, 1999.

[28] C. Piconi, & G. Maccauro, "Zirconia as a ceramic biomaterial", *Biomaterials*, vol. 20, pp. 1–25, 1999.

[29] A. Al-Ahmad et al., "In vivo study of the initial bacterial adhesion on different implant materials", *Archives of Oral Biology*, vol. 58, pp. 1139–1147, 2013.

[30] A.S.D. Al-Radha, D. Dymock, C. Younes, & D. O'Sullivan, "Surface properties of titanium and zirconia dental implant materials and their effect on bacterial adhesion", *Journal of Dentistry*, vol. 40, pp. 146–153, 2012.

[31] R.J. Kohal, D. Weng, M. Bächle, & J.R. Strub, "Loaded custom-made zirconia and titanium implants show similar osseointegration: an animal experiment.", *Journal of Periodontology*, vol. 75, pp. 1262–1268, 2004.

[32] I. Denry, & J.R. Kelly, "State of the art of zirconia for dental applications", *Dental Materials*, vol. 24, pp. 299–307, 2008.

[33] M. Montazerian, & E.D. Zanotto, "Bioactive and inert dental glass-ceramics", *Journal of Biomedical Materials Research - Part A*, vol. 105, pp. 619–639, 2017.

[34] R. Milani, Nitretação a plasma de zircónia parcialmente estabilizada, Universidade de Caxias do Sul, 2009.

[35] P. Christel, A. Meunier, M. Heller, J.P. Torre, & C.N. Peille, "Mechanical properties and short-term in vivo evaluation of yttrium-oxide-partially-stabilized zirconia", *Journal of Biomedical Materials Research*, vol. 23, pp. 45–61, 1989.

[36] A.F. vo. Recum, Handbook of Biomaterials Evaluation: Scientific, Technical, and Clinical Testing of Implant Materials, 2nd editio, Taylor & Francis, United States of America, 1999.

[37] F. WAKAI, S. SAKAGUCHI, & Y. MATSUNO, "Superplasticity of Yttria-Stabilized Tetragonal ZrO2 Polycrystals", *Advanced Ceramic Materials*, vol. 1, pp. 259–263, 1986.

[38] D.W. Paquette, N. Brodala, & R.C. Williams, "Risk Factors for Endosseous Dental Implant Failure", *Dental Clinics*, vol. 50, pp. 361–374, 2006.

[39] A.M. Roos-Jansåker, C. Lindahl, H. Renvert, & S. Renvert, "Nine- to fourteen-year follow-up of implant treatment. Part II: Presence of peri-implant lesions", *Journal of Clinical Periodontology*, vol. 33, pp. 290–295, 2006.

[40] S. Sakka, K. Baroudi, & M.Z. Nassani, "Factors associated with early and late failure of dental implants.", *Journal of Investigative and Clinical Dentistry*, vol. 3, pp. 258–261, 2012.

[41] F.J. Manzano-Moreno, F.J. Herrera-Briones, T. Bassam, M.F. Vallecillo-Capilla, & C. Reyes-Botella, "Factors affecting dental implant stability measured using the ostell mentor device: A systematic review", *Implant Dentistry*, vol. 24, pp. 565–577, 2015.

[42] R.B. Osman, & M. V. Swain, "A critical review of dental implant materials with an emphasis on titanium versus zirconia", *Materials*, vol. 8, pp. 932–958, 2015.

[43] N. Sykaras, a M. Iacopino, V. a Marker, R.G. Triplett, & R.D. Woody, "Implant materials, designs, and surface topographies: their effect on osseointegration. A literature review.", *The International Journal of Oral & Maxillofacial Implants*, vol. 15, pp. 675–690, 2000.

[44] W. Teughels, N. Assche, I. Sliepen, & M. Quirynen, "Effect of Material Characteristics and/or Surface Topography on Biofilm Development", *Clinical Oral Implants Research*, vol. 17 Suppl 2, pp. 68–81, 2006.

[45] Y. Manor, S. Oubaid, O. Mardinger, G. Chaushu, & J. Nissan, "Characteristics of Early Versus Late Implant Failure: A Retrospective Study", *Journal of Oral and Maxillofacial Surgery*, vol. 67, pp. 2649–2652, 2009.

[46] D.M. Chung, T.-J. Oh, J. Lee, C.E. Misch, & H.-L. Wang, "Factors affecting late implant bone loss: a retrospective analysis.", *The International Journal of Oral & Maxillofacial Implants*, vol. 22, pp. 117–126, 2007.

[47] A. Mombelli, N. Müller, & N. Cionca, "The epidemiology of peri-implantitis", *Clinical Oral Implants Research*, vol. 23, pp. 67–76, 2012.

[48] M. Kate, S. Palaskar, & P. Kapoor, "Implant failure: A dentist's nightmare", *Journal of Dental Implants*, vol. 6, pp. 51, 2016.

[49] C. Fransson, J. Wennström, C. Tomasi, & T. Berglundh, "Extent of peri-implantitis-associated bone loss", *Journal of Clinical Periodontology*, vol. 36, pp. 357–363, 2009.

[50] X. Yu et al., "Role of toll-like receptor 2 in inflammation and alveolar bone loss in experimental peri-implantitis versus periodontitis", *Journal of Periodontal Research*,

pp. 98–106, 2017.

[51] H.I. Nassar, & M.F. Abdalla, "Bacterial leakage of different internal implant/abutment connection", *Future Dental Journal*, vol. 1, pp. 1–5, 2015.

[52] V.K. Jansen, G. Conrads, & E.J. Richter, "Microbial leakage and marginal fit of the implant-abutment interface.", *The International Journal of Oral & Maxillofacial Implants*, vol. 12, pp. 527–540, 1997.

[53] Mombelli Andrea, & P.Lang Niklaus, "The diagnosis and treatment of peri-implantitis", vol. 17, pp. 1–51, 2000.

[54] A. Mombelli, "Microbiology and antimicrobial therapy of peri-implantitis", *Periodontology 2000*, vol. 28, pp. 177–189, 2002.

[55] S. Renvert, A.M. Roos-Jansåker, C. Lindahl, H. Renvert, & G. Rutger Persson, "Infection at titanium implants with or without a clinical diagnosis of inflammation", *Clinical Oral Implants Research*, vol. 18, pp. 509–516, 2007.

[56] L.A.R.S.D. Gunnar, "Microbial findings at failing implants", 1999.

[57] J.F. Hernández-Sierra et al., "The antimicrobial sensitivity of Streptococcus mutans to nanoparticles of silver, zinc oxide, and gold", *Nanomedicine: Nanotechnology, Biology, and Medicine*, vol. 4, pp. 237–240, 2008.

[58] L. Montanaro et al., "Evaluation of bacterial adhesion of Streptococcus mutans on dental restorative materials", *Biomaterials*, vol. 25, pp. 4457–4463, 2004.

[59] R. Buergers, W. Schneider-Brachert, S. Hahnel, M. Rosentritt, & G. Handel, "Streptococcal adhesion to novel low-shrink silorane-based restorative", *Dental Materials*, vol. 25, pp. 269–275, 2009.

[60] M. Grivet, J.J. Morrier, G. Benay, & O. Barsotti, "Effect of hydrophobicity on in vitro streptococcal adhesion to dental alloys", *Journal of Materials Science: Materials in Medicine*, vol. 11, pp. 637–642, 2000.

[61] S. Rinke, S. Ohl, D. Ziebolz, K. Lange, & P. Eickholz, "Prevalence of periimplant disease in partially edentulous patients: A practice-based cross-sectional study", *Clinical Oral Implants Research*, vol. 22, pp. 826–833, 2011.

[62] A.W. Rosaleen Anderson, Paul W. Groundwater, Adam Todd, Antibacterial Agents: Chemistry, Mode of Action, Mechanisms of Resistance and Clinical Applications, in: Wiley, 2012: p. 11.

[63] E.M. Hetrick, & M.H. Schoenfisch, "Reducing implant-related infections: active release

strategies", *Chemical Society Reviews*, vol. 35, pp. 780–789, 2006.

[64]   M.C.M. van Loosdrecht, & A.J.B. Zehnder, "Energetics of bacterial adhesion", *Experientia*, vol. 46, pp. 817–822, 1990.

[65]   Y. Liu, & Q. Zhao, "Influence of surface energy of modified surfaces on bacterial adhesion", *Biophysical Chemistry*, vol. 117, pp. 39–45, 2005.

[66]   S. Sirajuddin et al., "Iatrogenic Damage to the Periodontium Caused by Implants and Implant Treatment Procedures", *The Journal of Oral Implantology*, pp. 200–202, 2015.

[67]   E. Rompen, "The effect of material characteristics, of surface topography and of implant components and connections on soft tissue integration: A literature review", vol. 17, pp. 55–67, 2006.

[68]   J.L. T. Berglundh, "Dimension of the periimplant mucosa", *Journal of Clinical Periodontology*, vol. 23, pp. 971–973, 1996.

[69]   J. Blanco et al., "Biological width following immediate implant placement in the dog: Flap vs. flapless surgery", *Clinical Oral Implants Research*, vol. 21, pp. 624–631, 2010.

[70]   A. Pae, H. Lee, H.-S. Kim, Y.-D. Kwon, & Y.-H. Woo, "Attachment and growth behaviour of human gingival fibroblasts on titanium and zirconia ceramic surfaces", *Biomedical Materials*, vol. 4, pp. 025005, 2009.

[71]   M. Könönen, M. Hormia, J. Kivilahti, J. Hautaniemi, & I. Thesleff, "Effect of surface processing on the attachment, orientation, and proliferation of human gingival fibroblasts on titanium.", *Journal of Biomedical Materials Research*, vol. 26, pp. 1325–41, 1992.

[72]   M. Hormia, M. Könönen, J. Kivilahti, & I. Virtanen, "Immunolocalization of proteins specific for adhaerens junctions in human gingival epithelial cells grown on differently processed titanium surfaces", *Journal of Periodontal Research*, vol. 26, pp. 491–497, 1991.

[73]   T. Inoue, J.E. Cox, R.M. Pilliar, & A.H. Melcher, "Effect of the surface geometry of smooth and porous-coated titanium alloy on the orientation of fibroblasts in vitro", *Journal of Biomedical Materials Research*, vol. 21, pp. 107–126, 1987.

[74]   C. Kwon, Y. Kim, & H. Jeon, "Collective Migration of Lens Epithelial Cell Induced by Differential Microscale Groove Patterns", *Journal of Functional Biomaterials*, vol. 8, pp. 34, 2017.

[75]   B.A. Dalton et al., "Modulation of epithelial tissue and cell migration by microgrooves",

J Biomed Mater Res, vol. 56, pp. 195–207, 2001.

[76] X.F. Walboomers, H.J.E. Croes, L.A. Ginsel, & J.A. Jansen, "Growth behavior of fibroblasts on microgrooved polystyrene", *Biomaterials*, vol. 19, pp. 1861–1868, 1998.

[77] D.M. Brunette, G.S. Kenner, & T.R.L. Gould, "Grooved Titanium Surfaces Orient Growth and Migration of Cells from Human Gingival Explants", pp. 1045–1048, 2015.

[78] D.M. Brunette, "Spreading and orientation of epithelial cells on grooved substrata", *Experimental Cell Research*, vol. 167, pp. 203–217, 1986.

[79] J. Hasan, R.J. Crawford, & E.P. Ivanova, "Antibacterial surfaces: The quest for a new generation of biomaterials", *Trends in Biotechnology*, vol. 31, pp. 295–304, 2013.

[80] M. Gross, S.E. Cramton, F. Götz, & A. Peschel, "Key Role of Teichoic Acid Net Charge in Staphylococcus aureus Colonization of Artificial Surfaces", *Infection and Immunity*, vol. 69, pp. 3423–2426, 2001.

[81] S. Brown, J.P. Santa Maria, & S. Walker, "Wall Teichoic Acids of Gram-Positive Bacteria", *Annual Review of Microbiology*, vol. 67, pp. 313–336, 2013.

[82] B. Gottenbos, D.W. Grijpma, H.C. van der Mei, J. Feijen, & H.J. Busscher, "Antimicrobial effects of positively charged surfaces on adhering Gram-positive and Gram-negative bacteria", *Journal of Antimicrobial Chemotherapy*, vol. 48, pp. 7–13, 2001.

[83] L.D. Renner, & D.B. Weibel, "Physicochemical regulation of biofilm formation", *MRS Bulletin / Materials Research Society*, vol. 36, pp. 347–355, 2011.

[84] T.R. Garrett, M. Bhakoo, & Z. Zhang, "Bacterial adhesion and biofilms on surfaces", *Progress in Natural Science*, vol. 18, pp. 1049–1056, 2008.

[85] T. Wassmann, S. Kreis, M. Behr, & R. Buergers, "The influence of surface texture and wettability on initial bacterial adhesion on titanium and zirconium oxide dental implants", *International Journal of Implant Dentistry*, vol. 3, pp. 32, 2017.

[86] H.-W. Lee et al., "Identification of microbial communities, with a focus on foodborne pathogens, during kimchi manufacturing process using culture-independent and -dependent analyses", *LWT - Food Science and Technology*, vol. 81, pp. 153–159, 2017.

[87] K.A. Whitehead, J. Colligon, & J. Verran, "Retention of microbial cells in substratum surface features of micrometer and sub-micrometer dimensions", *Colloids and Surfaces B: Biointerfaces*, vol. 41, pp. 129–138, 2005.

[88] N. Beyth, I. Yudovin-Farber, M. Perez-Davidi, A.J. Domb, & E.I. Weiss, "Polyethyleneimine nanoparticles incorporated into resin composite cause cell death

and trigger biofilm stress in vivo", *Proceedings of the National Academy of Sciences*, vol. 107, pp. 22038–22043, 2010.

[89] G.C. Padovani et al., "Advances in Dental Materials through Nanotechnology: Facts, Perspectives and Toxicological Aspects", *Trends in Biotechnology*, vol. 33, pp. 621–636, 2015.

[90] Y.Z. Wan, S. Raman, F. He, & Y. Huang, "Surface modification of medical metals by ion implantation of silver and copper", *Applied Surface Science*, vol. 81, pp. 1114–1118, 2007.

[91] N. Padmavathy, & R. Vijayaraghavan, "Enhanced bioactivity of ZnO nanoparticles - An antimicrobial study", *Science and Technology of Advanced Materials*, vol. 9, 2008.

[92] N. Ichinose, Y. Ozaki, & S. Kashu, Superfine Particle Technology, Springer-Verlag, 2012.

[93] M. Hosokawa, K. Nogi, M. Naito, & T. Yokoyama, Nanoparticle Technology Handbook, First edit, Elsevier B.V., Amsterdam, 2007.

[94] A. Tiraferri, C.D. Vecitis, & M. Elimelech, "Covalent binding of single-walled carbon nanotubes to polyamide membranes for antimicrobial surface properties", *ACS Applied Materials and Interfaces*, vol. 3, pp. 2869–2877, 2011.

[95] M. Gunell et al., "Antimicrobial characterization of silver nanoparticle-coated surfaces by "touch test" method", *Nanotechnology, Science and Applications*, vol. 10, pp. 137–145, 2017.

[96] Y.M. Baoquan Jia, & and L.Z. Li Cheng, Jinping Zhou, "Preparation of copper nanoparticles coated cellulose films with.pdf", *American Chemical Society Applied Materials Interfaces*, vol. 4, pp. 2897–2902, 2012.

[97] E.P. Ivanova et al., "Natural bactericidal surfaces: Mechanical rupture of pseudomonas aeruginosa cells by cicada wings", *Small*, vol. 8, pp. 2489–2494, 2012.

[98] M. Stigter, J. Bezemer, K. De Groot, & P. Layrolle, "Incorporation of different antibiotics into carbonated hydroxyapatite coatings on titanium implants, release and antibiotic efficacy", *Journal of Controlled Release*, vol. 99, pp. 127–137, 2004.

[99] V. Alt et al., "The effects of combined gentamicin-hydroxyapatite coating for cementless joint prostheses on the reduction of infection rates in a rabbit infection prophylaxis model", *Biomaterials*, vol. 27, pp. 4627–4634, 2006.

[100] J. Hardes et al., "Lack of toxicological side-effects in silver-coated megaprostheses in humans", *Biomaterials*, vol. 28, pp. 2869–2875, 2007.

[101] Y.Z. Wan et al., "Modification of medical metals by ion implantation of copper", *Applied Surface Science*, vol. 253, pp. 9426–9429, 2007.

[102] K. El-Refaie et al., "Biocidal polymers: Synthesis, antimicrobial activity, and possible toxicity of poly (hydroxystyrene-co-methylmethacrylate) derivatives", *Journal of Applied Polymer Science*, vol. 120, pp. 2734–2742, 2011.

[103] F. Siedenbiedel, & J.C. Tiller, "Antimicrobial polymers in solution and on surfaces: Overview and functional principles", *Polymers*, vol. 4, pp. 46–71, 2012.

[104] C.P. Fik et al., "Impact of functional satellite groups on the antimicrobial activity and hemocompatibility of telechelic poly(2-methyloxazoline)s", *Biomacromolecules*, vol. 13, pp. 165–172, 2012.

[105] M.W. Huh et al., "Surface characterization and antibacterial activity of chitosan-grafted poly(ethylene terephthalate) prepared by plasma glow discharge", *Journal of Applied Polymer Science*, vol. 81, pp. 2769–2778, 2001.

[106] Y. Xing et al., "Effect of TiO2nanoparticles on the antibacterial and physical properties of polyethylene-based film", *Progress in Organic Coatings*, vol. 73, pp. 219–224, 2012.

[107] D. Das, B.C. Nath, P. Phukon, & S.K. Dolui, "Synthesis and evaluation of antioxidant and antibacterial behavior of CuO nanoparticles", *Colloids and Surfaces B: Biointerfaces*, vol. 101, pp. 430–433, 2013.

[108] Y.H. Leung et al., "Mechanisms of antibacterial activity of mgo: Non-ros mediated toxicity of mgo nanoparticles towards escherichia coli", *Small*, vol. 10, pp. 1171–1183, 2014.

[109] S. Agnihotri, S. Mukherji, & S. Mukherji, "Size-controlled silver nanoparticles synthesized over the range 5-100 nm using the same protocol and their antibacterial efficacy", *RSC Advances*, vol. 4, pp. 3974–3983, 2014.

[110] J. Ramyadevi, K. Jeyasubramanian, A. Marikani, G. Rajakumar, & A.A. Rahuman, "Synthesis and antimicrobial activity of copper nanoparticles", *Materials Letters*, vol. 71, pp. 114–116, 2012.

[111] T. Russo et al., "Preliminary focus on the mechanical and antibacterial activity of a PMMA-based bone cement loaded with gold nanoparticles", *Bioactive Materials*, vol. 2, pp. 156–161, 2017.

[112] H. Beherei, "Preparation and characterization of novel antibacterial nano-ceramic-composites for bone grafting", *Der Pharma Chemica*, vol. 3, pp. 10–27, 2011.

[113] L. Juan, Z. Zhimin, M. Anchun, L. Lei, & Z. Jingchao, "Deposition of silver nanoparticles on titanium surface for antibacterial effect", *International Journal of Nanomedicine*, vol. 5, pp. 261–267, 2010.

[114] N.I. Chalmers et al., "Use of quantum dot luminescent probes to achieve single-cell resolution of human oral bacteria in biofilms", *Applied and Environmental Microbiology*, vol. 73, pp. 630–636, 2007.

[115] Y.H. Lee, & D.T. Wong, "Saliva: An emerging biofluid for early detection of diseases", *American Journal of Dentistry*, vol. 22, pp. 241–248, 2009.

[116] M. Ahamed, M.S. AlSalhi, & M.K.J. Siddiqui, "Silver nanoparticle applications and human health", *Clinica Chimica Acta*, vol. 411, pp. 1841–1848, 2010.

[117] S.M. Dizaj, F. Lotfipour, M. Barzegar-Jalali, M.H. Zarrintan, & K. Adibkia, "Antimicrobial activity of the metals and metal oxide nanoparticles", *Materials Science and Engineering C*, vol. 44, pp. 278–284, 2014.

[118] C. Marambio-Jones, & E.M.V. Hoek, "A review of the antibacterial effects of silver nanomaterials and potential implications for human health and the environment", *Journal of Nanoparticle Research*, vol. 12, pp. 1531–1551, 2010.

[119] S. Eustis, & M.A. El-Sayed, "Why gold nanoparticles are more precious than pretty gold: Noble metal surface plasmon resonance and its enhancement of the radiative and nonradiative properties of nanocrystals of different shapes", *Chemical Society Reviews*, vol. 35, pp. 209–217, 2006.

[120] D. Astruc, Nanoparticles and Catalysis, John Wiley & Sons, Weinheim, 2008.

[121] S. Link, & M.A. El-sayed, "Optical properties and ultrafast dynamics of metallic nanocrystals", *Laser Dynamics Laboratory, School of Chemistry and Biochemistry*, vol. 54, pp. 331–366, 2003.

[122] Y. Cui et al., "The molecular mechanism of action of bactericidal gold nanoparticles on Escherichia coli", *Biomaterials*, vol. 33, pp. 2327–2333, 2012.

[123] E. Lima, R. Guerra, V. Lara, & A. Guzmán, "Gold nanoparticles as efficient antimicrobial agents for Escherichia coli and Salmonella typhi", *Chemistry Central Journal*, vol. 7, pp. 1–7, 2013.

[124] G. Gosheger et al., "Silver-coated megaendoprostheses in a rabbit model - An analysis of the infection rate and toxicological side effects", *Biomaterials*, vol. 25, pp. 5547–5556, 2004.

[125] X. Zhang et al., "Synthesis and antibacterial property of Ag-containing TiO2coatings by combining magnetron sputtering with micro-arc oxidation", *Surface and Coatings Technology*, vol. 235, pp. 748–754, 2013.

[126] Y. Dong et al., "Towards long-lasting antibacterial stainless steel surfaces by combining double glow plasma silvering with active screen plasma nitriding", *Acta Biomaterialia*, vol. 7, pp. 447–457, 2011.

[127] G. Madhumitha, G. Elango, & S.M. Roopan, "Bio-functionalized doped silver nanoparticles and its antimicrobial studies", *Journal of Sol-Gel Science and Technology*, vol. 73, pp. 476–483, 2014.

[128] Y. Huang et al., "A randomized comparative trial between Acticoat and SD-Ag in the treatment of residual burn wounds, including safety analysis", *Burns*, vol. 33, pp. 161–166, 2007.

[129] K. Chaloupka, Y. Malam, & A.M. Seifalian, "Nanosilver as a new generation of nanoproduct in biomedical applications", *Trends in Biotechnology*, vol. 28, pp. 580–588, 2010.

[130] A. De Mel et al., "A silver nanocomposite biomaterial for blood-contacting implants", *Journal of Biomedical Materials Research - Part A*, vol. 100 A, pp. 2348–2357, 2012.

[131] V. Alt et al., "An in vitro assessment of the antibacterial properties and cytotoxicity of nanoparticulate silver bone cement", *Biomaterials*, vol. 25, pp. 4383–4391, 2004.

[132] H. van de Belt et al., "Infection of orthopedic implants and the use of anti- biotic-loaded bone cements (A review)", *Acta Orthop Scand*, vol. 72, pp. 557–571, 2001.

[133] T.M. Benn, & P. Westerhoff, "Nanoparticle Silver Released into Water from Commercially Available Sock Fabrics", pp. 4133–4139, 2008.

[134] Q. Chaudhry et al., "Applications and implications of nanotechnologies for the food sector", *Food Additives and Contaminants - Part A Chemistry, Analysis, Control, Exposure and Risk Assessment*, vol. 25, pp. 241–258, 2008.

[135] M. Yadollahi, H. Namazi, & M. Aghazadeh, "Antibacterial carboxymethyl cellulose/Ag nanocomposite hydrogels cross-linked with layered double hydroxides", *International Journal of Biological Macromolecules*, vol. 79, pp. 269–277, 2015.

[136] G.M. Raghavendra et al., "Cellulose-polymer-Ag nanocomposite fibers for antibacterial fabrics/skin scaffolds", *Carbohydrate Polymers*, vol. 93, pp. 553–560, 2013.

[137] S.B. Sant, K.S. Gill, & R.E. Burrell, "Nanostructure, dissolution and morphology

characteristics of microcidal silver films deposited by magnetron sputtering", *Acta Biomaterialia*, vol. 3, pp. 341–350, 2007.

[138] K. Xu et al., "Microorganism adhesion inhibited by silver doped Yttria-stabilized zirconia ceramics", *Ceramics International*, vol. 37, pp. 2109–2115, 2011.

[139] S. Ravindra, Y. Murali Mohan, N. Narayana Reddy, & K. Mohana Raju, "Fabrication of antibacterial cotton fibres loaded with silver nanoparticles via " Green Approach"", *Colloids and Surfaces A: Physicochemical and Engineering Aspects*, vol. 367, pp. 31–40, 2010.

[140] S.N. Sawant, V. Selvaraj, V. Prabhawathi, & M. Doble, "Antibiofilm Properties of Silver and Gold Incorporated PU, PCLm, PC and PMMA Nanocomposites under Two Shear Conditions", *PLoS ONE*, vol. 8, pp. 1–9, 2013.

[141] A.J. Bone et al., "Silver nanoparticle toxicity to Atlantic killifish (Fundulus heteroclitus) and Caenorhabditis elegans: A comparison of mesocosm, microcosm, and conventional laboratory studies", *Environmental Toxicology and Chemistry*, vol. 34, pp. 275–282, 2015.

[142] X. Yang et al., "Mechanism of silver nanoparticle toxicity is dependent on dissolved silver and surface coating in caenorhabditis elegans", *Environmental Science and Technology*, vol. 46, pp. 1119–1127, 2012.

[143] D. MubarakAli, N. Thajuddin, K. Jeganathan, & M. Gunasekaran, "Plant extract mediated synthesis of silver and gold nanoparticles and its antibacterial activity against clinically isolated pathogens", *Colloids and Surfaces B: Biointerfaces*, vol. 85, pp. 360–365, 2011.

[144] M.M. Mohamed, S.A. Fouad, H.A. Elshoky, G.M. Mohammed, & T.A. Salaheldin, "Antibacterial effect of gold nanoparticles against Corynebacterium pseudotuberculosis", *International Journal of Veterinary Science and Medicine*, vol. 5, pp. 23–29, 2017.

[145] X. Zhang, "Gold Nanoparticles: Recent Advances in the Biomedical Applications", *Cell Biochemistry and Biophysics*, vol. 72, pp. 771–775, 2015.

[146] J. Majumdar, & I. Manna, "Laser processing of materials", *Sadhana*, vol. 28, pp. 495–562, 2003.

[147] G. Thawari, J.K.S. Sundar, G. Sundararajan, & S. V. Joshi, "Influence of process parameters during pulsed Nd:YAG laser cutting of nickel-base superalloys", *Journal of*

Materials Processing Technology, vol. 170, pp. 229–239, 2005.

[148] C. De Giorgi et al., "Laser Micro-polishing of Stainless Steel for Antibacterial Surface Applications", *Procedia CIRP*, vol. 49, pp. 88–93, 2016.

[149] S.H. Ko, J. Chung, Y. Choi, C.P. Griogoropoulos, & D. Poulikakos, "Fabrication of Inkjet Printed Flexible Electronics by Low Temperature Subtractive Laser Processing", *Electronic and Photonic Packaging, Electrical Systems Design and Photonics, and Nanotechnology*, pp. 599–603, 2005.

[150] J.P. Parry et al., "Laser micromachining of zirconia (Y-TZP) ceramics in the picosecond regime and the impact on material strength", *International Journal of Applied Ceramic Technology*, vol. 8, pp. 163–171, 2011.

[151] A. Samant, Laser Machining of Structural Ceramics : Computational and Experimental Analysis, University of Tennessee - Knoxville, 2009.

[152] J.C. Ion, Laser Processing of Engineering Materials principles, procedure and industrial application., Elsevier Butterworth-Heinemann, 2005.

[153] A.N. Samant, & N.B. Dahotre, "Laser machining of structural ceramics-A review", *Journal of the European Ceramic Society*, vol. 29, pp. 969–993, 2009.

[154] Y. Liu et al., "Fabrication of micro-scale textured grooves on green ZrO 2 ceramics by pulsed laser ablation", *Ceramics International*, 2017.

[155] L. Hao, & J. Lawrence, "Effects of Nd:YAG laser treatment on the wettability characteristics of a zirconia-based bioceramic", *Optics and Lasers in Engineering*, vol. 44, pp. 803–814, 2006.

[156] E. Costa, M. Shiomi, K. Osakada, & T. Laoui, "Rapid manufacturing of metal components by laser forming", *International Journal of Machine Tools and Manufacture*, vol. 46, pp. 1459–1468, 2006.

[157] H. K. C. Yung, S. P. Wu, "Synthesis of submicron sized silver powder for metal deposition via laser sintered inkjet printing", *Journal of Materials Science*, pp. 154–159, 2009.

[158] S. Hong et al., "Nonvacuum , Maskless Fabrication of a Flexible Metal Grid Transparent Conductor by Low-Temperature Selective Laser Sintering of Nanoparticle Ink", 2013.

[159] Y.Y. Fong et al., "Influence of cationic surfactants on the formation and surface oxidation states of gold nanoparticles produced via laser ablation", *Langmuir*, vol. 29, pp. 12452–12462, 2013.

[160] F. Mafune, J. Kohno, Y. Takeda, & T. Kondow, "Formation of Gold Nanoparticles by Laser

Ablation in Aqueous Solution of Surfactant", pp. 5114–5120, 2001.

[161] F. Mafuné, J.Y. Kohno, Y. Takeda, & T. Kondow, "Dissociation and aggregation of gold nanoparticles under laser irradiation", *Journal of Physical Chemistry B*, vol. 105, pp. 9050–9056, 2001.

[162] S. Marcus, J.E. Lowder, & D.L. Mooney, "Large-spot thermal coupling of CO2 laser radiation to metallic surfaces", *Journal of Applied Physics*, vol. 47, pp. 2966–2968, 1976.

[163] J. Wang, "Experimental analysis and optimization of the CO2 laser cutting process for metallic coated sheet steels", *International Journal of Advanced Manufacturing Technology*, vol. 16, pp. 334–340, 2000.

[164] S. Mohan, M.A. Trunov, & E.L. Dreizin, "Heating and Ignition of Metallic Particles by a CO2 Laser", *Journal of Propulsion and Power*, vol. 24, pp. 199–205, 2008.

[165] G. D D, M. W, W. K, & P. R, "Laser additive manufacturing of metallic components: materials, processes and mechanisms", *International Materials Reviews*, vol. 57, pp. 133–164, 2012.

[166] J. Lehr, & A.M. Kietzig, "Production of homogenous micro-structures by femtosecond laser micro-machining", *Optics and Lasers in Engineering*, vol. 57, pp. 121–129, 2014.

[167] N.B. Dahotre, S.R. Paital, A.N. Samant, & C. Daniel, "Wetting behaviour of laser synthetic surface microtextures on Ti-6Al-4V for bioapplication", *Philosophical Transactions of the Royal Society A: Mathematical, Physical and Engineering Sciences*, vol. 368, pp. 1863–1889, 2010.

[168] D.B. Geohegan, A.A. Puretzky, G. Duscher, & S.J. Pennycook, "Time-resolved imaging of gas phase nanoparticle synthesis by laser ablation", *Applied Physics Letters*, vol. 72, pp. 2987–2989, 1998.

[169] S. Reich et al., "Pulsed laser ablation in liquids: Impact of the bubble dynamics on particle formation", *Journal of Colloid and Interface Science*, vol. 489, pp. 106–113, 2017.

[170] H. Zeng et al., "Nanomaterials via Laser Ablation/Irradiation in Liquid: A Review", *Advanced Functional Materials*, vol. 22, pp. 1333–1353, 2012.

[171] M. Hashida, H. Mishima, S. Tokita, & S. Sakabe, "Non-thermal ablation of expanded polytetrafluoroethylene with an intense femtosecond-pulse laser", *Optics Express*, vol. 17, 2009.

[172] A. Hamad et al., "Generation of silver titania nanoparticles from an Ag-Ti alloy via

picosecond laser ablation and their antibacterial activities", *RSC Advances*, vol. 5, 2015.

[173] B. Qian, & Z. Shen, "Laser sintering of ceramics", *Integrative Medicine Research*, vol. 1, pp. 315–321, 2013.

[174] J.P. Kruth, X. Wang, T. Laoui, & L. Froyen, "Lasers and materials in selective laser sintering", vol. 23, pp. 357–371, 2003.

[175] C.Y. Yap et al., "Review of selective laser melting: Materials and applications", *Applied Physics Reviews*, vol. 2, 2015.

[176] C.G. Moura et al., "Effects of laser fluence and liquid media on preparation of small Ag nanoparticles by laser ablation in liquid", *Optics and Laser Technology*, vol. 97, pp. 20–28, 2017.

[177] P.R. Gogate, R.K. Tayal, & A.B. Pandit, "Cavitation: A technology on the horizon", vol. 91, 2006.

[178] M. Sivakumar, S. Ying, & K. Wei, "Ultrasonics Sonochemistry Cavitation technology – A greener processing technique for the generation of pharmaceutical nanoemulsions", *Ultrasonics Sonochemistry*, 2014.

[179] J.B. Petr Ptáček, Magdaléna Nosková, František Šoukal, Tomáš Opravil, Jaromír Havlica, Atomic Absorption Spectroscopy, InTech, México, 2012.

[180] M.L. Parsons, B.W. Smith, & G.E. Bentley, Handbook of Flame Spectroscopy, Arizona, 1975.

[181] G. Li, L. Tam, & J.X. Tang, "Amplified effect of Brownian motion in bacterial near-surface swimming", vol. 105, pp. 18355–18359, 2008.

[182] C.S. Chen, J.L. Alonso, E. Ostuni, G.M. Whitesides, & D.E. Ingber, "Cell shape provides global control of focal adhesion assembly", *Biochemical and Biophysical Research Communications*, vol. 307, pp. 355–361, 2003.

[183] R. Mempin et al., "Release of extracellular ATP by bacteria during growth", *BMC Microbiology*, vol. 13, pp. 1–13, 2013.